Sede Amministrativa: Università degli Studi di Padova

Consiglio nazionale delle ricerche, Istituto di Fotonica e Nanotecnologie (CNR-IFN), Padova

---

Dipartimento di Ingegneria dell'Informazione

Faculty of Mathematics, Computer Science and Natural Sciences

SCUOLA DI DOTTORATO DI RICERCA IN: Ingegneria dell'Informazione

INDIRIZZO: Scienza e Ingegneria dell'Informazione

CICLO: XXXI

TESI IN COTUTELA

Design, development, and characterization of thin film filters for high brilliance sources in the EUV-soft x-ray spectral range

Direttore della Scuola: Ch.mo Prof. Andrea Neviani

Coordinatore d'indirizzo: Ch.mo Prof. Andrea Neviani

Supervisore: Ch.mo Prof. Piergiorgio Nicolosi

Supervisore: Chiar.mo Prof. Dr.rer.nat. Joachim Mayer

Dottoranda: Kety Mayelin Jimenez Tejeda

2019

Design, development and characterization of thin film filters for high brilliance sources in the EUV-soft x-ray spectral range

Kety Mayelin Jiménez Tejeda

A thesis presented for the degree of

Doctor of Philosophy

Dr.rer.nat

To the:

Faculty of Mathematics, Computer Science and Natural Sciences
RWTH Aachen, Germany
and
Department of Information Engineering
University of Padova, Italy

Supervisors: Prof. Piergiorgio Nicolosi, Prof. Joachim Mayer.

Abstract

This thesis addresses research works on the design, fabrication development and characterization of thin film transmittance filters for high brilliance sources in the Extreme Ultraviolet (EUV) and soft X-ray spectral regions. The development and fabrication of thin film filters for extreme ultraviolet (EUV) and soft x-ray high brilliance sources are strongly required in many applications. In the case of Third and fourth generation, light sources, high order harmonic generation (HHG) sources, the extreme ultraviolet (EUV) and soft x-ray thin film filters are used to remove multiple-order radiations; Furthermore, those filters must be suited to face the high peak power of this kind of sources.

In the EUV and soft-X ray spectral range region materials have high absorption, so finding proper materials or combination of materials that fulfill the requirements of the filters is quite challenging. Using simulations of the transmittance performance of a variety of materials, based on the theoretical values of their optical constants, and taking in account their mechanical properties, Nb and Zr were chosen as core elements for the fabrication and study of free-standing filters.

The first development part of this thesis is focused on the bottom-up fabrication technique of Nb, Zr, Nb/Zr, and Zr/Nb 100 nm thick, thin films, deposited on silicon nitrate membrane windows by magnetron sputtering technique, pursuing achieve free standing filter after reactive ion etching; Nb and Nb/Zr free standing filters were achieved. These samples were characterized using Rutherford backscattering, AFM images and transmittance characterization in the EUV between 4-20 nm using synchrotron radiation at the Bear Beamline, ELETTRA, Italy and in Optical Beamline at BESSY synchrotron, Berlin, Germany. Also, the samples were characterized in the same range using a plasma source base on puff gas target as a secondary technique of transmittance characterization.

The second part is the structural characterization of the filters using TEM Analysis.

The third development part of this thesis is focus in the study of high density EUV radiation damage of Nb, Zr, Zr/Nb and Nb/Zr 100 nm thick free-standing filters. For this part of the experiment sample were deposited on silicon nitrite windows using e-beam deposition technique, showing more stable structures, free-standing filters of each type were achieved after reactive ion etching. Samples were characterized before and after exposure using x ray photon spectroscopy (XPS) technique, AFM images, x ray diffraction technique, and transmittance characterization in the EUV spectral range performed with

synchrotron radiation at Bear Beamline. For the radiation exposure a high-density set-up base in a plasma discharge source was use at 13.5 nm wavelength. Also, transmission electron microscopy and scanning electron microscopy characterization were used as complementary techniques to study the samples structures and interface properties.

Sommario

La tesi presenta un lavoro di ricerca svolto sulla progettazione, lo sviluppo della fabbricazione e la caratterizzazione di filtri a membrana sottile per la trasmissione di fonti di alta luminosità nelle regioni spettrali dell'ultravioletto estremo (EUV) e dei raggi x molli. Lo sviluppo e la fabbricazione di filtri a membrana sottile per le fonti di alta luminosità nelle regioni spettrali dell'ultravioletto estremo (EUV) e dei raggi x molli è fortemente richiesto in molte applicazioni. Nel caso delle fonti di alta luminosità di terza e quarta generazione, ovvero la generazione di fonti di armoniche di alto livello (HHG), sono richiesti filtri a membrana sottile per l'ultravioletto estremo (EUV) e i raggi x molli per rimuovere radiazioni di ordine multiplo. Inoltre, questi filtri devono essere adatti per affrontare la potenza di alto picco proveniente da questo tipo di fonti.

Nella regione del campo spettrale delle fonti di armoniche di alto livello (HHG) e l'ultravioletto estremo (EUV) i materiali hanno alto assorbimento, pertanto trovare materiali adatti o combinazioni di materiali che soddisfano i requisiti dei filtri è molto impegnativo. Utilizzando simulazioni sulla prestazione della trasmissione di una varietà di materiali, basate sui valori teorici delle loro costanti ottime, e considerando le loro proprietà meccaniche, sono stati scelti il Nb e il Zr come elementi base per la fabbricazione e studio di filtri indipendenti.

La prima parte dello sviluppo di questa tesi si concentra sulla tecnica di fabbricazione bottom-up di filtri a membrana sottile di Nb, Zr, Nb/Zr e Zr/Nb con spessore di 100 nm depositati su finestre di membrane di nitruro di silicio tramite la tecnica della polverizzazione catodica (Magnetron sputtering), con l'obiettivo di ottenere un filtro indipendente in seguito alla collisione con ioni reattivi; sono stati ottenuti filtri indipendenti di Nb e Nb/Zr. Questi campioni sono stati caratterizzati usando la tecnica del backscattering di Rutherford, immagini AFM e la caratterizzazione della trasmittanza nell'ultravioletto estremo (EUV) nell'intervallo 4-20 nm utilizzando radiazioni del sincrotrone al Bear Beamline, l'ELETTRA, in Italia e l'Optical Beamile e del sincrotrone BESSY, a Berlino, in Germania. Inoltre, i campioni sono stati caratterizzati nella stessa gamma utilizzando un bersaglio gass puff e una fonte di plasma come tecnica secondaria per la caratterizzazione della transmittanza.

La seconda parte correspode alla characterizazione structurale dei filtri utilizando TEM Analysis.

La terza parte dello sviluppo di questa tesi si concentra sullo studio dei danni delle radiazioni dell'ultravioletto estremo (EUV) ad alta densità di Nb, Zr, Zr/Nb e Nb/Zr dei filtri indipendenti con spessore da 100nm. Per questa parte dell'esperimento i campioni sono stati depositati su finestre di membrane di nitruro di silicio usando la tecnica di deposizione e-beam, mostrando strutture più stabili, sono stati prodotti free standing filtri per ciascun tipo in seguito alla collisione con ioni reattivi (RIE). I campioni sono stati caratterizzati prima e dopo l'esposizione usando la tecnica fotoelettronica a raggi x (XPS), immagini AFM, la tecnica di diffrazione a raggi x e la caratterizzazione della trasmissione nel raggio spettrale dell'ultravioletto estremo (EUV) fatta usando le radiazioni del sincrotrone al Bear Beamline. Per l'esposizione alle radiazioni è stata usata una configurazione di base ad alta densità in una fonte di scarica al plasma a lunghezza d'onda di 13.5 nm. Inoltre, sono stati usati un microscopio elettronico a trasmissione e la scansione microspia elettronica come tecniche complementari per studiare la struttura dei campioni e le proprietà dell'interfaccia.

Acknowledgment

Firstly, I would like to express my sincere and deepest gratitude to my advisors Prof. Piergiorgio Nicolosi, Prof. Larissa Juschkin and Prof Joachim Mayer for their support and guidance during my PhD study and related research, for their immense patience, continuous motivation, and vast knowledge. Besides my official advisors, I would like to deeply thanks to Dr Paola Zuppella for her endless and dedicated support during these three years and for always having kind words to keep me going.

The author wishes to thank Dr Serhiy Danylyuk and all colleagues from ILT institute at RWTH Aachen University and the Julich Research Center, for giving me the opportunity to work in their labs and for all the knowledge passed to me during my mobility. Off course, Immense gratitude to the administrative staff of department of information engineering (DEI Padova) and Julich Research Center. An enormous thank you to Marta Lipinska and Maximilian Kruth from the for all the help received from you.

I thank my fellow students in the EXTATIC program for having insightful discussions during the welcome weeks and conferences, specially to my direct colleagues from the program: Mewael Sertsu, Ahmed Gaballah and Nadeem Ahmed for their support and friendships.

Furthermore, I also like to extend my acknowledgments to the financial support from The Education, Audiovisual and Culture Executive Agency (EACEA), Erasmus Mundus Joint Doctorate Program EXTATIC under framework partnership Agreement No. 2012-0033.

Finally, I would like to divide the dedication of this thesis into two families:

To my family, who during all my years of studies have been near me, in heart to keep me going and encourage me to achieve my goals; principally to my dear sister Patricia who knows always the precise words to motivate me.

To the Serbanoiu Family, who took me in as part of their own during these years, showing me kindness and love, especially to my dear friend Dan who introduced me to the whole family. I am very grateful to all of you, you kept my heart warm during the cold weather and the distance from my own family.

Publications and Conference Presentations

I. Publications during PhD program

1. **K. Jimenez**, P. Nicolosi, L. Juschkin, Nadeem. Ahmed, A.E.H. Gaballah, E. Cattaruzza, M. G. Sertsu, A. Gerardino, A. Giglia, G. Mussler, P. Zuppella. “EUV free-standing transmittance filters, for high brilliance sources, based on Nb/Zr and Zr/Nb thin films on Si3N4 membranes; Design, fabrication, optical and structural characterization. (Submitted to thin solid film 2019).

2. **K. Jimenez**, A.E.H. Gaballah, Nadeem. Ahmed, P. Zuppella, P.Nicolosi “Optical and structural characterization of Nb, Zr, Nb/Zr, Zr/Nb thin films on Si3N4 membranes windows. “SPIE Proc. 10236, Damage to VUV, EUV, and X-ray Optics (2017).

3. A.E.H. Gaballah, P.Zuppella, Nadeem Ahmed, **K. Jimenez**, G. Pettinari, A. Gerardino , P. Nicolosi, “A tabletop polarimetric facility for the EUV spectral range: implementations and characterization“ Proc. 10235, UV and X-ray Optics: Synergy between Laboratory and Space (2017).

4. A.E.H. Gaballah, P. Nicolosi, Nadeem Ahmed, **K. Jimenez**, G. Pettinari, A. Gerardino, P.Zuppella “EUV polarimetry for thin film and surface characterization and EUV phase retarder reflector development” Rev. Sci. Instrum. 89, 015108 (2018).

5. A.E.H. Gaballah, P. Nicolosi, P.Zuppella, Nadeem Ahmed, **K. Jimenez**, G. Pettinari, A. Gerardino, P. Nicolosi “Vacuum ultraviolet quarter wave plates based on SnTe/Al bilayer: design, fabrication and ellipsometric characterization” submitted to applied surface science, Appl. Surf. Sci. 463 (2018) 75–81. doi:10.1016/j.apsusc.2018.08.190.

6. Nadeem. Ahmed, P. Nicolosi, A.E.H. Gaballah, **K. Jimenez**, P. Zuppella “EUV reflective ellipsometry in laboratory: determination of the optical constants and phase retarder properties of at hydrogen Lyman-alpha” submitted to Materials Research Express.

II. Other publications by Author

1. **Kety Jimenez**, Jeileen Luciano, Stephanie Rodriguez, Omar Vega, Fernand Torres, Christian Laboy, Jose Santana & Luis G. Rosa. (2015). *Surface Shearing Effects on Langmuir–Blodgett Thin Films of* P(VDF-TrFE) Ferroelectric Surface, Ferroelectrics, 482:1, 3445, DOI: 10.1080/00150193.2015.1056699.

III. Presentations at Conferences and Workshops

- EXTATIC Welcome Week **(Workshop**), 11-15 January 2016 at University of Southampton, UK. Design, Development and characterization of thin film filters for high brilliance sources in the UV-X-ray Spectral range. (**Oral presentation**)

- *Design, Development and characterization of thin film filters for high brilliance sources in the UV-X-ray Spectral range.* PXRNMS 2016, Multilayer-**workshop** 2016 (TNW), November 2016, Twente University, Twente, Holand. **(Poster presentation)**.

- Training and measurements (**workshop**) Bear Beamline, Elettra Synchrotron, Trieste; November 2016.

- *Optical and structural characterization of Nb, Zr, Nb/Zr, Zr/Nb thin films on Si3N4*, SPIE Optics + Optoelectronics, April 2017, Prague, Czech Republic. **(Poster presentation).**

- Extatic Welcome Week (**workshop**), 16-20 January 2017 at the International Centre for Theoretical Physics in Trieste, Italy. *Optical and structural characterization of Nb, Zr, Nb/Zr thin films on* Si_3N_4 *membranes windows*. (**Oral Presentation**).

- Final EXTATIC welcome week **(workshop)**. 22-24 /2018, CTU Prague. Oral presentation "*Optical and Structural Characterization of Nb, Zr, Nb/Zr, Zr/Nb Thin Films on Si3N4 Membranes Windows"*. (**Oral Presentation**).

- 3rd International Workshop on Frontiers of X&XUV Optics and its Applications. October 4-6/ 2017. Prague, Czech Republic. "*Optical and Structural Characterization of Nb, Zr, Nb/Zr, Zr/Nb Thin Films On Si3N4 Membranes Windows"* (**Poster Presentation).**

- PTB's 304. Seminar "VUV and EUV Metrology. Helmholtz-Building of the Berlin-Charlottenburg campus site of PTB. Abbestr. 2-12, 10587 Berlin. "*Optical Characterization of Nb, Zr, Nb/Zr, Zr/Nb thin films for transmittance filters application"*. **(Poster Presentation).**

- Training and Transmittance Characterization **(workshop)** at BEAR beamline, ELETTRA synchrotron 2018.

- Training and Transmittance Characterization **(workshop)** at BEAR beamline, ELETTRA synchrotron 2018.

Acronyms

UV	Ultraviolet
EUV	Extreme Ultraviolet
XRR	X-ray reflection
ML	Multilayer
EUVL	EUV lithography
GI-EUVR	Grazing incidence EUV reflection
BEAR	Bending magnet for Emission, Absorption and Reflectivity
FELs	Free electron lasers
RF	Radio frequency
DC	Direct current
E-beam	Electron beam
PVD	Physical Vapor Deposition
AFM	Atomic force microscopy
TEM	Transmission electron microscopy
SEM	Scanning electron microscopy
HAADF	High angle annular dark-field
HRTEM	High resolution transmission microscopy
BF	Bright field
keV	Kilo electron volt
FWHM	Full width half maximum
GDP	Gas Discharge plasma

HHG	High harmonic generation
RIE	Reactive Ion Etching

Contents

Abstract 4
Sommario 6
Acknowledgment.....8
Publications and Conference Presentations 9
Acronyms 12
1. Introduction 16
1.1 Motivation. 16
1.2 Extreme ultraviolet and soft X-rays..... 17
1.3 The interaction of EUV with matter. 19
1.3.1 Thin film filters, simple boundary. 21
1.3.2 Normal incidence..... 23
1.3.3 Oblique incidence 24
1.3.4 Normal incidence in an absorbing media 26
1.3.5 Oblique incidence radiation in an absorbing media 27
1.3.6 Transmittance, reflectance and absorptance of thin films assembly. 28
1.3.7 Potential transmittance of thin film assembly. 31
1.4 High brilliance sources for EUV radiation. 32
2. Thin film transmittance filters: design..... 36
2.1 Choosing Materials..... 36
2.2 Niobium..... 40
2.3 Zirconium (Zr)..... 42
2.4 Nb and Zr, filters background..... 43
3. Experimental..... 45
3.1 Filters fabrication..... 45
3.1.1 Step 1. The Substrate..... 46
3.1.2 Step 2. Metal evaporation of the thin film layers. 47
3.1.2.1a RF Magnetron Sputtering deposition technique 48
3.1.2.1b Magnetron sputtering set-up and deposition process..... 49
3.1.2.2a E-beam evaporation technique..... 49
3.1.2.2b E-Beam evaporation set-up and deposition process 51
3.1.3 Step 3. Placement of polymer “legs”..... 52

3.1.4a Reactive Ion Etching (RIE) 52

3.1.4b Etching process 53

3.2 Characterization Methods. 54

3.2.1 Structural and chemical composition characterization 54

3.2.1.1 Atomic Force Microscopy 54

3.2.1.2 Rutherford backscattering spectrometry for thickness determination. 55

3.2.1.3 X-ray Diffraction (XRD) 56

..... 57

3.2.1.4. Scanning Electron Microscopy (SEM) 57

3.2.1.4 TEM, HRTEM, STEM and EDX 57

3.2.1.5 X-ray photoelectron spectroscopy (XPS) 59

3.2.2 Optical Characterization 60

3.2.2.1a Transmittance measurements using a gas puff target source. 60

3.2.2.1b Puff target source set-up 61

3.2.2.2 Transmittance measurements at synchrotron facilities. 62

3.2.2.2a Experimental setup at BEAR 62

3.2.2.2b Experimental set-up at BESSY II 63

4 Mechanical and optical characterization of Nb/Si3N4, Zr/Si3N4, Zr/Nb/Si3N4 and Nb/Zr/Si3N4 filters (Experiment 1). 65

4.1 Introduction 65

4.2 Results and discussion 66

4.3 Conclusions: 79

5. TEM Study of the bilayer structures Zr/Nb, Nb/Zr and Nb/Zr/Nb on Si3N4 membranes 80

5.1 Nb/Zr TEM analysis 81

6.2 Zr/Nb TEM analysis Structure 92

6.3 Nb/Zr/Nb TEM analysis structure 99

6. Study of EUV radiation damage on free self-standing Nb, Zr, Nb/Zr, and Zr/Nb thin film filters. (Ongoing) 102

6.1 Introduction 102

6.2 Description of the experiment. 103

6.3. High density radiation set up 104

7 Conclusion and recommendation. 106

Bibliography. 107

1. Introduction

1.1 Motivation.

The development and fabrication of thin film filters for extreme ultraviolet (EUV) high brilliance sources is strongly required in many applications. In the case of free electron laser (FEL), one of the critical technical problems is related to the rejection of high harmonics, seed laser, first stage photons, and diffuse light. In order to improve the quality of the beam delivered by these sources, suitable optical systems acting as band-pass filters are necessary **[1-7]**. FERMI is the free electron laser in Trieste, Italy: *FEL 1* covers the spectral range 20-100 nm and *FEL 2* covers the range 4- 20 nm **[8, 9].**

In several applications requiring high brilliant sources, thin film filters, for extreme ultraviolet and soft x-ray photons, are used to remove multiple-order radiations and are suited to face a high peak power of around 1-5 GW and a fluence associated to pulses of about 100 femtoseconds. They are also often used as gas barriers; in this case, the filters could interact with contaminant gases that can react with their surface causing damage or affecting their performances **[10-13]**. For these reasons the material selected for the fabrication of the filters should be highly resistant, both chemically and structurally, to high power radiation. Thin film filters are applied in other fields like EUV lithography and spectroscopy; for space experiments where they are used to select suitable spectral bands where spectral emission lines are used to derive plasma physical parameters, through spectroscopic diagnostic techniques **[14-17].**

Since materials have high absorption in the EUV spectral range filters must be very thin to achieve good transmittance performances, so, considering their optical, chemical and mechanical properties only a few materials demonstrate to be good candidates for transmittance filters. In *Figure 1.1* we can see the theoretical transmittance performance of different elements in the EUV. We are particularly interested in thin film transmittance filters for the spectral range between 4-20 nm, which is the range covered by FEL 2. Materials as Beryllium and other rare earth are suggested to be good candidates for transmittance filters in this ranges, but the toxicity of rare earth materials makes very difficult and dangerous the fabrication of such filters. Combination of metal materials in the form of bilayers or multilayers filters have being

presented before for the EUV region, most of them supported by metal mesh but others fabricated in free standing architectures **[18-23].**

1.2 Extreme ultraviolet and soft X-rays

The electromagnetic spectrum is divided in different identified regions, the precise boundaries that divide one region from another is not always perfect defined. The extreme ultraviolet (EUV) is located between the photon energies region of about 30 eV to 250 eV (wavelengths from about 40 nm to 5 nm) fading into the soft x ray region (SXR) that could extend from about 250 eV to several thousand eV (wavelengths

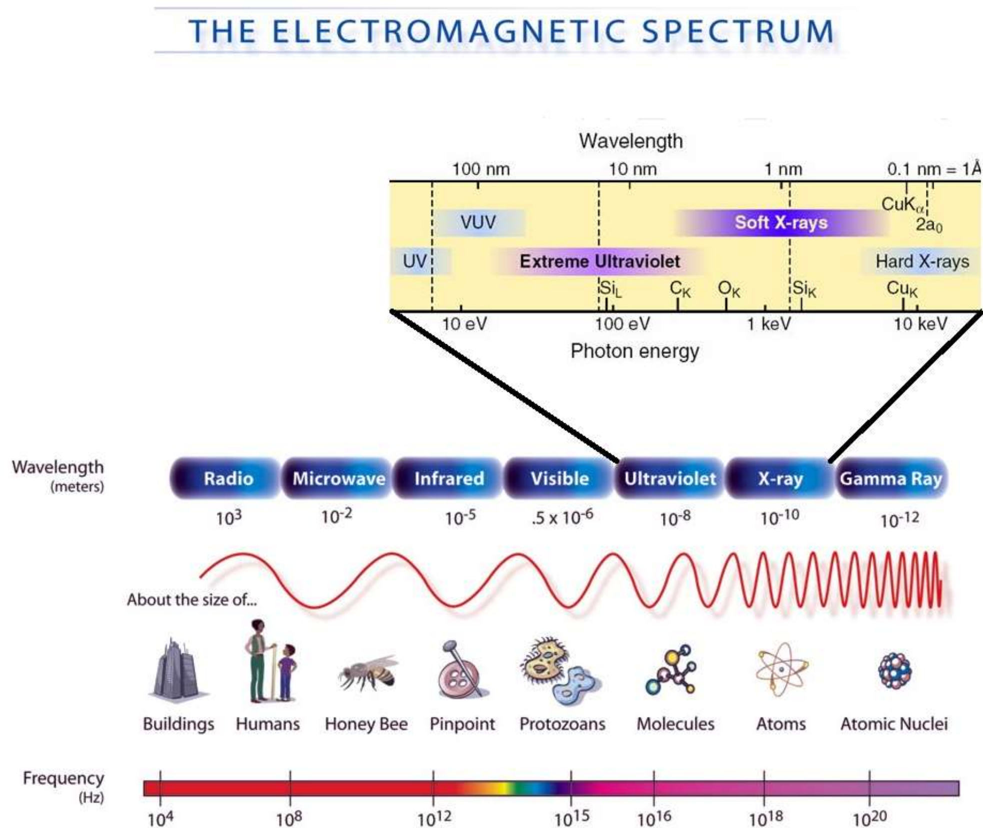

Figure 1.1 Electromagnetic spectrum, each identified region and their properties can be observed, focusing in the fading boundaries between EUV and SXR

from 5 nm to about 0.3 nm). A very well description of the physics and applications of EUV radiation and SXR are given in the book of D. Attwood [Ref] and only brief introduction

will be presented this section. In ***Figure 1.1*** we can appreciate the whole electromagnetic spectrum with a focus in the ultraviolet and X ray regions, making focus in the overlapping between the extreme ultraviolet and the soft x ray regions.

These energies regions are important because two mainly reasons: First, these energies are comparable with the binding energies of the core electrons of atoms; Second, the wavelength of EUV-SXR photons approach atomic dimensions, making them ideal for studies physical and chemical properties of molecules and atoms.

In the EUV most materials exhibit large absorption and since there is not so many available high-intensity EUV light sources (compact sources), experiments to study the optical properties of materials in the EUV represents still a big challenge. With strong absorption and low normal incident reflectivity, in this region experiments are best done using thin film.

EUV radiation is nowadays widely used in several applications. Most of these applications such as lithography, nanotechnology, material sciences, biology and imaging, require high brilliant light sources with spatial coherence and enough monochromaticity to be able to study and analyze materials and their behavior at the molecular and atomic level. EUV can be generated artificially in different ways such as hot plasma emission, synchrotron radiation and high harmonic generation. In laboratory scale experiments, the common sources for EUV radiation is based in the emission of hot plasma; among the sources are Discharge-Produced Plasmas (DPP) and Laser-Produced Plasmas (LPP). The use of synchrotron radiation have made growth the scientific research utilizing the vacuum ultraviolet to soft x-ray regions. The emission of EUV radiation from (FELs), also based on the same physical principle of synchrotron radiation [24] , has taken a significant consideration as a light source for EUV lithography and other applications due to their tunability, coherence and the availability of high-power accelerators.

1.3 The interaction of EUV with matter.

There are two models to explain the interactions EUV radiation with matter:

1. The photo absorption model
2. The coherent scattering model.

In photo-absorption, the energy of the incoming photon exceeds the ionization energy of the bound electron. When the photon energy is not enough to ionize atoms, the most frequently occurring process is a coherent scattering of the photon without energy loss [7ahmed]. Accordingly, the electron-photon interactions model can describe the interaction of EUV radiation with matter through the concept of scattering cross sections of particles as follows:

$$f^0(\omega) = f_1^0(\omega) + f_2^0(\omega)$$

where f_1^0 and f_2^0 correspond to the atomic scattering factors of an element, which are associated with the reflection and absorption respectively.

Each material shows distinctive interaction with EUV radiation and it can be described by the concept of the complex optical constant or complex index of refraction (N) as:

$$N = n - ik$$

where n and k, are the optical constants and these can be experimentally derived by applying methods based on reflectance and transmittance measurements combined with an optimized algorithm for fitting analysis.

N depend strongly of the frequency. The real part of N is called the refractive index (n) and k is known as the extinction coefficient. In the EUV, the complex refractive index N can be described also in terms of the atomic scattering factors f_1^0 and f_2^0 as [25]

$$N = n - ik = \frac{n_a r_e \lambda^2}{2\pi} f^0(\omega)$$

where n_a is the atomic density per unit volume, and λ is the wavelength of the EUV radiation and r_e is the classical electron radius which is defined as:

$$r_e = \frac{e^2}{4\pi\varepsilon_0\, m_e C^2} = 2.82\; x\; 10^{-15} m$$

Leading us to the following relationship between the real and imaginary parts of the scattering factor with the optical constants:

$$n = 1 - \frac{n_a r_e \lambda^2}{2\pi} f_1^0(\omega)$$

and

$$k = \frac{n_a r_e \lambda^2}{2\pi} f_2^0(\omega)$$

In the EUV, the real part of the optical constant (*n*) is smaller than one compared to the visible light. The absolute values of n and k decrease for higher energies, the complex index of refraction of all materials approaches unity. Photons with energy near to the energy necessary to excite an electron from its orbital lead to resonance at that precisely energy. The effect of this are manifested themselves in the complex index of refraction (N), more significant at n since its dependence with the frequency is very acutely. In contrast with the other energy ranges of the electromagnetic spectrum where resonance occurs (between infrared and visible, between the visible and the ultraviolet), the EUV results more complicated since the wavelength are on the same scale not only of the atomic dimensions but also in the scale of the physical and structural feature of the materials. The nanoscale imperfections or nanoscale structural changes on films or coatings don't represent big changes in the optical performance of the device in the other ranges of light, while in the EUV their presence can change it completely.[25]

1.3.1 Thin film filters, simple boundary.

Thin-film filters, such as single layer filters, multilayers, etc., normally consist of a certain number of boundaries between various homogeneous media. To calculate the effect that these boundaries will have on an incident wave let's start with the simpler case: A single boundary structure.

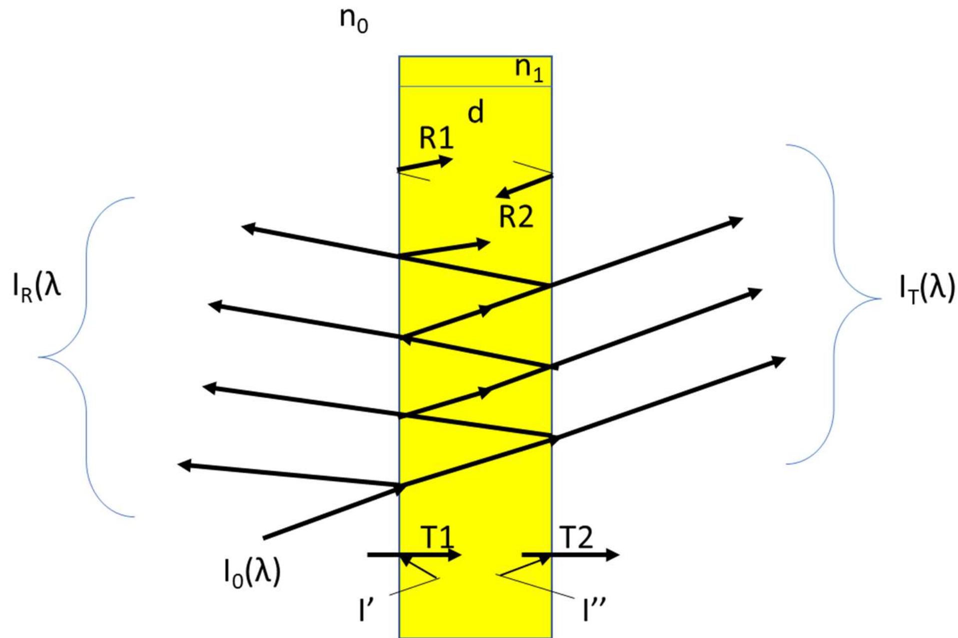

Figure 1.2 Diagram of specular transmission and reflection for a single layer filter.

Let's considering a free -absorption media, i.e. k = 0, if we assume a plane-polarized harmonic incident wave then this wave will be split into a reflected wave and a transmitted wave at the boundary. The relative phases of these waves are included in the complex amplitudes.

The complete performance of a filter can be determined by the following key elements. [reference handbook of filter]

1. Spectral transmittance.
2. Reflectance.
3. Absorbance.

4. Optical density curve of the materials.

To describe the radiation wave parameters we will take the direction cosines of ŝ propagation vectors of the transmitted wave ($\alpha_t\beta_t\gamma_t$) and for the reflected wave be ($\alpha_r\beta_r\gamma_r$). The phase factor will have the following form:

Incident wave $$e^{i\left[\omega_i t-\left(\frac{2\pi n_0}{\lambda_i}\right)(xsin\vartheta_0+zcos\vartheta_0)\right]}$$

Reflected wave $$e^{i\left[\omega_r t-\left(\frac{2\pi n_0}{\lambda_r}\right)(\alpha_r x+\beta_r y+\gamma_r z)\right]}$$

Transmitted wave $$e^{i\left[\omega_t t-\left(\frac{2\pi n_1}{\lambda_t}\right)(\alpha_t x+\beta_t y+\gamma_t z)\right]}$$

Satisfying all boundaries condition at z = 0 we will have that

$$\omega \equiv \omega_r \equiv \omega_t$$

This implies that the frequencies in reflection or refraction don't change and neither the free space wavelength, thus:

$$\lambda \equiv \lambda_r \equiv \lambda_t$$

Having the reflected beam and refracted beam in the plane of incidence, makes

$$n_0\beta_r \equiv n_1\beta_t \equiv 0$$

Then

$$\alpha = sin\vartheta \qquad \gamma = cos\vartheta \qquad n_0 sin\vartheta_0 \equiv n_0\alpha_r \equiv n_1\alpha_t$$

If we take the angle of reflection as ϑ_r and the angle of refraction ϑ_t, fulfilling all boundaries condition we will arrive to Snell's low:

$$n_0 sin\vartheta_0 = n_1\vartheta_t$$

In the further description of the optical parameters, we will use the concept of optical admittance of a medium given by y; in free space the optical admittance is given by:

$$\mathcal{Y} = \left({}^{\varepsilon_0}/_{\mu_0}\right)^{1/2}$$

Then for any medium, we will have that:

$$y = N\,\mathcal{Y}$$

1.3.2 Normal incidence.

In the case that the oncoming pane-polarized plane harmonic radiation is totally perpendicular to the surface of the filter, we have the normal incidence case. In this case since the direction of the propagation is the opposite of the reflected beam, the orientation of electric and magnetic field change with respect to the one that was in the incident beam. With not absorption media and applying all the boundaries condition for this case. We can calculate the Amplitude reflection and transmission coefficients denoted by ρ and τ respectively:

$$\rho = \frac{n_{0} - n_1}{n_0 + n_1}$$

And

$$\tau = \frac{2n_0}{n_0 + n_1}$$

For the normal incidence case $\tau$is always a positive real number and there is not phase shift between the incident and transmitted beams at the interface.

With an incident wave (λ), the normal incident spectral transmittance as it shown in **Figure 1.2**, T(λ) is determined by the ratio of the light intensity of the transmitted wave through the filter $I_T(\lambda)$ and the incident wave I_0 (λ), that's is:

$$T(\lambda) = \frac{I_T(\lambda)}{I_0(\lambda)} = \frac{y_1}{y_0}\tau^2 = \frac{4n_0n_1}{(n_0 + n_1)^2}$$

Where y_0 and y_1 are the optical admittance values of the incident medium and the filter respectively.

In the case of the reflectance, the calculation is similar:

$$R(\lambda) = \frac{I_R(\lambda)}{I_0(\lambda)} = \rho^2 = \left(\frac{n_0 - n_1}{n_0 + n_1}\right)^2$$

Finally, we have:

$$(1 - R) = T$$

1.3.3 Oblique incidence

Let's consider again a free-absorption media, any incident wave of arbitrary polarization can be split into two components. The transmitted and reflected beams components can be calculated for each separately for each orientation and then they can be combined. These two components are known as p-polarized if the wave have the electric vector in the plane of incidence and s-polarized if the electric vector is normal to the plane of incidence.

For p-polarized light, Appling all the boundaries conditions concerning to this case, we have the following expressions to calculate the important parameters:

$$\rho_p = \frac{\left(\frac{y_0}{cos\vartheta_0} - \frac{y_1}{cos\vartheta_1}\right)}{\left(\frac{y_0}{cos\vartheta_0} + \frac{y_1}{cos\vartheta_1}\right)} \qquad \tau_p = \frac{\left(\frac{2y_0}{cos\vartheta_0}\right)}{\left(\frac{y_0}{cos\vartheta_0} + \frac{y_1}{cos\vartheta_1}\right)}$$

$$R_p = \left[\frac{\left(\frac{y_0}{cos\vartheta_0} - \frac{y_1}{cos\vartheta_1}\right)}{\left(\frac{y_0}{cos\vartheta_0} + \frac{y_1}{cos\vartheta_1}\right)}\right]^2 \qquad T_p = \frac{\left(\frac{4y_0 y_1}{cos\vartheta_0 cos\vartheta_1}\right)}{\left(\frac{y_0}{cos\vartheta_0} + \frac{y_1}{cos\vartheta_1}\right)^2}$$

For s-polarized light we have:

$$\rho_s = \frac{(y_0 cos\vartheta_0 - y_1 cos\vartheta_1)}{(y_0 cos\vartheta_0 + y_1 cos\vartheta_1)} \qquad \tau_s = \frac{(2y_0 cos\vartheta_0)}{(y_0 cos\vartheta_0 + y_1 cos\vartheta_1)}$$

$$R_s = \left[\frac{(y_0 cos\vartheta_0 - y_1 cos\vartheta_1)}{(y_0 cos\vartheta_0 + y_1 cos\vartheta_1)}\right]^2 \qquad T_p = \frac{(4y_0 cos\vartheta_0 y_1 cos\vartheta_1)}{(y_0 cos\vartheta_0 + y_1 cos\vartheta_1)^2}$$

In resume if we consider a wave with not normal incidence direction (random polarized radiation), then the component of the intensity perpendicular to the interface most be used also to calculate the total transmittance and reflectance:

$$T(\lambda) = \frac{1}{2}(T_p + T_s). \qquad R(\lambda) = \frac{1}{2}(R_p + R_s)$$

While the density of a filter known also as absorbance can be calculated by:

$$D(\lambda) = \log \frac{1}{T(\lambda)}$$

1.3.4 Normal incidence in an absorbing media

As we mention before, materials have high level of absorption in the EUV and soft- x ray range, so we must describe the interaction of radiation with matter in more realistic situation. In our case, transmittance filters are placed more often in front of the pass of the radiation coming from the source, this is the perfect example for the description of an oncoming normal incident radiation in an absorbing media.

In the case of a filter, made by a certain number of layers (absorbing media) between to free absorbing media spaces, we have that the absorption on the filter is related to the transmittance and reflectance such that:

$$A + T + R = 1$$

For explaining better this case, let's start introducing the important parameter that will describe the condition of an absorbing media:

$$N_0 = n_0 - ik_0$$

$$y_0 = N_0\mathcal{Y} = (n_0 - ik_0)\mathcal{Y}$$

Medium 0

$$N_1 = n_1 - ik_1$$

$$y_1 = N_1\mathcal{Y} = (n_1 - ik_1)\mathcal{Y}$$

Medium 1

Applying boundary conditions, the expression for the amplitude coefficients can be obtained:

$$\rho = \frac{(n_0 - n_1) - i(k_0 - k_1)}{(n_0 + n_1) - i(k_0 + k_1)}$$

$$\tau = \frac{2(n_0 - ik_0)}{(n_0 + n_1) - i(k_0 + k_1)}$$

And the values of reflectance and transmittance are given by:

$$R = \left(\frac{y_0 - y_1}{y_0 + y_1}\right)\left(\frac{y_0 - y_1}{y_0 + y_1}\right)^*$$

$$T = \frac{4y_0 Re(y_1)}{(y_0 + y_1)(y_0 + y_1)^*}$$

Since we are considering the media 0 be a non-absorbing media, y_0 is real.

1.3.5 Oblique incidence radiation in an absorbing media

As in the last section, in this case, we are assuming non absorbing incident medium and an absorbing emergent medium.

For this case, since p-polarized radiation and s-polarized radiation are treated independently, the introduction of tilted admittance terms (η) must be made, so we have:

$$\eta_p = \frac{N\mathcal{Y}}{cos\vartheta}$$

For p-waves

$$\eta_s = N\mathcal{Y}cos\vartheta$$

for s-waves

Where N and ϑ follows Snell's law, such as:

$$N_0 sin\vartheta_0 = N_1 sin\vartheta_1$$

Using η_p or η_s by η for either plane of polarization and being η_0 real for a not absorbing incident media, we have the terms for transmittance or reflectance for an oblique incoming radiation:

$$R = \left(\frac{\eta_0 - \eta_1}{\eta_0 + \eta_1}\right)\left(\frac{\eta_0 - \eta_1}{\eta_0 + \eta_1}\right)^* \qquad T = \frac{4\eta_0 Re(\eta_1)}{(\eta_0 + \eta_1)(\eta_0 + \eta_1)^*}$$

When the wave travel a distant d normal to the boundary it will experience a phase shift given by:

$$-2\pi Nd\frac{cos\vartheta}{\lambda}$$

1.3.6 Transmittance, reflectance and absorptance of thin films assembly.

If we extend the analysis of a single boundary to the case of a certain number of parallel films of materials, then we will have that with the existence of two or more interfaces and several beams will be produce by internal reflected and transmitted light as we can appreciate in fig n. In a thin film assembly, the interference effects can be detected in the reflected or transmitted light. The best approach for analyzing this kind of systems is using the matrix formulation of the boundary conditions at the film surfaces derived from Maxwell's equations [13].

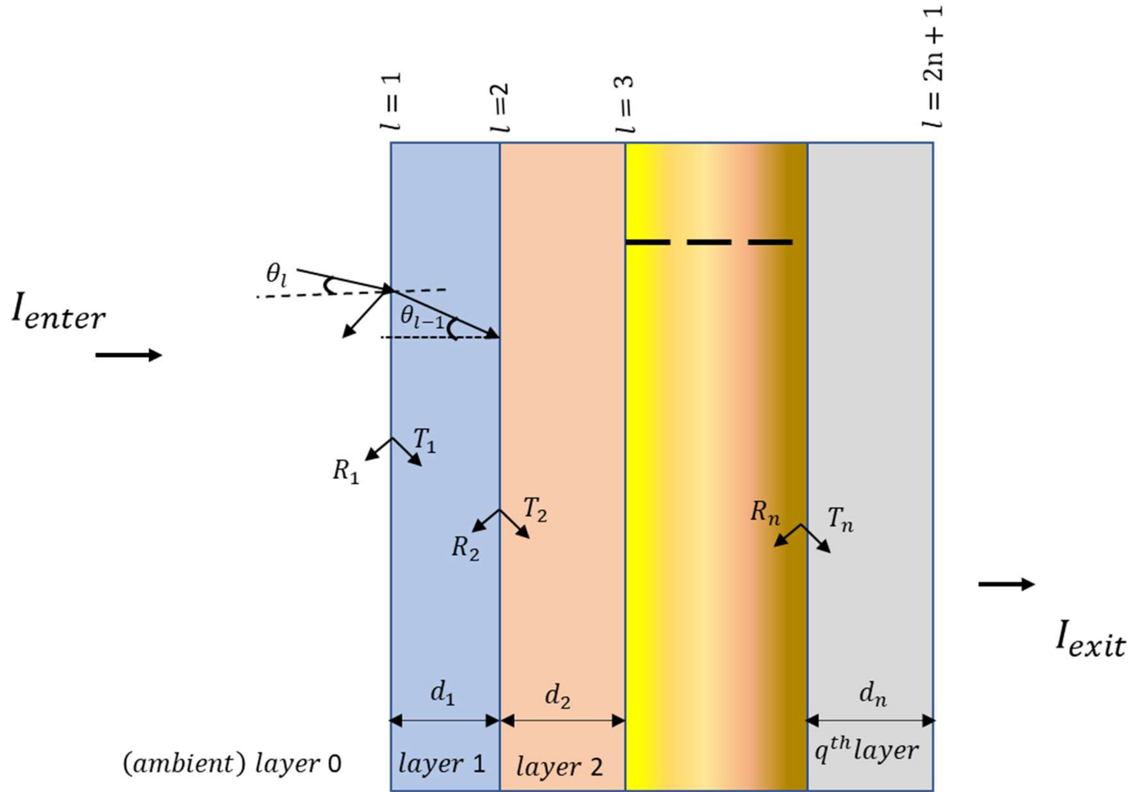

Figure 1.3 Diagram of specular transmissions and reflections for a thin film assembly.

Let's considering a thin film assembly consisting of n number of layers, the incident radiation (I) enter to the system with an angle θ and wavelength (λ); the characteristic matrix that describe one layer and the interfaces that limit that layer (l) have the following structure:

$$\begin{bmatrix} E_l/E_{l+1} \\ H_l/E_{l+1} \end{bmatrix} = \begin{bmatrix} B \\ C \end{bmatrix} = \begin{bmatrix} cos\delta_r & isin\delta_r/\eta_r \\ i\eta_r sin\delta_r & cos\delta_r \end{bmatrix} \begin{bmatrix} 1 \\ \eta_{l+1} \end{bmatrix}$$

Where

$$\delta_r = \frac{2\pi N_r d_r cos\vartheta_r}{\lambda}$$

$$\eta_r = \mathcal{Y} N_r cos\vartheta_r$$

For s-polarization

$$\eta_r = \frac{\mathcal{Y} N_r}{cos\vartheta_r}$$

For p-polarization

For a q number of layers, the characteristic matrix of the system will be the product of the all individual matrices following the correct order, so:

$$\begin{bmatrix} B \\ C \end{bmatrix} = \left\{ \prod_{r=1}^{q} \begin{bmatrix} cos\delta_r & isin\delta_r / \eta_r \\ i\eta_r sin\delta_r & cos\delta_r \end{bmatrix} \right\} \begin{bmatrix} 1 \\ \eta_{l+1} \end{bmatrix}$$

Where

$$\eta_{l+1} = \mathcal{Y} N_{l+1} cos\vartheta_{l+1}$$

For s-polarization

$$\eta_{l+1} = \frac{\mathcal{Y} N_{l+1}}{cos\vartheta_{l+1}}$$

For p-polarization

In the system the Snell's low is always fulfilled.

Finally, for a thin film assembly or multilayer structure, the reflectivity, transmission and absorptance terms respectively, are given by:

$$R = \left(\frac{\eta_0 B - C}{\eta_0 B + C}\right)\left(\frac{\eta_0 B - C}{\eta_0 B + C}\right)^*$$

$$T = \frac{4\eta_0 Re(\eta_{l+1})}{(\eta_0 B + C)(\eta_0 B + C)^*}$$

$$A = \frac{4\eta_0 Re(BC^* - \eta_{l+1})}{(\eta_0 B + C)(\eta_0 B + C)^*}$$

1.3.7 Potential transmittance of thin film assembly.

The potential transmittance of any system (single layer, multilayer) correspond to the ratio between the irradiance leaving the system and the irradiance entering to the system.

The potential transmittance in a filter fabricated with more than one layer can be calculated by the product of the independence transmittance of each layer, taking in account the optical properties of each layer. For a q layer system, the potential transmittance is given by:

$$T_{potential} = T_1 T_{2 \ldots\ldots} T_{q-1} T_q$$

1.4 High brilliance sources for EUV radiation.

Synchrotrons and Free electron lasers (FEL's), are the higher technologies of third and fourth generation high brilliance sources.

A synchrotron is a particle accelerator that produce light with very high-intensity, ultra-bright radiation; this light in the scientific community is called synchrotron radiation. The synchrotron radiation is emitted by an electron traveling nearly speed of light, when its path is bent by a magnetic field when passing through different magnetic devices such as undulators, wigglers and bending magnets. The resulting light, ten billion times brighter than that supplied by conventional sources. The light can be provided from a wide wavelength range, depending on the facility can reach from the infrared to hard x-rays. The radiation beams are collected by in-vacuum optical systems and propagate through beamlines to reach experimental stations. In these stations (beamlines) different analytical and processing techniques are available.

Synchrotron have a big range of applications, based in research methods such as imaging, spectroscopy and scattering, in fields like:

- Life sciences
- Lithography
- Semiconductors and electronics devices
- Physics
- Material sciences
- Chemistry
- Earth and environmental sciences
- Pharmaceutics and medical sciences
- Industrial applications.

The reason of why synchrotron radiation is useful in many applications is because their multiple properties which still cannot be reached for compact-home lab sources:

- Very high brilliance
- Pulse time structure
- Natural collimation
- High degree of polarization
- Coherence
- Precise tunable wavelength

Based in synchrotron radiation, a higher technology facility are the Free electron lasers (FEL's). Fels's are designed to produce very fast bunches of light with extremely high peak brightness, pulses with a peak brightness ten billion times higher than that made available by third-generation light sources. In FEL's, the radiation light is used to feed an undulator in order to produce the optical amplification. Depends on the facility FEL's can produce radiation with wavelength ranging from the terahertz region until the hard X-ray region.

One big advantage of an FEL's in comparison with a conventional laser is the free tunability of the wavelength by simply changing the electron energy [**26, 27**], but more than that, FEL's light provide very useful properties like:

- Wide tunability range, depending on the facilities, from 100 to 0.1nm, in case of X-ray FEL's 10 to 0.1nm
- Transverse and longitudinal coherence
- High peak power, tens to hundreds GW
- Short pulse length, 1 to 100 fs

In the EUV and x-ray range, FEL's opens the door to the ultra-small and ultra-fast word. Some application of FEL's are:

- The transverse coherence and large number of photons make possible to image periodic and non-periodic structures at the nanometer and sub-nanometer scale.
- Using fast, single shot imaging, one can follow the dynamics of these phenomena, and overcome the limit set by sample damage.

- Nonlinear phenomena and high energy density systems can be studied using the short pulse duration and large peak power.
- The X-ray FEL can be used to explore matter at atomic molecular scale with unprecedented space-time resolution. [27]

For all these applications, high brilliance sources such as synchrotrons and free electron lasers (FEL) are very important nowadays for the development of science and technology such as the development of EUV Lithography, EUV metrology, research in materials science, chemical technology, biophysical science, medical applications, surface studies, and solid-state physics.**[7, 28].**

One example of FEL's facility is FERMI, located at ELETTRA synchrotron scientific campus in Italy. FERMI is based in a double cascade seeded source. In case of FERMI and many other FEL's facilities with similar technology, light at the selected wavelength is mixed with a small fraction of the seed photons reaching the experimental chamber, also is mixed with the light from the first stage and a fraction of higher harmonics, so transmittance filters (band pass filters) must be introduced to ensure the specific wavelength range that the experiment demands and to ensure the quality of the beam **[29, 30]**

In fig 4, a map with the FEL's facilities around Europe is shown.

Figure 1.4 FEL's facilities available to users in Europe. **www.leaps-initiative.eu/fels/european_facilities/**

2. Thin film transmittance filters: design

2.1 Choosing Materials.

The optical properties of any filter depends, of course, on the materials you are using to fabricate them; the correct selection of the materials is done following the requirements of the source. For our research these requirements are such:

- **Wavelength Target**: We decide to design transmittance filters, suitable for FEL 2, one of the two sources at FERMI free electron laser. Normally FEL 2 works between 4-20 nm wavelength range but can go even lower. Our target spectral range is between 4-20 nm.
- **Fragility**: Since materials possess high absorption in the EUV spectral range, transmittance performance of the filters increase with the decrease of the thickness of the materials, but with a small thickness the fragility of the material increase. So, the materials chosen should be tough enough to ensure the mechanical stability of a nanometric thin films, with the correct thickness able to select suitable spectral bandwidth or reject harmonics.
- **Oxidation and carbonation contamination**. Filter are exposure to difference sources of contamination during their use. Contamination from air, water, carbon, can reduce the performance of the filters and contribute to the production of higher harmonics photons. Chosen materials should be if it is possible resistant to wear and not reactive when they are expose to these types of contaminants [10, 12]. Another option is adding a protective coating to the filter.
- **Exposure time to high energy and aging:** High brilliance sources are specials because their high power and high intensity peak radiation. Optical systems for high energy power sources could present damages and induce fast aging of the materials. The materials chosen, have to possess high mechanical and thermal stability to high power to ensure a good performance and lager useful life period [14].

Taking in account all those requirements we procced to simulate the transmittance performance of different materials in the targeted wavelength range, from 4.5nm (carbon k-edge) to 20 nm.

Simulations are done using an open-access software product called IMD package (http://www.esrf.eu/Instrumentation/software/data-analysis/xop2.3) [31-32]. IMD is a versatile software that allows you, among another options, to manually modeling the layers of your filters device and simulate their transmittance, reflection and absorption response to the desire wavelength range, using the optical constants of the different elements located in their database. This optical constant can be based on theoretical calculations or experimental data added by different scientist along the years.

As we mentioned before, since materials have high absorption, finding materials that fulfill all the high brilliance sources requirement is quite challenging. Some materials as Beryllium and other rare earth are suggested to be a good candidate for transmittance filters in this ranges, but the toxicity of rare earth materials make very difficult and dangerous the fabrication of such filters.

In **Figure 2.1** and **Figure 2.2** we can appreciated the theoretical transmittance response of different material. The fit parameter was the thickness of the layers. All simulated filters have 100 nm thickness.

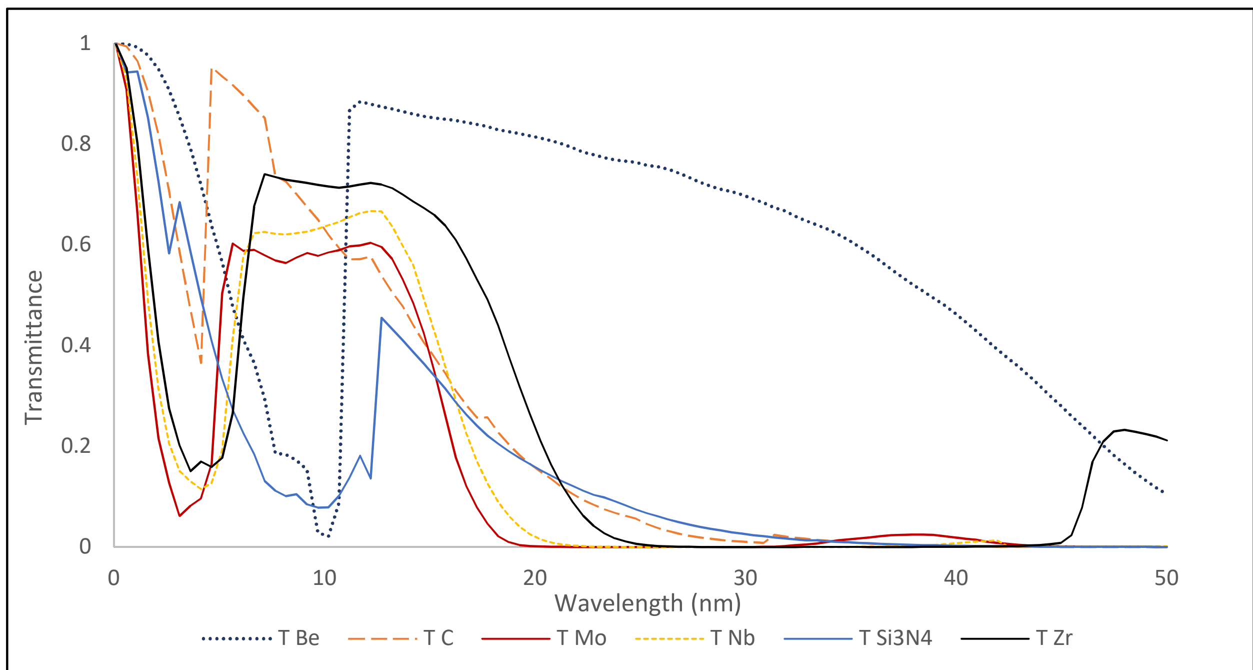

Figure 2.1 IMD simulations of Transmittance performaces for 100 nm single layer filters of differents materials, 4 to 50 nm spectral range .

We realized that some materials have high transmittance response, in the targeted wavelength range, but they are less tough, while other have lower transmittance response but are stronger and more thermally stable. So, instead of going after single layer transmittance filter, we decided to fabricate bilayer structures, combining materials to enhance their best properties and obtain filters with good transmittance and high mechanical strength and thermally stable.

Using the evaluation of the transmittance performance together with the mechanical strength of the materials, the possibility of fabrication in the available facilities for the project, the free toxicity of the elements; Zr and Nb were selected as chosen materials for the fabrication. In Fig 6 is shown the comparison of the transmittance response of the bilayer structures Zr/Nb and Nb/Zr in contrast with other single layer filters.

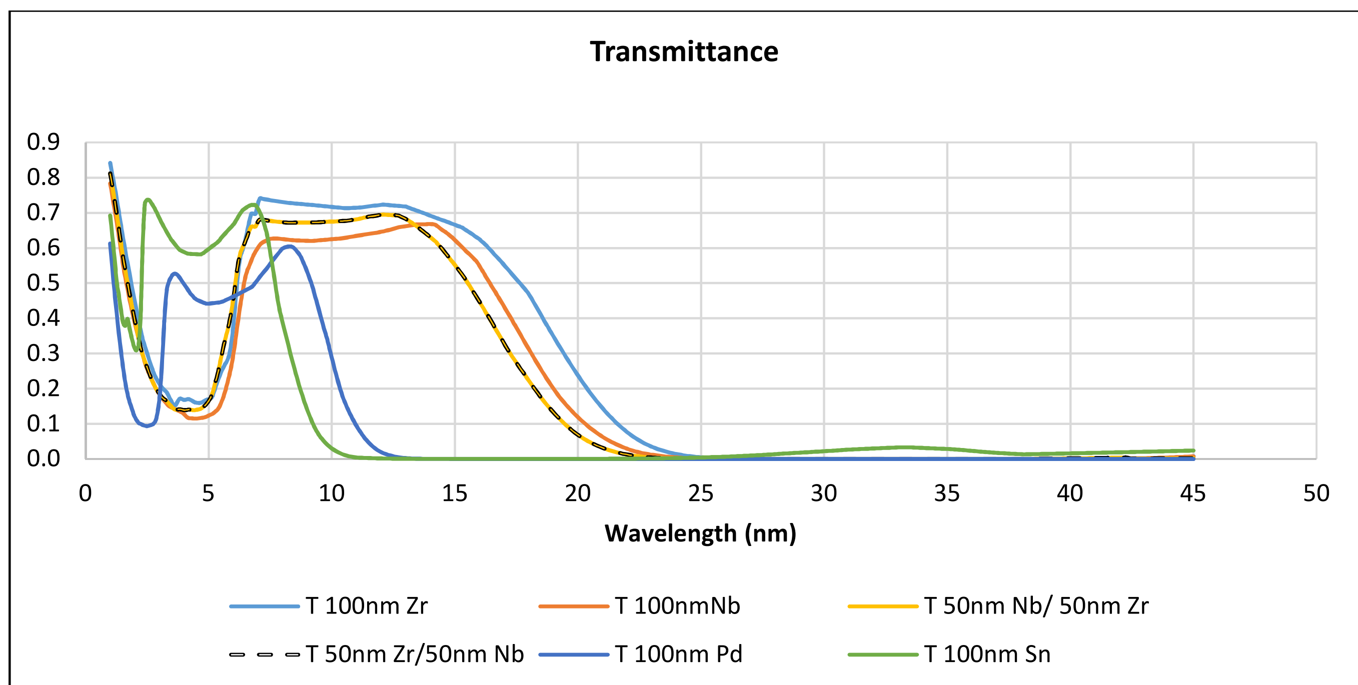

Figure 2.2. IMD simulations of Transmittance performaces for a total thickness of 100 nm filters of differents materials, some single layers and some bilayer filters., from 2 to 45 nm spectral range

Nb and Zr have a higher melting point and better thermal stability than other materials like Palladium or Tin, also used for thin film filters **[10, 13, 33]**. Both are suited for e–beam deposition and sputtering techniques. Zr and Nb are two of the few materials with proper optical, chemical and mechanical properties for being an option for transmittance filters in the range 4-20 nm wavelength.

In this Research study, the combination of Zr and Nb formed by bilayer structures is intended to obtain filters with better mechanical properties, strong enough to achieve the fabrication of thin self-standing filters and high thermal stability to fulfill FEL's requirements. Single layer filters of Zr and Nb will be also studied in other to understand better the optical and mechanical performance of the bilayer structures filters.

For the fabrication of the filters we have used Si_3N_4 membranes as substrates, which provides extra mechanical support to the sample's fabrication process.

In **Figure 2.3** a schematic diagram of the structural design of the filters is presented. We have shown the bilayer structures formed by Nb/Zr and Zr/ Nb and the single layer of Nb and Zr on Si_3N_4.

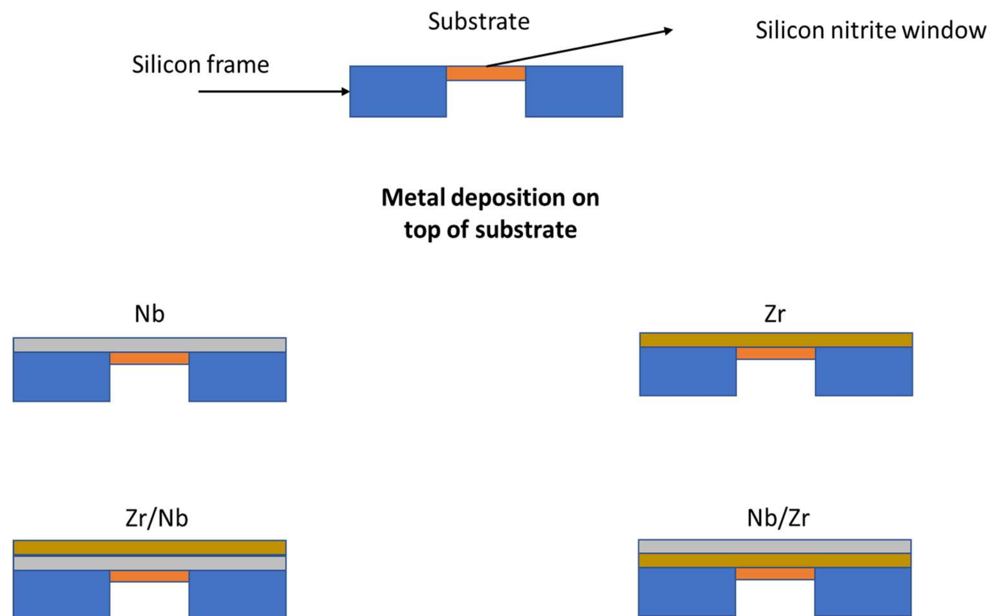

Figure 2.3 Structural design of the samples.

2.2 Niobium

Chemical elements with symbol Nb and atomic number 41, is a transition metal that belongs also to the group called refractory metals. Refractory metals are a class of metals that are extremely resistant to heat and wear. Niobium is a crystalline and very ductile. Pure Niobium has a hardness like the pure titanium. Niobium oxidizes in the earth's atmosphere very slowly. The most common oxides formed in thin films is Nb_2O_5. Principal properties of Nb are listed in table 2.1

Some application of Nb are:

- **Iron and steel industry**

  About 85% to 90% of niobium in the world is used for iron and steel production as a form of niobium iron. The steel can increase more than 30% of strength by adding 0.03% - 0.05% niobium.

- **Superconducting materials industry**

  Some niobium compounds and niobium alloys have high superconducting transition temperature, which is widely used in the manufacture of various industrial superconductors, such as superconducting generator, high power accelerator magnets, superconducting magnetic energy storage, magnetic resonance imaging equipment.

- **Aerospace Industry**

  Aerospace industry is the main application area of high purity niobium, mainly used for manufacturing engines and heat resistant components rockets and spacecraft. Nb - and Ta - based hot - alloys have excellent thermal resistance.

- **Atomic energy industry**

  Niobium has a high thermal conductivity, high melting point, good corrosion resistance, and low neutron capture cross section. It is a material that is well suited for atomic reactors.

- **Electronic industry**

Niobate ceramics can be used in production of capacitors. Single crystal of lithium niobate and potassium niobate compounds have good crystal, piezoelectric, pyroelectric and optical properties. Has been widely applied to infrared, laser technology and electronic industry. In addition, niobium has high melting point, high emission electron capacity. It can be used to make electron tubes and other electronic vacuum devices.

- **Medical field**

Niobium has anti - corrosive physiological and good biological compatibility, which are often used in the manufacture of bone plate, skull plate screw, plant root, surgical instruments etc.

- **In other areas:**

  - Nb helps to increase the transmittance of lenses, is also used in the manufacture of lenses in the optical industry.
  - Nb can also be applied to the lighting industry, such as Nb and 1% Zr alloy can be used for producing precision support of high strength sodium vapor lamp, these small parts have excellent heat resistance to sodium vapor corrosion. **[34 35]**

Table 2.1 Principal properties of Nb, table founded at http://www.rsc.org/periodic-table/element/41/niobium

Group	**5**
Period	**5**
Block	**d**
Atomic number	**41**
State at 20°C	**Solid**
Electron configuration	**[Kr] $4d^4 5s^1$**
Melting point	**2477°C, 4491°F, 2750 K**
Boiling point	**4741°C, 8566°F, 5014 K**
Density (g cm−3)	**8.57**
Relative atomic mass	**92.906**
Key isotopes	**93Nb**

2.3 Zirconium (Zr)

Zirconium is a silver-gray transition metal, very strong but malleable, ductile and easily forms stable compounds. It is flammable in powder form, and highly resistant to corrosion and heat but oxidizes very fast in contact with air. The most common oxidation states in thin film is ZrO_2

The main commercial use of zirconium is as zircon.

- Zircon is widely used in refractories, ceramic opacification and foundry sands. Zirconium is also used as an alloying agent in materials that are exposed to aggressive environments.

- Zr forms a variety of inorganic and organometallic compounds. Zirconium dioxide (ZrO2, Zirconia) can withstand very high temperatures and is used to make crucibles and to line the walls of high temperature furnaces.

- Zr is use as transmittance filter for laser sources. **[36]**

- Zirconium is used in nuclear reactors due to its low neutron absorption cross section and resistance to the corrosive environment encountered within nuclear reactors. Nuclear power generation applications account for more than 90% of commercial zirconium production.

Table 1.2 Principal properties of Zr, table founded at http://www.rsc.org/periodic-table/element/41/niobium

Group	**4**
Period	**5**
Block	**d**
Atomic number	**40**
State at 20°C	**Solid**
Electron configuration	**[Kr] $4d^2 5s^2$**
Melting point	**1854°C, 3369°F, 2127 K**
Boiling point	**4406°C, 7963°F, 4679 K**
Density (g cm−3)	**6.52**
Relative atomic mass	**91.224**
Key isotopes	**90Zr, 92Zr, 94Zr**

2.4 Nb and Zr, filters background.

Single foils of Zr and Nb are being used as transmittance filters and have been tested in different wavelength ranges, for applications of extreme ultraviolet high-volume lithography instrumentation and in FELs **[10,14, 15, 20-23, 33]**, but Zr/Nb or Nb/Zr bilayer structures have not been tested yet for any of these applications.

In 2001 Forbes R Powel and Terry A. Johnson, presented Zr films of around 100 nm supported by a Ni mesh reporting 48% of transmittance at 13.4 nm, used as filter windows for lithography application **[14]**. In 2007 V.P Belik et al. showed some results for 100 nm Nb and Zr filters supported by Si_3N_4 membranes with transmittance peak of 30% around 13nm. They also presented a 240 nm thickness Nb/Si multilayer

(6 nm Nb, 6 nm Si; 20 pairs), supported by a gold mesh with 18% of transmittance near 11 nm and approximately 45% around 13 nm, as filter for nanolithography **[22].** Furthermore, Wu Heyun, also in 2007 presented self- supporting Zr filters, for soft x- ray laser applications, but with higher thicknesses 300, 400 and 500 nm; the thinnest one showing the highest, 35% peak transmittance around 13.5nm **[20].** In 2011 Yonggan Wu et al. presented Zr filters supported by a Polyamide film with 10.5% transmittance around 13 nm and 14% around 11 nm, looking for filter materials for soft x ray **[23]**. In addition, in 2011, N.I. Sckhalo et al, fabricated different multilayers structures based on Mo/$ZrSi_2$ combinations, with a transmittance peak of around 72% near 13nm, but very low transmittance for the range between 5-10nm **[21]**. In 2012 Brose S. et al. achieved free-standing Nb filters tested at 11 nm with 48% of transmittance **[15]**. In 2015, C. Tarrio, fabricated Zr filters of 250 nm supported by Cu mesh, pursuing better mechanical structure; These filters have a maximum peak transmittance of 48% **[10].**

3. Experimental

The following chapter covers the fabrication of the samples on the one hand and the methods for characterization on the other hand. The sample fabrication procedure was not the same for all experiments. Hence first a typical process is introduced, then deviations from this process for certain experiments are explained. The characterization methods mainly divide into 3 parts: the mechanical, structural and the optical transmittance characterization.

3.1 Filters fabrication.

The fabrication procedure to fabricate the samples is shown in the schematic diagram, **figure 3.1**.

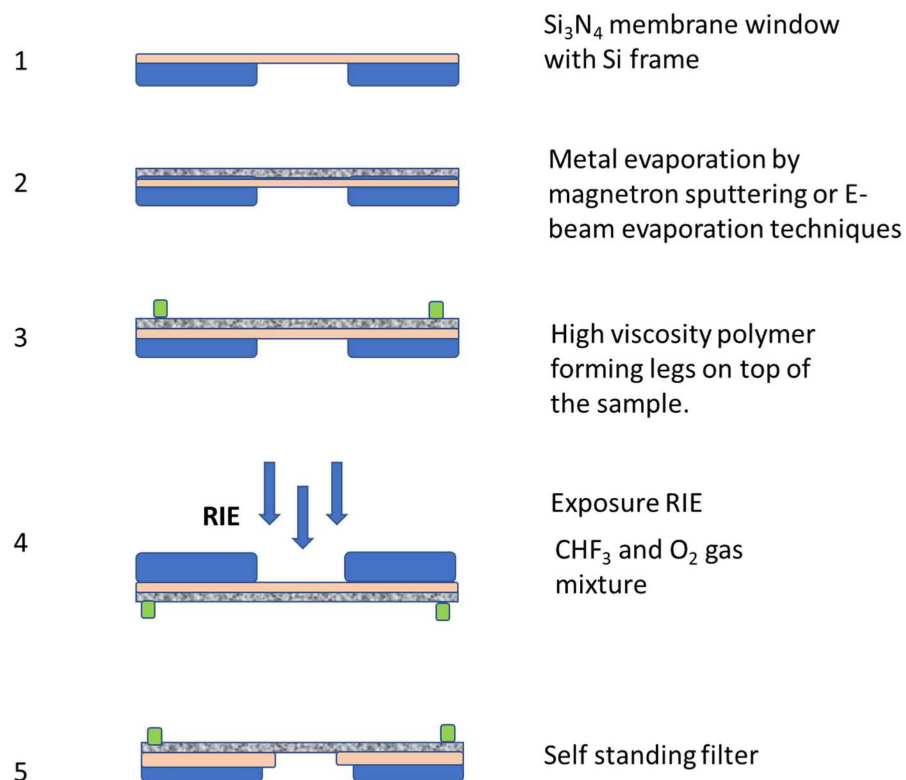

Figure 3.1 Schematic diagram of the simplified fabrication process of the free self-standing filters.

Using a Si_3N_4 membrane as substrate (step 1), we proceed with the evaporation of the metal layers on top of the substrate by using magnetron sputtering (step 2) or E-beam evaporation technique. Four polymer dots are deposit with a small needle to protect the front of the top layer of the filter, since filter must be turned over in other to procced with the RIE process in the backside of the sample (step 3). To obtain a free self-standing filter, the Si_3N_4 substrate must be etched. Reactive ion etching (RIE) (step 4) has been applied on the membrane backside in order to open a window in the silicon nitride. A continuation we will describe in detail step by step the fabrication process.

3.1.1 Step 1. The Substrate.

Silicon nitride (Si_3N_4) membranes from Silson Ltd, Company specialized in the fabrication on this kind of membranes, were used as a substrate for the fabrication of several Zr, Nb, Nb/Zr and Zr/Nb thin films filters with different thicknesses. The substrate used has 7.5mm X 7.5mm silicon frame with 3mm X 3mm Si_3N_4 membrane window on the center. The Si_3N_4 membrane window is about 100 nm thickness while the silicon frame is about 200 µm thickness.

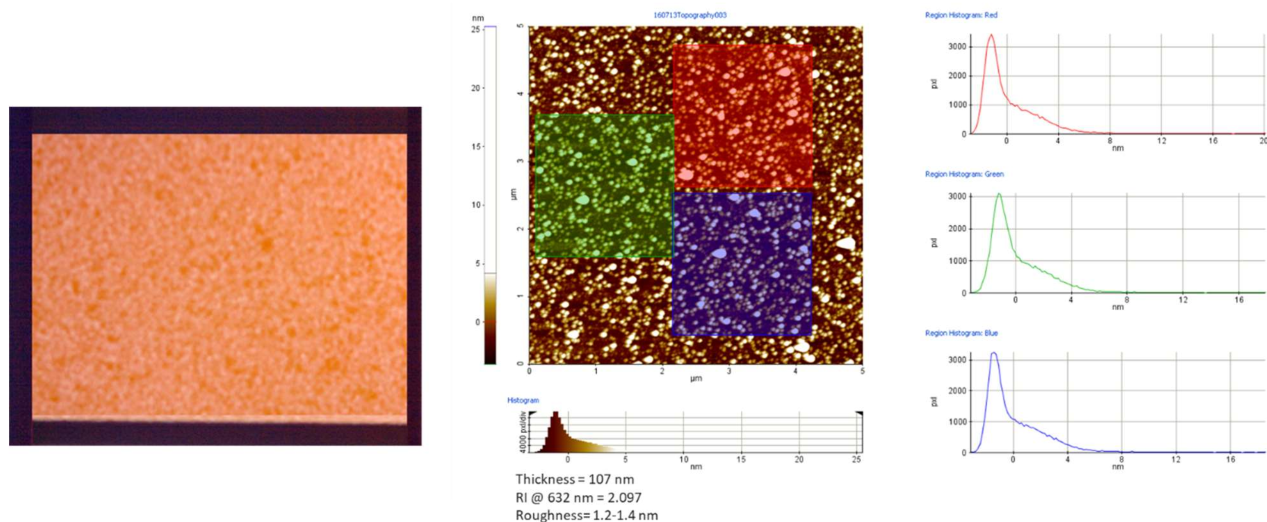

Figure 3.2 Left, optical microscope image of a Si_3N_4 membrane used as a substrate for the fabrication of the filter samples. Right AFM image and measurements of the membrane.

Membranes were bought in packages of 50 membranes. AFM not contact images were taken to one membrane for having an idea of the topography of the substrate; the roughness measured of the membranes were about 1.2-1.4 nm.

Since membranes windows are very fragile, we designed custom-made holders which were used to handle the samples during the metal evaporation and characterization, ***Figure 3.3***. Holders were fabricated with aluminum (body part) and Bronze (clamps). The design of the holder is presented in **Figure 3.3**

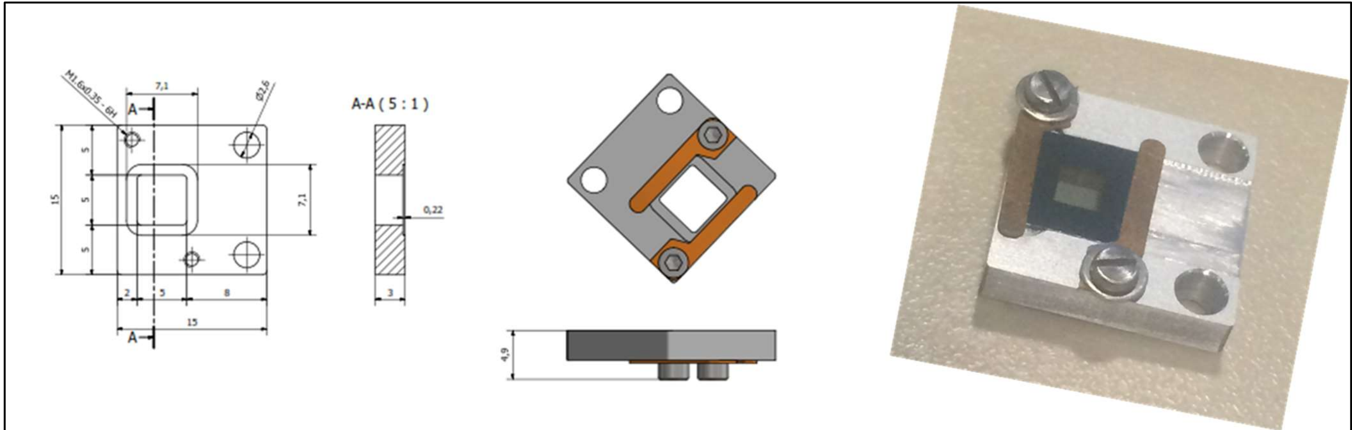

Figure 3.3 Custom-made holder.

3.1.2 Step 2. Metal evaporation of the thin film layers.

Of the many methods that can be applied for the deposition of metal materials, magnetron sputtering, and electron beam evaporation are the most widely used. These two methods are the one we have used to fabricate the samples utilized in the different experiments.

- Magnetron RF sputtering technique was used to fabricate all the examples of the experiment 1 (described in chapter 4).
- E beam evaporation technique was used for the fabrication of the rest of the samples, samples utilized in the TEM structural characterization (chapter 5) and in the experiment 2 (chapter 6).

Further discussion and description of these two methods are provided in the subsequent sections.

3.1.2.1a RF Magnetron Sputtering deposition technique

Magnetron sputtering is a Plasma Vapor Deposition (PVD) process, is one of the most versatile techniques used for the deposition of metallic films, when device quality films are required. The principle of this technique is shown in Figure 11, left. Substrates are placed in a vacuum chamber facing the target which is composed of the material to be deposited. The metallic target is placed on a magnetron in an inert gaseous atmosphere. The magnetron generates plasma at the surface of the target, the gas ions present in the discharge knock off the target material with sufficient force to dislodge and eject atoms from the target which consequent will condense on the surfaces that are placed in proximity to the magnetron sputtering cathode (where the substrate is placed). The plasma is generated with an argon atmosphere at pressures typically between 1 and 10 mTorr. By controlling the argon flow, target power, deposition time, and substrate temperature, the film thickness and deposition rate can be tailored. This method allows for a wide range of film thicknesses from tens of nanometers to a few micrometers.

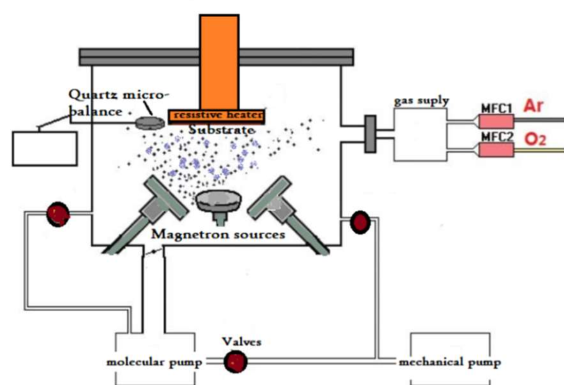

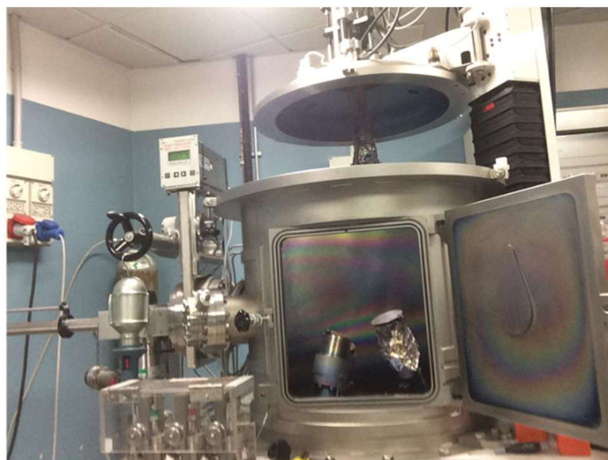

Figure 3.4 Left, schematic diagram of a Magnetron RF sputtering. On the right, Magnetron RF sputtering used for the deposition of the samples at the d*epartment of Molecular Sciences and Nanosystems, Ca' Foscari University of Venice, Italy.*

Magnetron sputtering process produces films with higher purity and better controlled composition, provides films with greater adhesion and homogeneity and permits better control of film thickness [1-4lucius].

3.1.2.1b Magnetron sputtering set-up and deposition process.

A set of samples were fabricated by using magnetron sputtering evaporation technique at the *Sputtering Lab of the Department of Molecular Sciences and Nanosystems, Ca' Foscari University of Venice, Italy.* A picture of the set-up is shown in Figure 11, right. Sputter depositions were performed in a custom-built radiofrequency (RF) magnetron sputtering system (13.56 MHz), equipped with three independent circular (2-inch in diameter), water-cooled, planar magnetron sources and a rf-biased sample holder. The cylindrical process chamber (equipped with a load-lock system) has both the diameter and the height equal to 60 cm, it is evacuated by the concurrent action of a turbomolecular pump and a cryogenic one. Throttle valves are placed between the pumps and the chamber to control the pumping speed. The base pressure in the chamber was in the range $1–10 \times 10^{-5}$ Pa. Depositions were performed using pure Ar (99.9995%) at a total working pressure around 50×10^{-2} Pa. The working pressure was maintained by the cryogenic pump; during the deposition, an additional and masked magnetron sputtering DC source (loaded with a pure Ti target) was also working in order to decrease the partial pressure of residual reactive gases, mainly oxygen, present in the vacuum chamber. The targets used on the two independent rf-sources were a 2-inch diameter Nb (99.95%) and Zr (99.5%) metallic disk, ¼-inch thickness. The lower purity of Zr target is mainly due to the well-known difficulty to produce Hf-free zirconium: the presence of Hf atoms in all the Zr-deposited films was confirmed by Rutherford backscattering spectrometry (RBS), showing in all films a Hf/Zr ratio of about 1%. The rf-power applied to the targets was 30 W, for deposition time ranging from 85 to 350 min. The two sources were both operated in an unbalanced-magnetron configuration. Film deposition was performed at room temperature in an off-axis configuration; the 4 inches diameter substrate holder, rotating at 10 rpm, was placed above the sources. At first, sources were conditioned for 20 min at the operating conditions to remove residual surface contaminations on the targets. For both sources, the deposition rate was of about 30 nm/h. Twelve depositions were performed, three for each kind of composition: Zr, Nb, Nb/Zr, and Zr/Nb considering 2 different thicknesses for each one; several samples were deposited at the same time, for a total of **30 samples analyzed**. Samples for experiment described in chapter 4 were fabricated with this technique.

3.1.2.2a E-beam evaporation technique

Electron beam evaporation (E-beam) is a Physical Vapor Deposition (PVD) technique. The E-beam machine consists of two main sections; an electron source (electron gun) and the deposition chamber. The

high-vacuum EB deposition system have a main chamber pumped using an ion pump and a Ti sublimation pump, and a load-lock chamber pumped using a turbo pump and a rotary pump. The background pressure of the main chamber was 4 × 10−9 Pa with the use of a liquid N2 shroud. The deposition rate and the thickness of the layer can be controlled using a crystal-oscillation-type film thickness controller. In this technique an intense electron beam is generated from a charged tungsten filament and steered via electric and magnetic fields to strike source material at the crucible and vaporize it within a vacuum environment. At some point as the source material is heated via this energy transfer its surface atoms will have enough energy to leave the surface. Atoms will traverse the vacuum chamber, at thermal energy (less than 1 eV), and will be deposited at the substrate positioned above the evaporating material. Average working distances are 300 mm to 1000mm. The deposition geometry mainly influences the ultimate film uniformity [**37**]. A schematic draw of an E-beam evaporator is shown in Fig 12, Left.

.

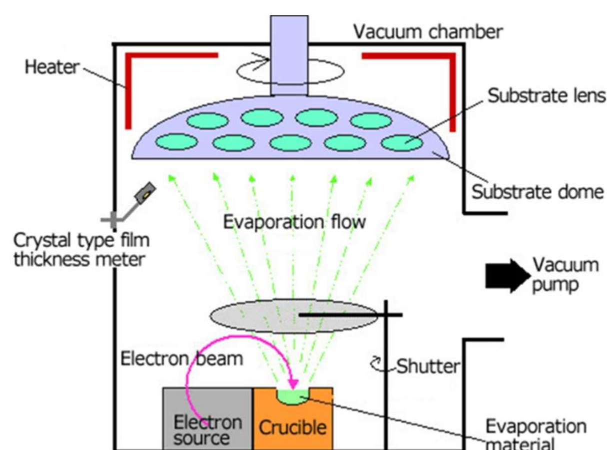

Figure 5 Left, schematic diagram of an Electron Beam evaporation device, image taken from https://www.jeol.co.jp/en/science/eb.html**. On the right, E-beam evaporator Balzers (Pfeiffer) PLS 500, used for the deposition of the samples. The device is located at the Helmholtz Nano Facility (HNF), Julich Forschungzentrum, Germany.**

The differences between these two types of deposition technique is shown in table 3.1

Table 2.1 Main differences between a sputter deposition system and E-beam evaporation system [58mewael].

Sputtering	E-beam
Stable rates	Deposition rates can vary
suitable sputtering for high melting point materials	Requires very high temperature for melting and this causes instability of rates
Thickness control by timing	Needs error compensation for the in-situ thickness monitor
Substrate holder rotates past sputter source	Needs shutter in front of the source
Good thickness uniformity requires large chamber diameter	Good uniformity over large areas
Kinetic energy of deposition often > 100 eV can be adjusted	Kinetic energy smaller than 0.5 eV not adjustable
Surface smoothing can be performed by ion gas bombardment	Ion polishing added for smoother boundaries

3.1.2.2b E-Beam evaporation set-up and deposition process

A set of samples were fabricated by using e-beam evaporation instrument: high vacuum Balzers (Pfeiffer) PLS 500 at clean room the Helmholtz Nano Facility (HNF), Julich Forschungzentrum, Germany. A picture of the set-up is shown in Figure 12 right.

Nb and Zr layers were deposited without heating the substrate in this experiment. Nb pellets of 10 mm with purity of 99.9% and Zr pellets of 8 mm with purity of 99.2% were used for the evaporation of this set of samples. The deposition rate of Nb and Zr was 0.3 nm/s. The pressure during evaporation was kept on the order of $\sim 10{-}7$ Pa. Machine was working at 25% of maximum power, high output voltage of 9.99 KV and current at the source was of 174 mA.

Different set of samples were fabricated using this method of evaporation technique to try out the etching procedure until we reached the perfect parameter for etch correctly the samples. Finally:

- One set of 4 samples was used for TEM structural study, these samples were not etched.
- One set of samples 5 samples were used for experiment 2 described in chapter 6.

3.1.3 Step 3. Placement of polymer "legs".

A high viscosity polymer dots were placed in the four corners of the top layer of the sample, in order to avoid that the surface of the sample get damage during RIE process. For the RIE process samples must be turned over with the backward side facing up, so can be hit it by the plasma of mixture gases to etch the membrane. The polymer legs avoid the contact of the top layer with the RIE floor chamber. PMMA AR-P was used to form the polymer "legs". The polymer dots were place it with the help of a rounded needle.

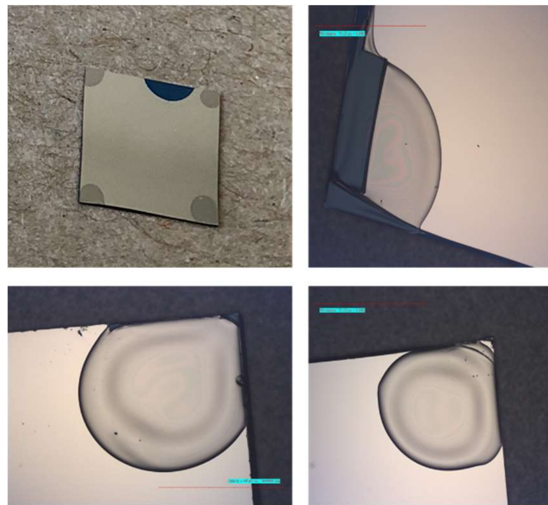

Figure 3.66 In the left top image, the four polymer dots can be appreciated, the 3 other images are optical microscopy images of the samples showing each one a corner with the polymer dots.

3.1.4a Reactive Ion Etching (RIE)

In a reactive ion etcher, samples are collocated on a cathode which is capacitively coupled to a radio-frequency generator, while the anode is grounded. Free electron, which are accelerated with an electric field collide with the gas molecules, ionize them and initiate a plasma of a mixture of gases. Ions and reactive neutral radicals start to bombard the surface almost at normally direction and etch the expose part of the surface.

3.1.4b Etching process

For the first experiment (samples fabricated using magnetron sputtering technique) the etching procedure to free the metal thin films from the silicon nitrate membrane substrate was performed at the Institute for Photonics and Nanotechnologies (CNR - IFN) in Rome, Italy; while for the samples used in the rest of the experiments (samples fabricated using e-beam evaporation techniques) the RIE process was performed at the clean room of Helmholtz Nano Facility (HNF), Julich Forschungzentrum, Germany, using as a Reactive ion etcher an Oxford Plasmalab 100 Cluster Tool.

The reactive ion etching of Si_3N_4 membrane was carried on the back side of the sample using a gas mixture of CHF_3 and O_2 plasma.

The sample has been inserted in the RIE chamber with the backside upward in order to better expose the membrane to the etching process, protecting the front side for not damage or contaminate the surface of the film. Using the following recipe: 50 sccm CHF3; 10 sccm O2; RF power: 175 W; Pressure: 55 mTorr, V bias: 250V, time: 2' 50''; few try out with different samples were performed to adjust the time of the sample to the reactive action of the mixture. In the **Figure 3.7,** the difference no etched, partial etched and total etched sample can be appreciated. Even though in the figure the etched sample shown compressive stress and wrinkled surface, is worth to mention that not all the sample share this behavior. Depending in the type of evaporation process and the order in which the materials were deposited, samples can have completely flat surface after etching process as we will show in chapter 6.

Membrane without etching

Sample Etched HFN. Incomplete membrane detachment, adjusting time of etching needed. CHF3/CF4 Plasma (Reactive Ion Etching)

Sample etched, membrane completely removed

Figure 3.7 Difference between a membrane not etched, a partial etched membrane and a completely etched membrane.

3.2 Characterization Methods.

The characterization includes the structural determination of the thickness, determination of Crystal structure when applied, chemical composition and optical characterization (transmittance). Methods used to do such characterization are presented in the following sections.

3.2.1 Structural and chemical composition characterization

3.2.1.1 Atomic Force Microscopy

Atomic Force Microscopy (AFM) was used to scan the surface of the first set of samples, used in experiment 1. With the scanning the surface of the sample an image is obtained, this image is used to derive the surface morphology. This way the smoothness of the surface could be determined.

During AFM an oscillating cantilever with a very narrow tip pass at very low distance over the surface and the force between the tip and the surface deforming the cantilever is typically measured by the displacement of the reflection of a laser beam focused on the cantilever. If the tip gets closer to the sample surface, the oscillations behavior changes due to increased van-der Waals forces. Typically, a feedback loop is used to maintain free oscillations and therefore to keep the tip at a constant distance to the surface. The movement of the tip can be regulated by piezo elements [38].

The height positions of the cantilever are used to build the AFM image and hence a height profile of the surface. The average over such a height profile yields the surface roughness.

The surface roughness of the samples was measured in air by atomic force microscopy (AFM) using a Park System 70 XE-series AFM in non-contact mode *at CNR- Institute for Photonics and Nanotechnologies IFN (CNR-IFN) Padova, Italy*. The scanned area was 5x5 μm^2. The root-mean-square (RMS) and average surface roughness (Ra) were determined by using XEI data analysis software (Park Systems Corp). Measurements were taken for the substrate and for the deposited samples. The silicon nitride membranes used as substrates show always roughness values less than 1.6 nm.

3.2.1.2 Rutherford backscattering spectrometry for thickness determination.

The thickness of deposited the deposited samples using magnetron sputtering deposition techniques were determined by Rutherford backscattering spectrometry (RBS). To check the thickness and composition of the deposited films, additional 1 × 2 cm^2 flat pieces of SiO_2 (1 mm thick) have been mounted on the sample holder. A portion of the Si substrates was masked against film deposition in order to estimate the thickness of the deposited layers by measuring the step edge height with contact profiler. The deposition rate derived by profilometer measurements was subsequently checked by RBS data.

During RBS He+ ions are scattered in a material to determine its elemental composition and distribution. Incident He+ ions collide with target atoms in the sample and transfer energy to them due to Coulomb scattering. In these elastic collisions the principles of conservation of energy and impulse are valid and the energy of the scattered He+ ion EH is completely determined by the masses of the He+ MH , the mass of the target atom MT , the scattering angle θ and the energy of the incident He+ E0 [39]:

$$E_H = E_0 \left[\frac{(M_T^2 - M_H^2 sin^2\theta)^{1/2} M_H cos\theta}{M_T + M_H} \right]^2$$

The higher the mass of the target atom MT is, the higher is the measured energy of the scattered He+ ion EH for a fixed scattering angle θ and thus different atomic elements can be differentiated in the RBS spectra. If the incident He+ ion penetrates deeper into the target material it does not only loose energy due to Coulomb scattering with a certain target atom, but also smaller energy amounts due to small-angle scattering [50]. Hence, target atoms go deeper into the material resulting in the reduction on the energy in the measured spectrum than target atoms of the same element at the surface. This characteristic offers the possibility to determine the thickness of a certain layer by RBS. The measured data were analyzed deploying the software RUMP [51].

3.2.1.3 X-ray Diffraction (XRD)

Thin films deposited by sputtering are made of small grains that can be crystalline or amorphous. The size, shape and stacking of the grains are part of the film morphology. X-ray diffraction (XRD) was used to determine if the film is amorphous or polycrystalline.

If the sample is a crystal, x-rays are diffracted only in directions verifying the Bragg condition:

$$2dsin\theta = n\lambda$$

where d is the distance between crystal planes, 2θ the Bragg angle, n is an integer, and λ the wavelength of the monochromatic x-rays. The position of the peaks depends on the crystal symmetry and on the size of the elementary cell of the lattice since each crystal have a differentiate lattice, the element and its crystal structure can be determined. Crystalline phases present in a sample can be identified by comparison with x-ray diffraction curves compiled in standard databases [5,6 lucius]. In another hand, because in XRD only the scattered X-ray intensity is measured and information about the phase is totally missing, modeling is usually required to fit the measured intensity, and then by an indirect method, the structures of samples could be obtained. The problem with modeling is that fits are not unique. Analysis even gets more difficult for multilayer analysis of XRD peaks due to the unavoidable diffusions and formations of alloys, thickness fluctuations and other artifacts.

For this research work, X-ray diffraction (XRD) measurements were accomplished by using a high-resolution Bruker D8 diffractometer, Cu_K_alpha = 0.15406 nm, employing a scintillator detector with a mechanical slit of 3 mm. The equipment is located in Peter Gruenberg Institute-9 facilities at the Forschungszentrum Jülich. The scans were carried out in a range from 2Theta = 3° – 140° with angular resolutions of 0.1°. Each data point was measured for 10s.

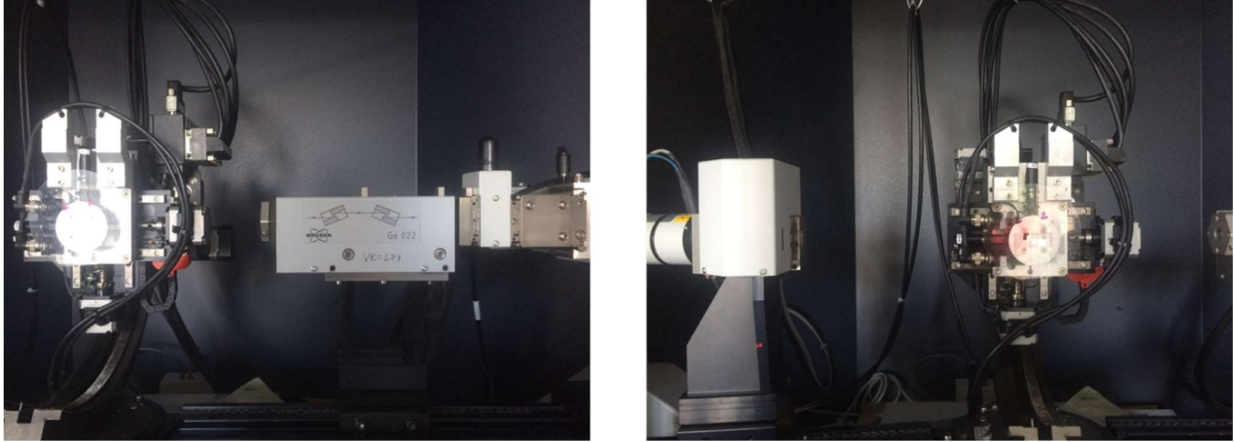

Figure 3.7 XRD instrument used for measurements, located at PGI 9 Institute, Julich Forschungzentrum, Germany.

3.2.1.4. Scanning Electron Microscopy (SEM)

Scanning electron microscopy (SEM) was also applied to investigate the properties of the free-standing sample. The measurements were performed at the imaging facilities of HFN Jülich, using a FE-SEM ZEISS SIGMA 300 (field emission scanning electron microscope), at the accelerating voltage of 20 kV.

3.2.1.4 TEM, HRTEM, STEM and EDX

Transmission electron microscopy (TEM) is an imaging technique that uses electrons passing through a thin (preferably less than 100 nm) specimen. It provides information on the atomic arrangement of atoms due to its high spatial resolution (down to few angstroms for standard microscopes). Therefore, crystal structure of crystalline materials may be accessed directly from atomically resolved TEM images. Due to the small de Broglie wavelength of electrons, resolutions below 0.5 Å can be achieved [63]. At lower magnifications, TEM image contrast is caused by differences in composition, density or thickness of the material. Therefore, macroscopic strain effect can be observed. At higher magnifications, fine details as small as single columns of atoms can be resolved. TEM is usually coupled with EDX spectroscopes in order to provide elemental analysis of specimens with much higher resolution than EDX in SEM.

Before imaging the sample for TEM, the specimens must be prepared using the focused-ion beam (FIB) method: a small area of the sample is coated with Pt and a beam of Ga ions cuts a thin sample section,

called "lamella" [65]. After separation from the initial sample, the obtained specimen can be further thinned and studied with TEM. In this way, thickness of a film can be determined.

Figure 3.8 TEM TECNAI Instrument , ER-C 1 institute at Julich Forschungszentrum

When an image is formed in TEM, can do it by using the central spot or some or all of the scattered electrons. The way that the user chooses which electrons form the image, is implemented by insertion of an aperture into the back focal plane of the objective lens, to block out selectively part of the diffracted electrons. This is, by means of special mechanism inside the TEM, the user can drive the desired aperture so that either the direct electrons or some scattered electrons. If the direct beam is selected, the resulting image is called a bright-field (BF) image; and if the scattered electrons of any form is selected, it is called a dark-field (DF) image. The difference between these two modes is that the image contrast is inverted in relation to one another. This is due to the mechanism of image formation in each case. Since BF images are formed by weakening of direct beam upon interaction with the sample, a mass-thickness contrast is in effect. The areas in the sample that contain heavier elements, appear darker. Whereas for an DF image, the diffracted beams are the main contributor to the image formation; thus, DF images contain information about the crystal lattice such as imperfections and a more reliable composition contrast comparing to the BF image. When the contrast is formed by the differences in the phase of the electron wave and thus is

called the phase contrast. This happens when a large objective aperture is selected allowing wider range of electrons with different phases to go through and form a high-resolution image (HRTEM). A typical HRTEM micrograph contains information about the orientation of atoms and spacing between them through the lattice fringes. In addition, a Fast Fourier Transform (FFT) can be applied to a selected portions of an HRTEM image to generate a diffraction-type pattern and be able to determine the crystalline structure of the deposited film.

STEM is similar to TEM. While in TEM parallel electron beams are focused perpendicular to the sample plane, in STEM the beam is focused at a large angle and is converged into a focal point. The transmitted signal is collected as a function of the beam location as it is raftered across the sample. [REF STEM]

There are multiple detectors for STEM imaging:

1. BF (bright-field) detector: small angles (<0-10 mrad). These images are like the bright-field images obtained using TEM.
2. ADF (annular dark-field) detector: larger angles (10-50 mrad)
3. HAADF (high-angle annular dark-field) detector: Angles > 50mrad

The TEM images in this work were accomplished in cooperation with the Ernst-Ruska- Center at the Forschungszentrum Jülich GmbH using a FEI´s Tecnai G2 F20 instrument.

3.2.1.5 X-ray photoelectron spectroscopy (XPS)

Photoelectron Spectroscopy is based on the measurement of the energy of electrons emitted from a surface bombarded by a beam of x-rays [8lucio]. Each atom has its own signature. One of the most important capabilities of XPS is its ability to measure shifts in the binding energy of core electrons resulting from a change in the chemical environment of the emitting atom. In this way the degree(s) of oxidation of each atomic species can be measured. The depth penetration of this chemical analysis is only a few nanometers (typically 25 Å in depth to a maximum of 80 Å), thus surface contamination and surface oxidation have a great influence on the results and samples must be carefully prepared to obtain valuable information.

XPS measurements were performed on the sample by using the Phi5000 VersaProbe II, ULVAC-Phi Inc., USA. The instrument is operated at Al K-alpha, with a monochromatic source of 1.486 keV. The measurements were carried on three 200µm size spots, with 187.5 eV pass energy, 0.8 eV step, and 100ms/step. The results are presented with quantification in atomic percentage (at%) and 15% relative error, normalized to 100 at%, with a Shirley background and empirical relative sensitivity factors. The instrument is located at the Central Institute for Engineering, Electronics and Analytics (ZEA-3) at Forschungszentrum Jülich.

3.2.2 Optical Characterization

3.2.2.1a Transmittance measurements using a gas puff target source.

The source is based on the double-stream gas puff target approach [1]. The targets are formed by pulsed injection of high-Z gas (xenon, krypton, argon) into a hollow stream of low-Z gas (helium, hydrogen) using the valve system composed of two electromagnetic valves mounted in a common body and equipped with the double-nozzle setup. The outer stream of gas confines the inner stream improving the gas puff target characteristics (higher density of high-Z gas at longer distance from the nozzle output). Strong EUV production from the double-stream xenon/helium gas puff target irradiated with nanosecond laser pulses from a Nd:YAG laser, exceeding production from solid targets irradiated in the same conditions, has been demonstrated [2].

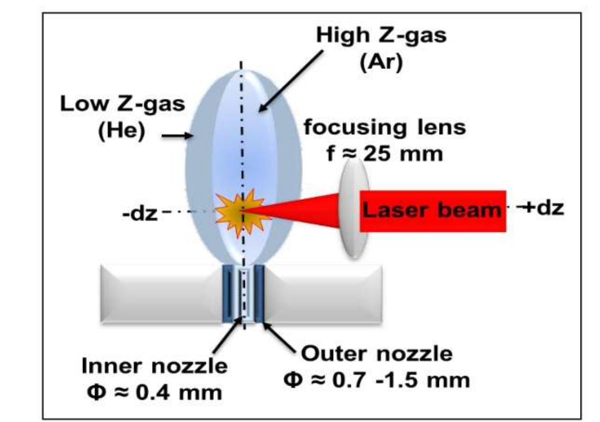

Figure 3.9. Schematic diagram of the production of EUV plasma based in a Gas puff Target set up.

3.2.2.1b Puff target source set-up

Transmittance measurements of the filters were carried on at the Institute of Optoelectronics, Military University of Technology; Warsaw, Poland. The experimental setup consists of a laser plasma EUV light source based on a double-stream Xe/He gas-puff target combined with a transmission grating spectrograph coupled to a CCD camera.

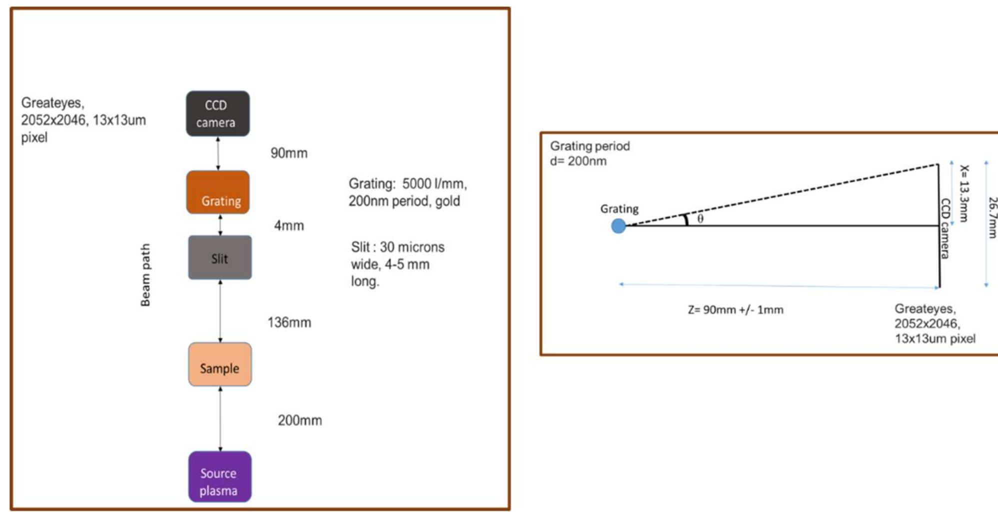

Figure 3.10 Schematic diagram of the set up for doing transmittance measurements using a gas puff target source.

The experimental setup has three major components: a laser system, an interaction chamber with the electromagnetic valve to form a gas puff target, and soft X-ray measurement instruments. The laser system consists of a commercial Nd: YAG laser _Continuum YG 682. Originally producing 10 ns FWHM pulses with energy up to 0.430 J. The soft X-ray emission spectra from laser-produced gas puff plasmas in the 1– 22 nm wavelength range have been measured with the use of two grazing incidence spectrometers _GIS equipped with variably spaced gratings, and a transmission grating spectrometer _TGS. The GIS consisted of a grazing incidence gold-coated spherical mirror and a varied spacing spherical grating of 1200 lines rmm to measure the spectra in the 5–22 nm wavelength range. The transmission grating was placed at 460 mm from the plasma. All the spectra were recorded with a back-illuminated CCD camera Greateyes GE 2048 2948 BI placed at 90mm from the Transmission grating. Measurements were taken using the following parameters: 40 shots. 10 sec - 5 Hz. The vacuum chamber was equipped with a rotary holder with eight apertures, capable to measure 7 samples without the necessity of braking the vacuum. The last aperture is reserved to measure the direct light.

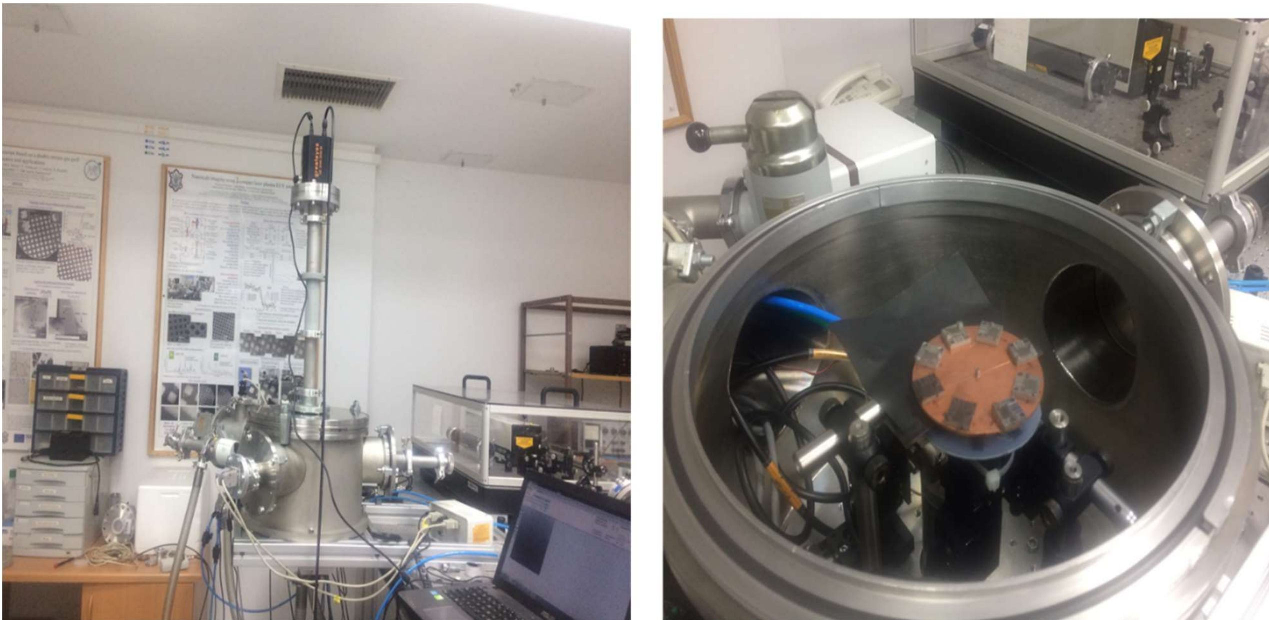

Figure 3.11. Pictures of the set up for transmittance measurements located at the Institute of Optoelectronics, Military University of Technology; Warsaw, Poland. Left image correspond to the complete set up. Right image correspond to the vacuum chamber. Rotary holder with sample can be appreciated.

3.2.2.2 Transmittance measurements at synchrotron facilities.

The transmittance measurements of the filters also were carried out in two synchrotron facilities:

- *BEAR beamline of ELETTRA – Synchrotron, Trieste, Italy*
- *Optics Beamline at BESSY Synchrotron, Berlin, Germany.* **[26]**

3.2.2.2a Experimental setup at BEAR

BEAR is a bending magnet beamline dedicated, among others, to reflectance and transmittance measurements **[31-32].** It covers an energy band from visible light to 1.6 keV, delivering radiation with well-defined spectral purity properties. The sample chamber is equipped with motors enabling movements of the sample holder in all directions (six degrees of freedom), accurate alignment, and scans in a vast angular range. Finally, a sample insertion chamber with locking transfer system allows to change and insert samples without venting. Figure 3.12 shows a schematic of the beamline.

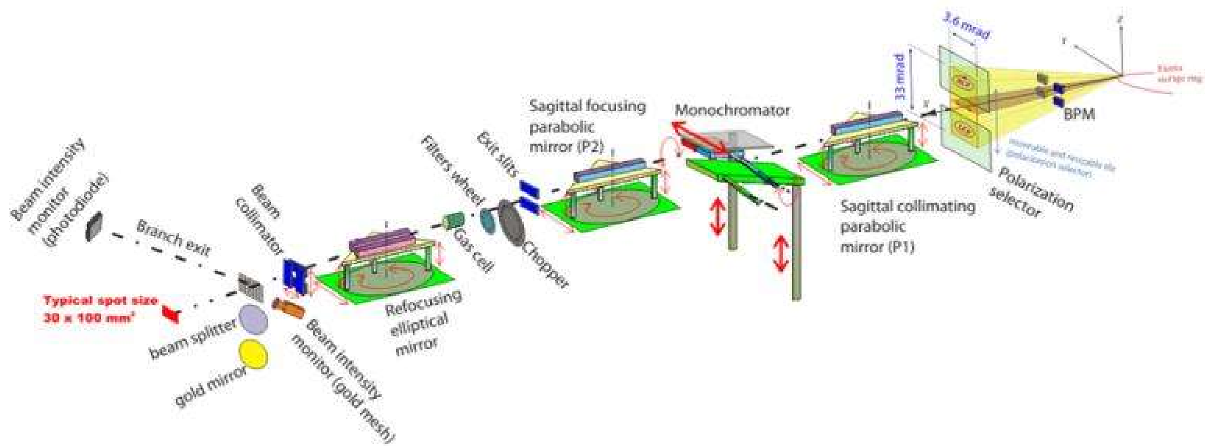

Figure 3.12 http://www.elettra.trieste.it/lightsources/elettra/elettra-beamlines/bear/beamline-description.html

3.2.2.2b Experimental set-up at BESSY II

The Optics beamline at BESSY II, is a soft x-ray bending magnet beamline equipped with plane grating monochromator, operated in collimated light. It is optimized to offer a good resolution at very high spectral purity and efficient stray light reduction by a 4-mirror high order suppressor (HIOS) and a filter and slit units (FSU). A permanent end-station, located in a clean-room hutch, possesses inside a versatile reflectometer for at-wavelength metrology, covering the spectral range from 10-2000 eV **[30].** Images of the set-up are shown in Figure 3.13

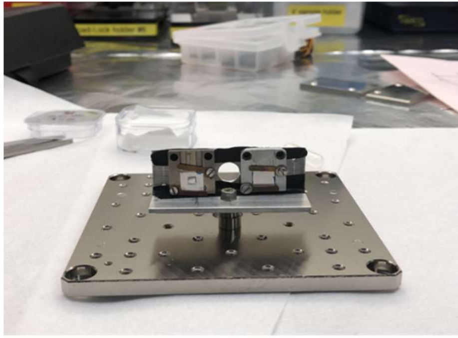

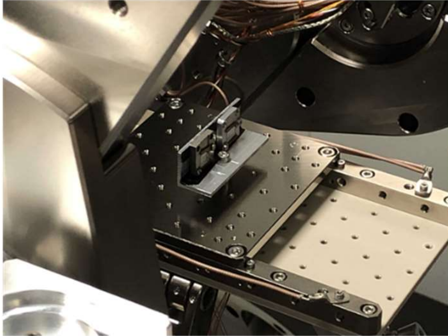

Figure 3.13 Optics beamline at Bessy II synchrotron. In the left pics, the positioning of the samples can be appreciated, the holder used have 3 holes, one for measuring the direct light and the other 2 for samples.

4 Mechanical and optical characterization of Nb/Si3N4, Zr/Si3N4, Zr/Nb/Si3N4 and Nb/Zr/Si3N4 filters (Experiment 1).

4.1 Introduction

In this part of our research, we investigated the optical and structural properties of Nb/Zr and Zr/Nb bilayer thin films for the development of free-standing transmittance filters in the EUV region between 5-20 nm wavelengths. Samples were deposited on Si_3N_4 membranes by magnetron sputtering technique, using metallic targets of niobium and zirconium. For a better understanding of the performance of these structures and their optical and mechanical properties, a single layer of Zr and Nb on Si_3N_4 membranes have also been deposited and studied. Thickness of the samples were measured by RBS stoichiometry.

From a multiple set of samples that were deposited using magnetron sputtering technique 7 of this sample were selected to resume our findings. The transmittance of 6 of the samples were characterized without etching the membrane. After first round of transmittance characterization, we proceed to complete the fabrication process follow by RIE procedure.

Fragile samples did not survive the etching process, but we achieved with success to etch the membrane from Nb/Zr and Nb samples. These samples showed higher mechanical stability and toughness.

By etching the silicon nitride membrane, Nb and Nb/Zr self-standing filters were successfully obtained, with free-standing areas up to 3×3 mm^2 and 100 nm thickness. Transmittance of the Nb/Zr free standing filter was measured. The results show the higher peak transmittance of 60% at 7.02nm and very good performance in the target range. XPS , XRD and SEM images were also used to characterize sample structure and chemical composition.

Transmittance performance of the samples has been measured by using EUV radiation at BEAR beamline at ELETTRA and Optics beamline at Bessy II synchrotrons.

The description of the samples used for this part are described in the table 4.1. Optical microscope images show that Zr and Zr/Nb structures on membranes reveal compressive stress while Nb and Nb/Zr structures present tensile stress behavior.

Table 4.1 Description of the samples used for the resume of the results of the research and measurements performed on them.

Samples	Substrate (100nm)	Nominal thickness es of individual layers (nm)	Total thickness of metal layer (nm)	Measurements performed					
				RBS	AFM Roughness	Transmittance		XRD	XPS
						At BESSY II 3 months after deposition	BEAR 1 year after deposition		
Nb	Si_3N_4	100	104	*	*		*		
Zr_1	Si_3N_4	100	108	*	*				
Zr_2	Si_3N_4	150	169	*			*		
Zr/Nb	Si_3N_4	50/50	103	*	*		*		
Nb/Zr_1	Si_3N_4	50/50	107	*	*	*			
Nb/Zr_2	Si_3N_4	50/50	107	*			*		
Nb/Zr_3	Etched (no - substrate)	50/50	107	*			*	*	*

4.2 Results and discussion

After deposition, the samples were characterized by RBS in order to detect contaminants due to the fabrication process and raw materials impurities. The specimens mostly show oxygen contamination. The oxygen concentration is not uniform with depth: in some samples oxygen probably diffused from the outside due to the air exposure, in other cases a relatively large presence of oxygen at the interface substrate/film could suggest a gettering effect at the start of the deposition.

Table 4.2 reports a summary of the RBS results: for each sample, the mean stoichiometry of the different layers was calculated. Since the density of the different detected compounds is unknown, the reported layer thickness was retrieved by assuming a hypothetical pure metal layer, the bulk metal density and the detected amount of metal. Samples Nb/Zr_1, Nb/Zr_2 and Nb/Zr_3 were deposited together, then we are assuming the three samples have the same chemical composition. The oxygen contamination mainly affects the Zr_1, Zr_2 and Zr/Nb films.

Both Zr and Nb oxidize readily when they are exposed to air. Zr oxidize at faster rate than Nb as it is shown in table 2. From literature we know that the most common oxidation state of Zr, in thin metallic films, is ZrO_2, while for Nb is Nb_2O_5. The material's density changes with oxidation, producing the expansion of the layers thicknesses, resulting in the appearance of some intrinsic stress in the film. The lower rate of oxidation and possible plastic deformation of Nb layers could allow the relieve of the residual stress. **[27,33,34,35]**

Table 4.2 Mean stoichiometry of the different deposited layers calculated from RBS data. Thickness* is related to a hypothetical pure metal layer containing the detected amount of metal and having bulk density.

Sample	**Nominal total thickness (nm)**	**Top layer (mean composition − thickness*)**	**Bottom layer (mean composition − thickness*)**
Nb	100	$NbO_{0.3}$ − 104 nm	−
Zr _1	100	$ZrO_{1.1}Hf_{0.01}$ – 108 nm	–
Zr_2	150	$ZrO_{0.1}Hf_{0.01}$ − 169 nm	--
Zr/Nb	100	$ZrOHf_{0.01}$ – 49 nm	$NbO_{0.2}$ − 54 nm
Nb/Zr (1,2,3)	100	$NbO_{0.1}$ − 50 nm	$ZrO_{0.4}Hf_{0.01}$ – 57 nm

Also, the strain strongly depends on the selected top layer. *Figure 4.1* depicts examples of filters grown with compressive and tensile strain. The top images of figure 4 refer to Nb and Nb/Zr_1 samples, with Nb on the top. In this case, a smooth homogenous structure with tensile stress is observed. The bottom images show Zr_1 and Zr/Nb specimens: the surface is wrinkled by compressive stress.

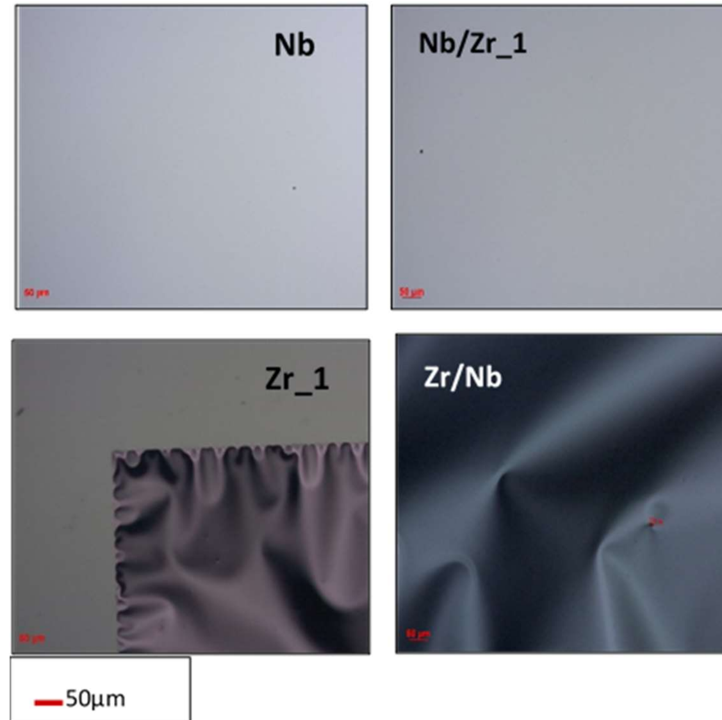

Figure 4.18 Optical images of the surfaces on the different material samples on Si_3N_4. Nb and Nb/Zr, flat samples, grown with tensile stress, (top images). Zr and Zr/Nb, wrinkled samples, grown with compressive stress, (bottom Images).

Regarding the nanoscale observation, the surface roughness of the Nb and Nb/Zr samples is almost the same as that of the substrate, while in case of Zr and Zr/Nb structures the surface experiences an increase of roughness, particularly in the Zr specimen. The results of the morphology analysis performed by AFM are summarized in table 4.3:

Table 4.3 Summary of surface roughness values measured by AFM

Sample	Nominal thickness (nm)	Roughness (nm)
Si_3N_4(substrate)	100	1.4±0.2
Zr_	100	3.4±0.2
Nb	100	1.4±0.1
Zr/Nb	100	1.8±0.2
Nb/Zr_	100	1.4±0.1

The roughness and the stress of the films can affect the properties of the wavefront passing the filter, by inducing distortion of the incoming beam, also can affect the quality of the films and the mechanical stability of the filters. Furthermore, Zr and Zr/Nb samples exhibiting high surface roughness and compressive stress are not the best candidates for etching process. In fact, we know that they didn't survive the etching.

The filters with the tensile strain (Nb and Nb/Zr_1), on the contrary, demonstrate a flat surface, suitable for achieving a successful etching process and for the filters manufacturing. The reduction of the compressive stress is due to the presence of Nb as top layer. The stress in Zr thin films could be related to the pronounced oxidation of Zr during deposition and the continuing escalated oxidization due to exposure with the air, after deposition. **[33-34]**

Figure. 5 shows the optical microscope images of the Nb/Zr filter surface structure before and after the etching procedure. Due to the detachment of the silicon nitrate membrane, we can observe how the membrane releasing changes the stress on the surface of the sample.

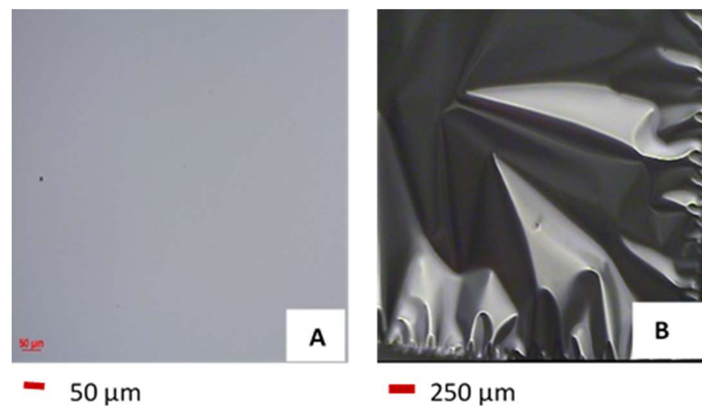

Figure 4.5 Optical microscope images of the Nb/Zr sample before etching procedure (left) and after etching procedure (right).

Transmission measurements were performed before the etching for the samples of interest in the EUV region 40-410 eV (3-31 nm) with steps of 0.2 eV.

In *fig 4.6* we present the results of transmittance measurements for Nb/Zr_1 (BESSY II) and Nb/Zr_2 (BEAR) samples. As mentioned before, they were deposited together in the same chamber; sample Nb/Zr_1 was measured 3 months after deposition while sample Nb/Zr_2 was measured 1 year after

deposition in order to evaluate possible effects of aging and contamination on the transmittance performance of the filters.

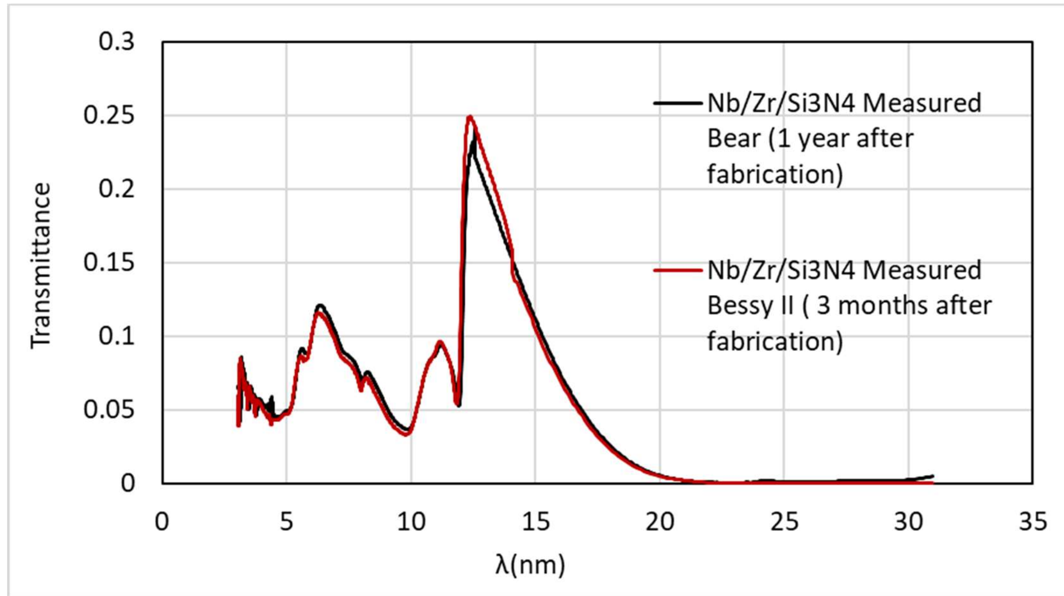

Figure 4.6 Measured transmittance comparison between sample Nb/Zr_1 and Nb/Zr_2. Samples were fabricated together, in the same chamber; they have the same thicknesses. Transmittance of Nb/Zr_1 was measured 3 months after and Nb/Zr_2 was measured 1 year after fabrication.

There is a minimal difference in the transmittance spectra of the two samples between 3-31nm. Since the samples characterized are not exactly the same, we cannot directly conclude that the slight reduction of performance is due to the aging. However, taking in account that the samples were fabricated during the same deposition run and were kept in similar packing conditions, the results are a good indication of the chemical stability and wear resistance of Nb/Zr bilayer.

After one year, also the samples Zr_1, Nb, and Zr/Nb were characterized in terms of transmittance at BEAR beamline. The total thickness of the metal layers for all the samples is around 100 nm plus 100 nm of the Si_3N_4 membrane. The idea was to compare structural and optical performance of them. The 100 nm Zr sample appears more fragile than Nb one and bilayers. This is possibly due to the higher compressive stress that showed after deposition. During handling and measurement, the 100 nm Zr sample got broken. Then, we decided to use a thicker sample of around 169 nm of Zr (Zr_2) to study the properties of single Zr layer.

Figure 4.7 shows the experimental transmittance of the measured samples together with the transmittance curves obtained by IMD simulation; using theoretical optical constants of the targeted materials assuming the RBS thickness results and no contamination. All the samples exhibit lower transmittance compared to the calculated data (the Si_3N_4 membrane was considered in the simulated curves). Besides the optical constants used for the simulation (LLNL_CXRO from IMD database), the discrepancy of transmission could have two possible causes:

1. different level of oxidation in the surface and through the sample than RBS results showed;
2. different kind of contamination on the surface and oxidation of the sample.

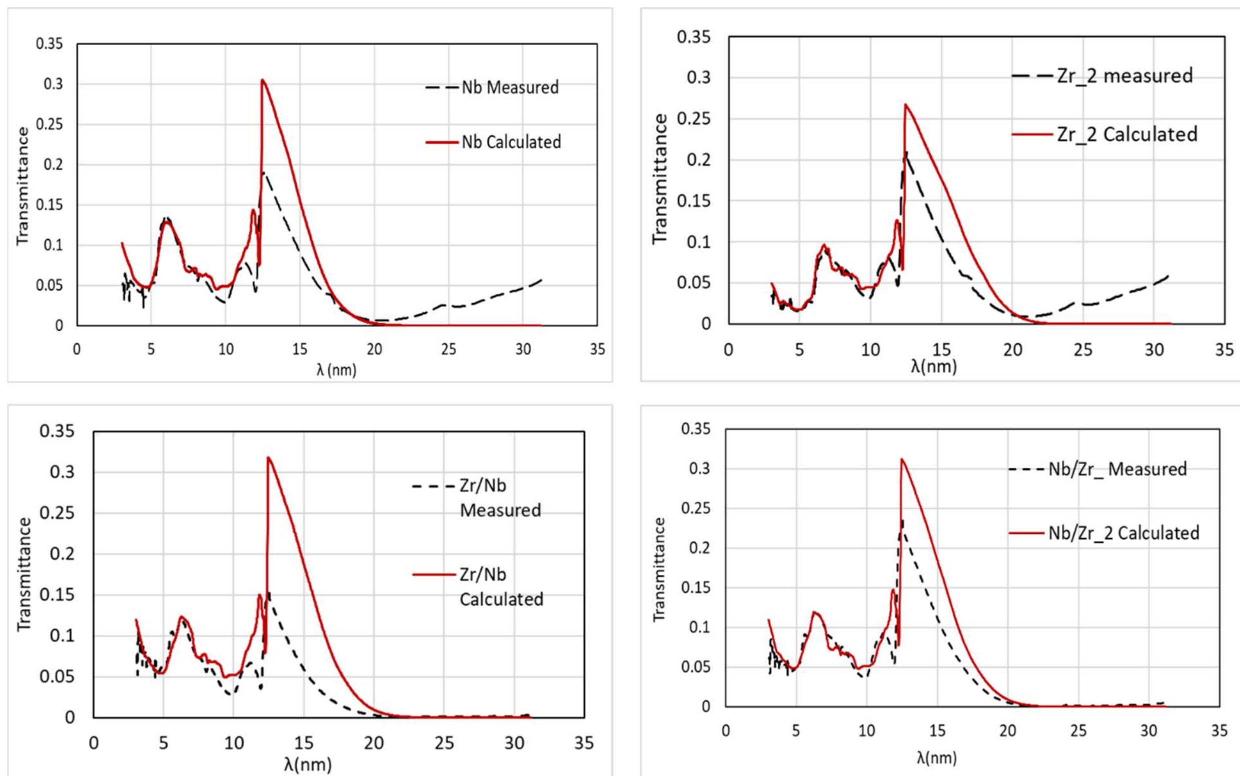

Figure 4.7. Transmittance curves of the samples deposited on Si_3N_4 membrane substrates, (not etched samples). The graphs show the comparison between the calculated and the measured values of transmittances for the different samples.

Figure 4.8 shows the comparison between four of the measured samples and the theoretical transmittance of the silicon nitride membrane. As we can observe, Nb/Zr_2 exhibits the higher peak transmission, approximately 24% around 12.55 nm. Zr/Nb sample, on the contrary, shows lower transmittance

performance. The 100 nm Zr specimen theoretically should have better transmittance performance, but it didn't survive the measurement campaign and we don't have any experimental results for it. Some studies have linked the compressive stress in sputtered zirconium thin films to the low pressure during the deposition, and to the transition from metallic to oxidized film **[33-34]**. As it was shown before, in *Table 4.2*, higher concentration of oxygen was present in Zr/Nb specimens. This could mean an increase of oxidation of the sample, which explains the lower transmittance response.

For the same thickness, the stiffness of the Nb guarantees stable structures on membrane **[17]**, but with lower transmittance performance than Zr. In fact, the transmission of the Nb is slightly below of the widely used zirconium filters and below of the Nb/Zr free standing filter, proposed in this manuscript (see *fig 7*). The bilayer structure of Nb/Zr combines the higher mechanical stability of Nb with the higher transmittance performance of Zr in this specific spectral region, resulting in the best candidate for free-standing filters.

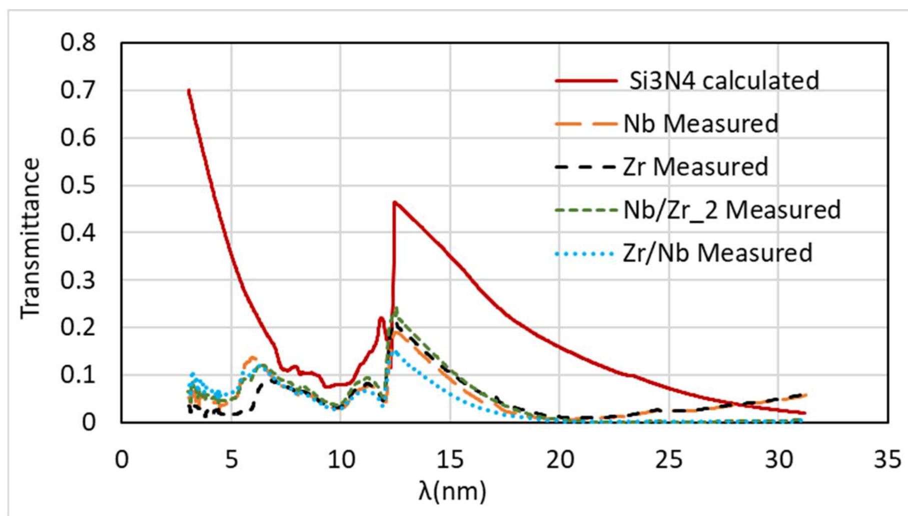

Figure 4.89 Comparison of the transmittance values of all the samples and the calculated values of transmittance for the Si3N4 membrane substrate.

The etching process was tried out on the four different types of samples, and as it was mentioned before, only Nb and Nb/Zr samples survived the etching process proving to have high mechanical stability.

In this section we mainly focus on the new free-standing Nb/Zr filter which, based on simulated data, could offer higher transmittance performance than monolayer Nb of the same thickness. Sample Nb/Zr_3

(see table 1) corresponds to the Nb/Zr free standing filter (etched sample). We did not test Nb free-standing filter.

We performed XRD measurements of this sample. Besides the Si substrate peaks, signatures of the Nb/Zr epilayers were found. These peaks are attributed to the Zr in the hcp crystal structure at 32.2° and Nb in the bcc lattice configuration at 38.0°, as it is shown in *fig 4.9*.

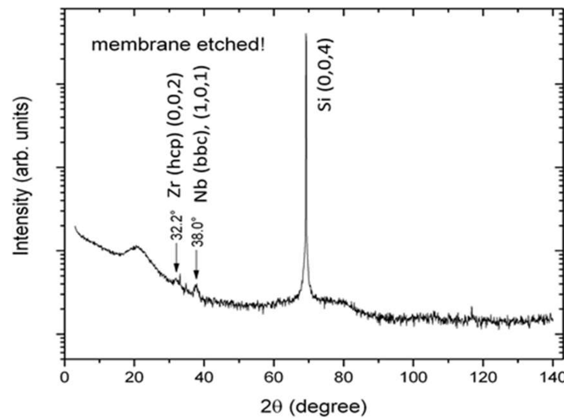

Figure 4. 10 XRD measurements. Signatures of Niobium and Zirconium were found, and also the signature of Silicon due to the frame of the samples.

Due to the polycrystalline nature of the sample's structures, the picks are not strongly sharp, however well identifiable SEM images depict the surface of the Nb/Zr_3 (*Figure. 4.10*). In the left image, filter window area and silicon frame can be distinguished; in the right, the polycrystalline structure is observed.

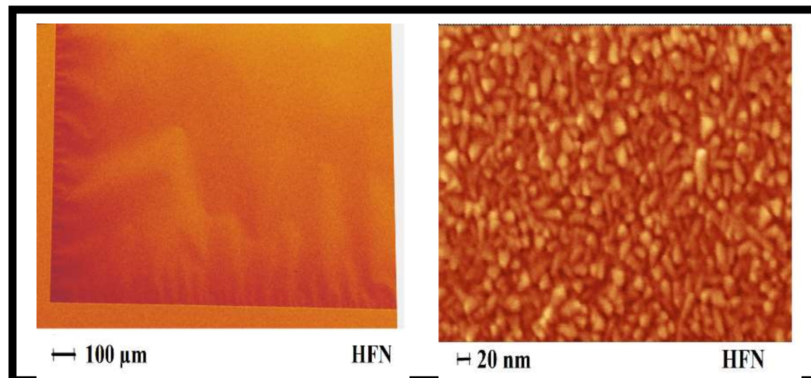

Figure 4.10 SEM images of Nb/Zr_3 (free self-standing filter) around 100 nm thickness. In the left image, it could be appreciated how the tensile stress was released. In the right, image of the surface nanostructure is shown.

The transmittance of Nb/Zr free standing filter was measured at BEAR beamline between 40-420 eV (3-31 nm).

A rough transmittance scan, using the reading on the diode signal, was performed on the sample along horizontal (Y-axis) and vertical (Z axis), using 40 eV photon energy for studying the uniformity of the filter. Results are presented in *Figure. 4.11*. The membrane window is about 3 mm x 3 mm. The signal is very stable inside the window area along both axes, demonstrating a uniform bilayer structure.

Subsequently, the transmittance was measured in the complete wavelength range. The results are in *Figure. 4.12*. The difference in transmittance before and after the etching procedure is shown in *Figure 4.12 left.* A considerable increase of transmittance is notable as it is expected after the membrane is removed. The filter possesses the higher transmittance's peak at 7.02 nm of about 60%. At 11nm the transmittance is 47.5% a little bit lower than the results presented by Brose S. et all in 2012, but higher than for filters proposed by other authors **[12, 25, 26]**. Brose measured a Nb free standing filter with 48% of transparency at 11 nm **[17].** We present broad-band characterization of the high throughput Nb/Zr free standing filter developed in this work and thought for a wide wavelength range.

Figure 4.12 right shows the comparison between theoretical transmission curves and measured one of the investigated filter. We present two theoretical curves: "Nb/Zr Calculated 1" corresponds to the IMD simulated transmission for 107 nm ideal Nb/Zr filter by ignoring any contamination or oxidation of the materials. As we can observe, the measured and Calculated 1 curve have big discrepancies, then we simulated the transmission of a more realistic structure. In "Calculated 2" curve, we considered the RBS thicknesses results, we simulated the Nb/Zr filter assuming a thin layer of Nb_2O_5, most common oxidation state for Nb thin film **[35-36]**, on top of the Nb layer and a thin layer of ZrO_2 at the interface **[27, 33, 34]**.

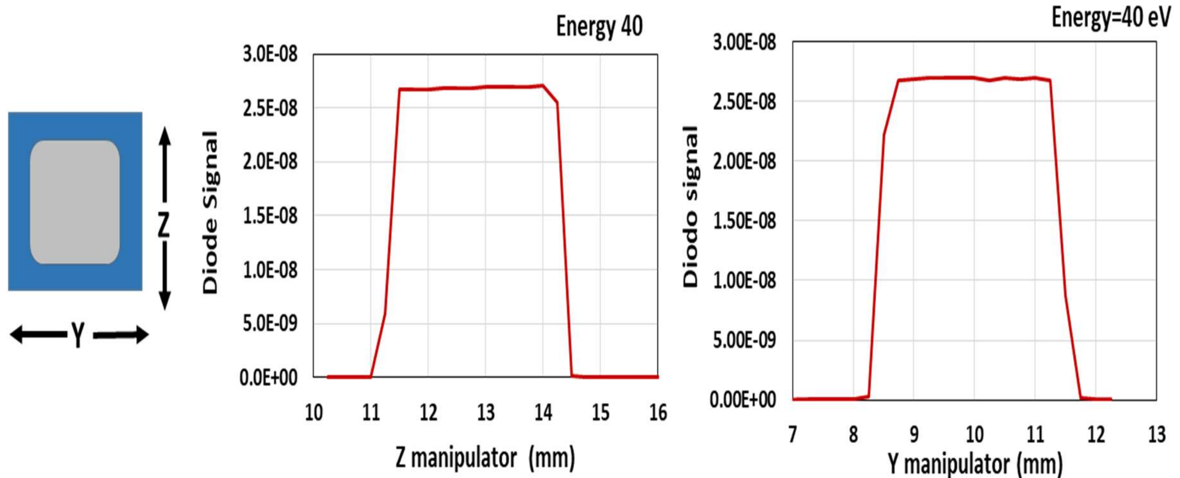

Figure 4.11 Y and Z scan of the sample using an energy of 40 eV to study uniformity of the sample. The filter window is about 3mm x 3mm, and the transmitted signal looks very stable.

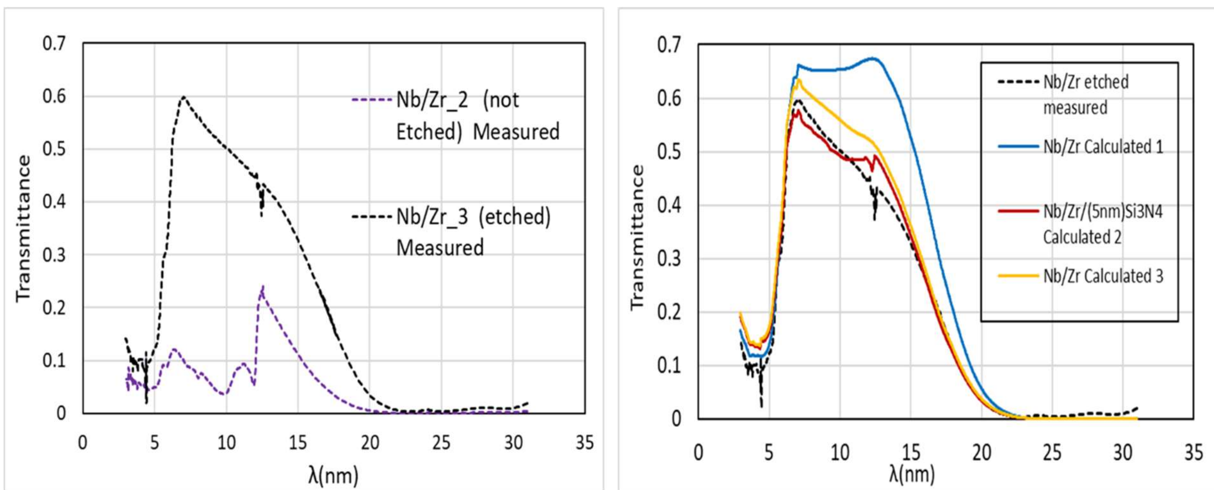

Figure 11 Left. Comparison of transmittance values of Nb/Zr (Nb/Zr_2) before and after the etching process (Nb/Zr_3). Right. Comparison of transmittance measured values of Nb/Zr free standing filter (Nb/Zr_3) in contrast with the IMD simulated transmittance considering only the nominal thickness of the sample in the Calculated 1 curve. Calculated 2 curve is simulated considering the nominal thickness, layers of oxidation of the materials, carbon contamination and 5 nm of a residual Si_3N_4 membrane. Calculated 3 curve is simulated using the same structure of Calculated 2 but assuming complete etching (no residual membrane).

Furthermore, since Carbon is as a common type of contamination on metal filters exposed to the environment, we added in the simulation 4 nm of carbon on the surface. In the model, a 5 nm thin layer of Si_3N_4 has been also added to the bottom of the structure to take into account the possible residuals of the membrane after the etching process. The final structure (*Figure. 4.13*) used for the simulation of the Calculated 2 Curve is the following, from top to bottom:

1) C layer = 4.00 nm
2) Nb2O5 layer = 7.00 nm
3) Nb layer = 42.00 nm
4) ZrO2 layer = 20.00 nm
5) Zr layer = 37.00 nm
6) Si3N4 layer = 5.00 nm
7) C layer = 5.00 nm

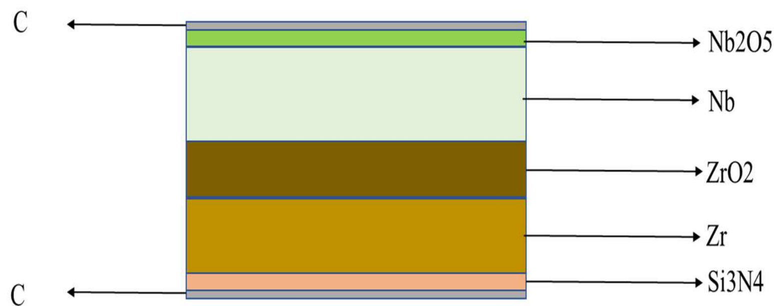

Figure 4.13 Filter Structure used for obtaining the transmittance simulated curve Calculated 2, which agreed more closely to the measured curve.

Indeed, the measured and Calculated 2 curves are very similar. We can deduce that our hypotheses of contamination have some grounds. In Calculated 3 curve, we consider the same carbon and oxygen contamination as in Calculated 2, but in this case, we are assuming a completed etching (no presence of residual membrane). The transmittance of the filter is improved in case of achieving complete etching. Furthermore, we can conclude that carbon contamination and oxidation of the metal layers are the higher contributors to the reduction of the transmittance performance of the filter. Some absorption features can be found in the measured data at 4.39 nm and 4.45nm corresponding to Carbon K absorption edge and at

12.2 nm and 12.4 nm, where the LII and LIII Silicon absorption edges are present. These lines are found not only in the experimental analysis, but also in the Calculated 2 curve.

To test the hypotheses of surface contamination other than the initial oxidation levels found in the RBS results after the fabrication of the samples, XPS mapping in three different spots of the free-standing filter was performed. *Fig 14* shows the image of the three spots randomly selected to determine the homogeneity (about 8nm deep) of the contamination at the sample surface.

Figure 4.14 XPS analysis was performed in the 3 different shown spots.

In *Figure 4.15* the XPS spectrum from one of the spots is reported and in *table 4.4* results from the survey of the three spots are displayed.

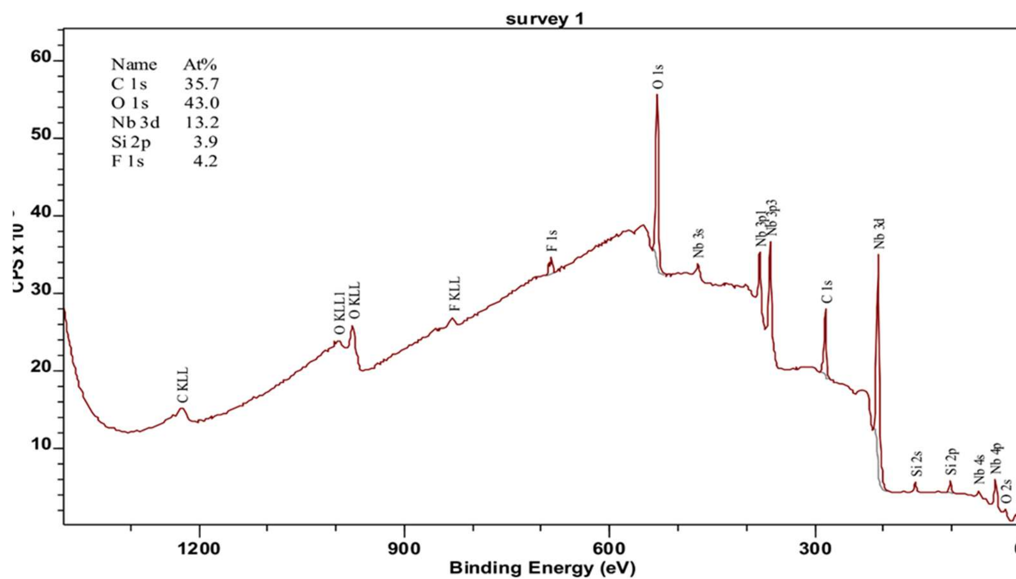

Figure 4.15 XPS spectrum of one spot measured on the Nb/Zr free standing filter.

Table 3. Quantification in at% of elements found on the surface of the free-standing filter. The analysis can reach between 5 to 8 nm deep.

Elements found	**Spot 1 (At %)**	**Spot 2 (At %)**	**Spot 3 (At%)**
C	35.7	35.0	37.0
O	43.0	42.3	41.3
Nb	13.2	13.1	12.4
Si	3.9	4.7	4.5
F	4.2	4.9	4.8

The results indicate the presence of carbon contamination on the surface on top of a natural oxide layer of Nb_xO_x. Furthermore, some Si and F traces were found on the surface. The XPS results agree with the transmittance performance of the filter as we have shown in Calculate 3 curve.

4.3 Conclusions:

Nb and Zr, have good transmittance performance between 5-20 nm, they are good candidates for EUV filters for FEL 2 at FERMI that cover specifically this range. The transmission of the Nb is slightly lower than that of widely used zirconium filters, but the higher stiffness of the Nb allows obtaining more stable filters of the same thickness. The use of the combination of these two materials, in bilayer structures, brings together the good transmittance performance of Zr and the stiffness of Nb which makes Nb/Zr an excellent choice for fabrication of thinner free standing EUV filters.

Nb/Zr free standing filters were obtained, showing a peak transmittance of 60% at 7.02 nm, this is the best reported transmittance value until now, to our knowledge, for this wavelength. In the case of the filters on Si_3N_4 membranes the maximum transmittance achieved was approximately 24% around 12.55 nm. Due to the high compressive stress of Zr and Zr/Nb on Si_3N_4 samples, etching the membrane was not possible. On the other hand, for the samples that showed flat, tensile stress surface, the etching process was successful, obtaining free self-standing Nb, Nb/Zr filters. Besides the presence of a residual thin layer of Si_3N_4 at the bottom of the sample, the XPS analysis of the Nb/Zr free standing filter indicated that the reduction of the expected values of transmittance could be due to the surface contamination and some level of oxidation of the metal layers. It is recommended to grow an oxidation protection layer in situ with the metal material deposition to avoid progressive oxidation of the filters.

5. TEM Study of the bilayer structures Zr/Nb, Nb/Zr and Nb/Zr/Nb on Si3N4 membranes

A set of 4 samples were selected for study the structural composition of the bilayer filters. Samples were deposited using e-beam deposition techniques. This 4 samples were not etched, since in any case during the preparation of the sample for TEM specimen, the filter will be "sandwiched".

We are interested in understanding the reason why Nb/Zr filters resulted, regardless of the type of the deposition technique used during the fabrication, tougher than the Zr/Nb filter. The study of the crystal structure of the sample and the interface properties using TEM analysis could give us the answer.

Samples to be analyzed are:

- 2 Nb/Zr filter 50 nm/50 nm thickness. +/- 5 nm error in each layer, all samples have 100 nm of membrane.
- 1 Zr/Nb filter 50 nm /50 nm thickness.
- 1 Nb/Zr/Nb filter 25 nm/50 nm/ 25 nm .

The 3 samples have 100 nm of membrane as substrate. HRTEM was possible to obtain for some samples and also EDX Analysis.

5.1 Nb/Zr TEM analysis

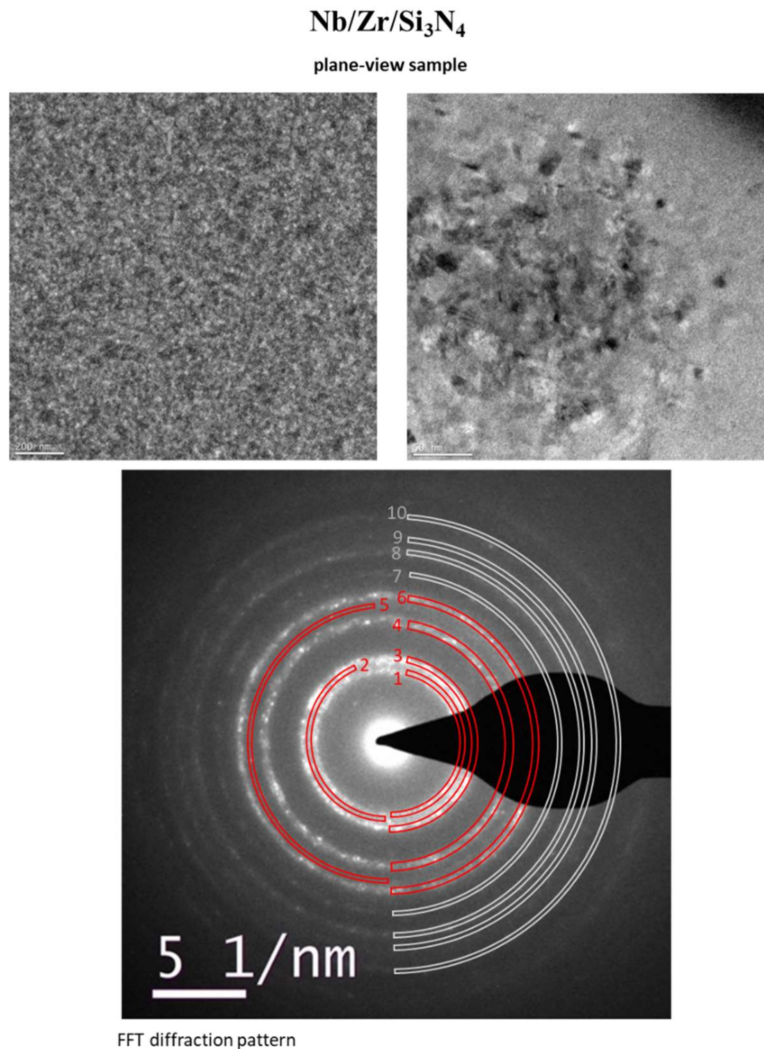

Figure 5.1 diffraction pattern of the normal surface

Accordingly**, the best fit corresponds to the Zr Fm-3m structure,** all peaks of this structure are present and the ratios from the experimental pattern agree with this structure model. It is possible also that hcp Zr is present – its strongest intensities (of 101) and (110) would overlap with the firs ring

For Nb it is not possible to exclude it, because within the calibration accuracy, possible unit cell size variations and the broadness of the experimental intensities (up to 1 mn-1) these are broad enough to contain the reflexes of Nb structure, as well. Moreover, all Nb reflexes overlap with some Zr intensities.

For Si we are assuming a structure model with Fd-3m space group (structure of mostly used Si wafers).

Si can be excluded, because its strongest peak of (111) planes is missing in the experimental pattern. Another g for Si would overlap with Zr pattern.

Table 5.1 comparison between Experimental g values and Zr and Nb g values for different crystal structures. Best fitted values are in yellow

	Experimental g nm-1	**g_Zr Fm-3m nm-1**	**hkl**	**g Nb Im-3m nm-1**	**hkl**	**g_Si Fd-3m nm-1**	**hkl**	**g_Zr P63/mmc nm-1**	hkl	**g_Zr P6/mmm nm-1**	hkl
								3,57	**100**	**3,92**	**101**
1	**3,8-4,0**	**3,82**	111			**3,19**	111	**3,88**	**002**	**3.97**	**110**
2	4,2			4,28	110			**4,06**	**101**		
3	**4,4-4,7**	**4,42**	200								
										5,1	111
						5,21	022	**5,28**	**102**	**5,5**	**201**
										6.36	002
								6,2	100		
										6.85	**211**
4	**6,6-7,0**	**6,24**	220	6,06	200	**6,11**	113	**6,8**	103	6.88	300
5	7,5	**7,32**	311	**7,42**	211	7,37	004			**7.5**	**112**
6	**7,8-8,2**	7,65	222			8,03	113			7.94	220
7	9,1-9,3	8,83	400	8,57	220	9,02	224				

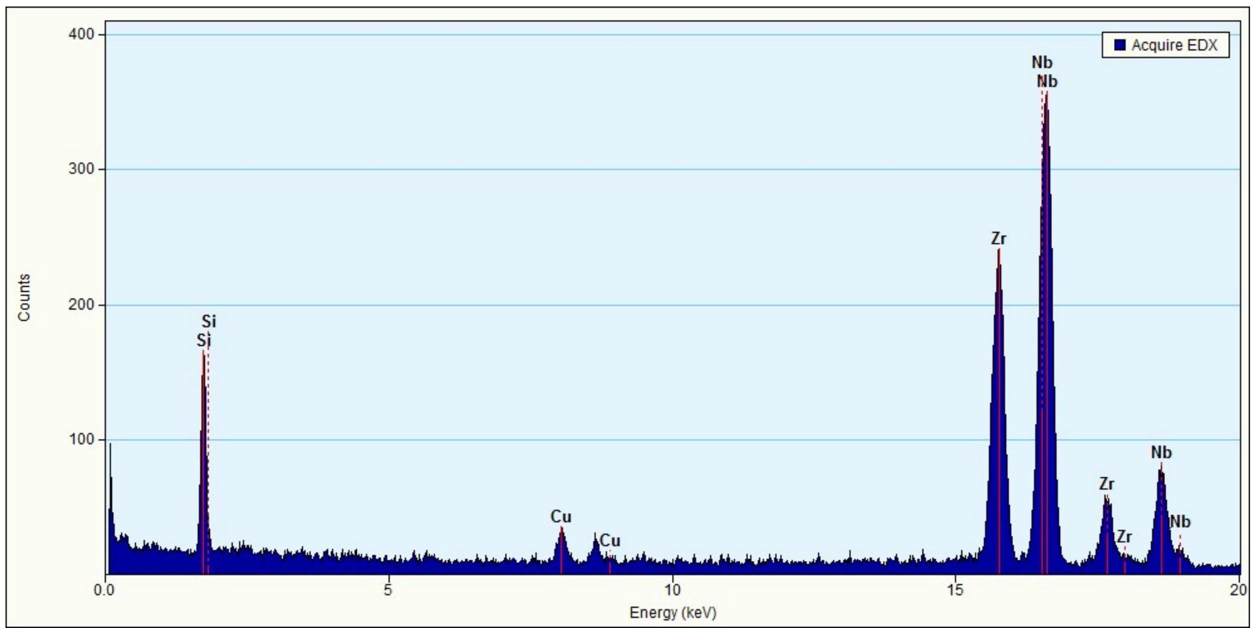

Figure 5.2 EDX analysis of the Nb/Zr Filter

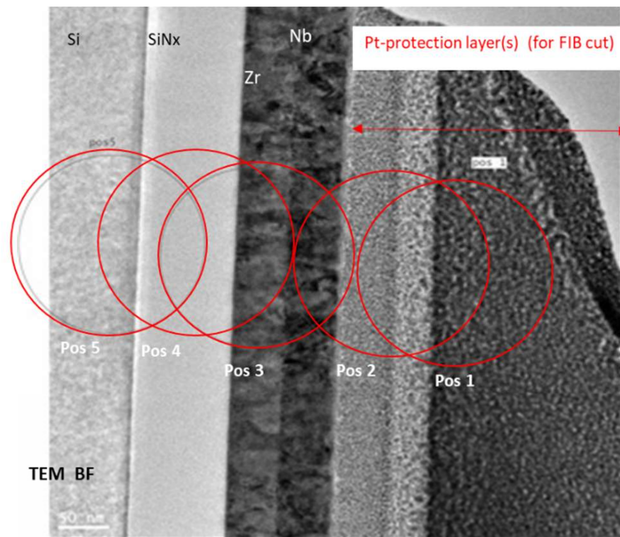

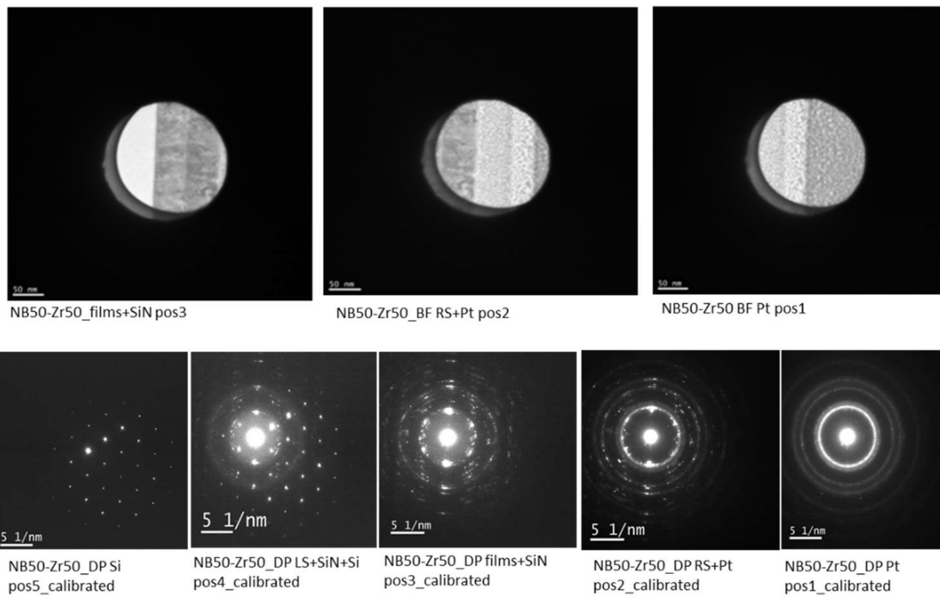

Figure 5.3 diffraction pattern of each contact interfaces.

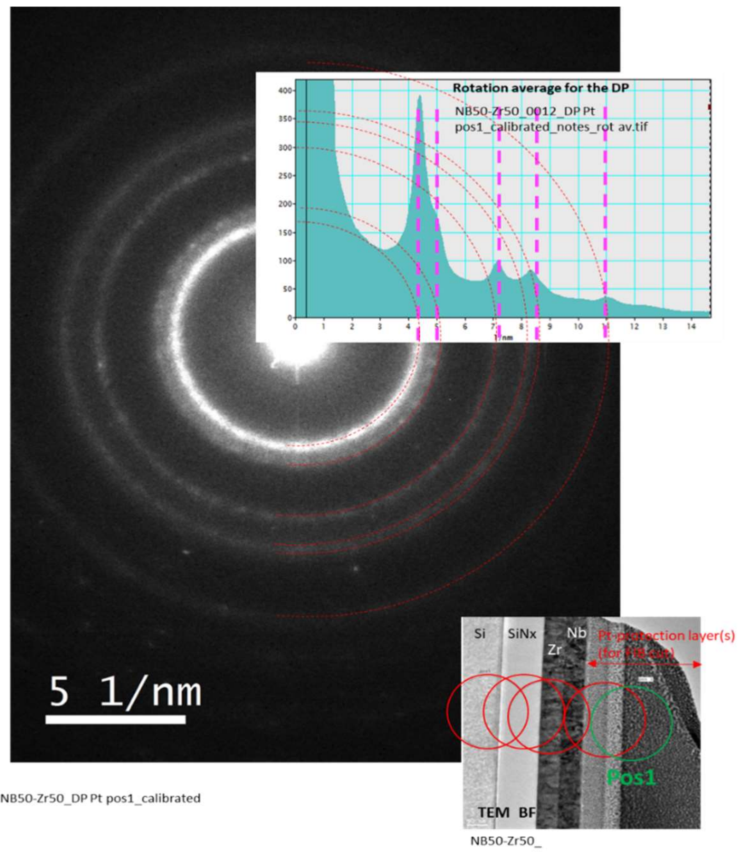

Figure 5.4 Diffraction pattern of the green circle in the image above, which represents position of the selected area aperture used for the acquisition of DP in pos 1 (i.e. Pt only)

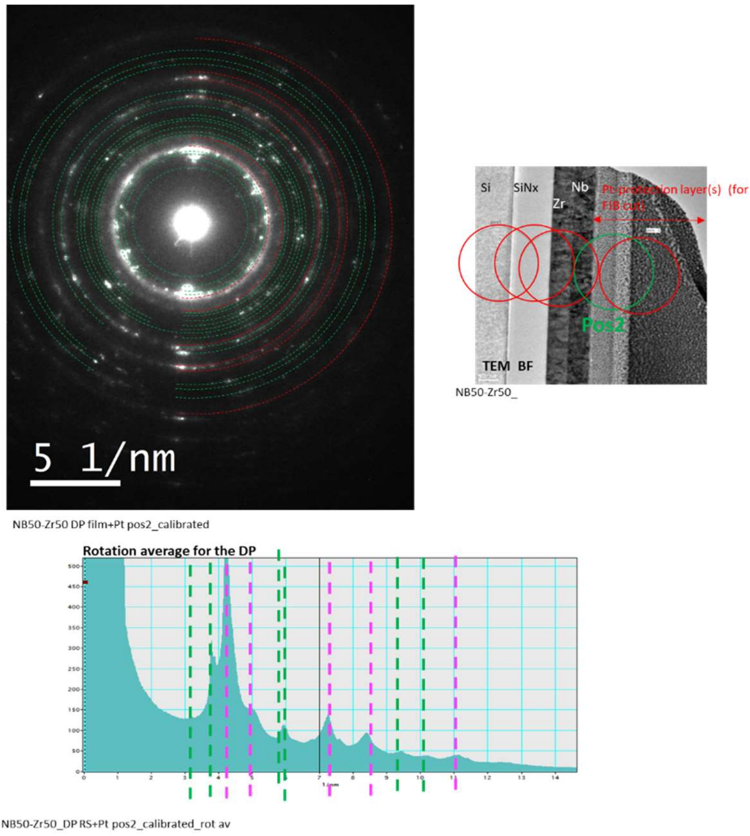

Figure 5.5 green circle in the image above represents position of the selected area aperture used for the acquisition of DP in pos2 (i.e. Pt and top layer-mainly)

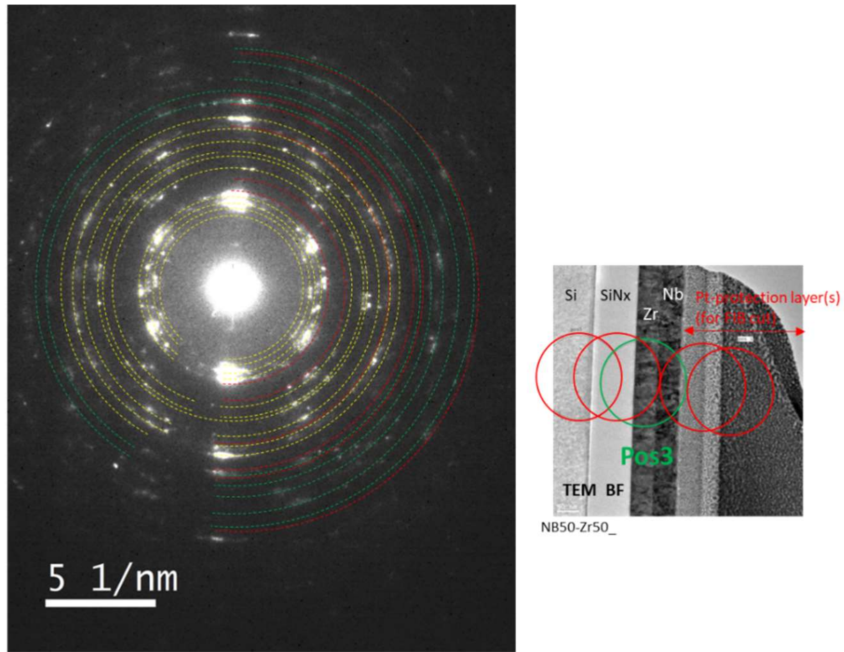

NB50-Zr50_DP films+SiN pos3_calibrated

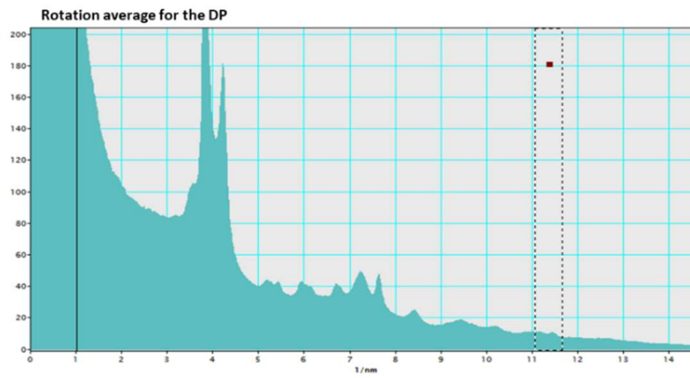

NB50-Zr50_0012_DP films+SiN pos3_calibrated_rotat av

Figure 5.6. green circle in the image above represents position of the selected area aperture used for the acquisition of DP in pos. 3 (both layers and the SiNx part)

Pos 4 Si+SiNx+Zr+ZrO

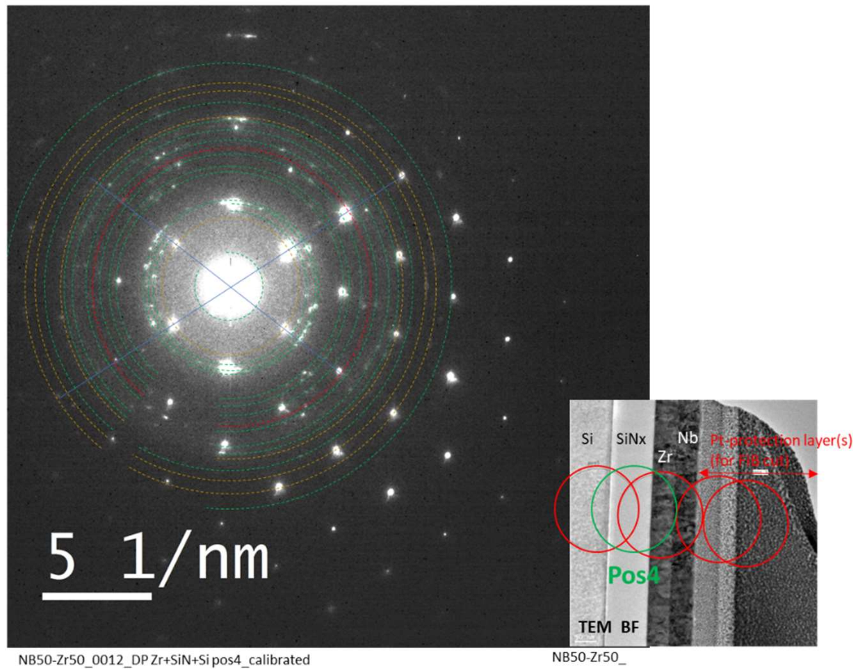

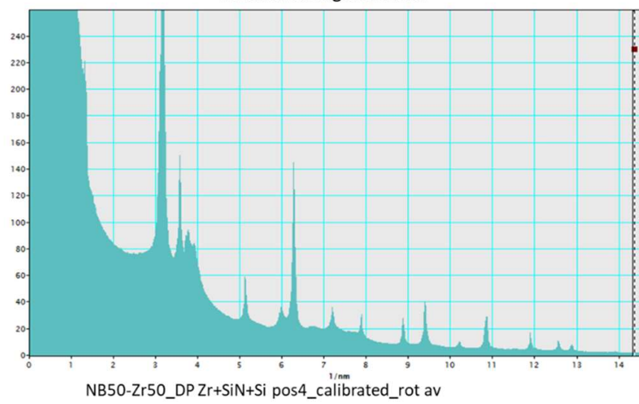

Figure 5.7. green circle in the image represents position of the selected area aperture used for the acquisition of DP in pos 4, i.e. Si+SiNx and bottom layer

Positions of intensities (in nm-1) the respective diffraction patterns

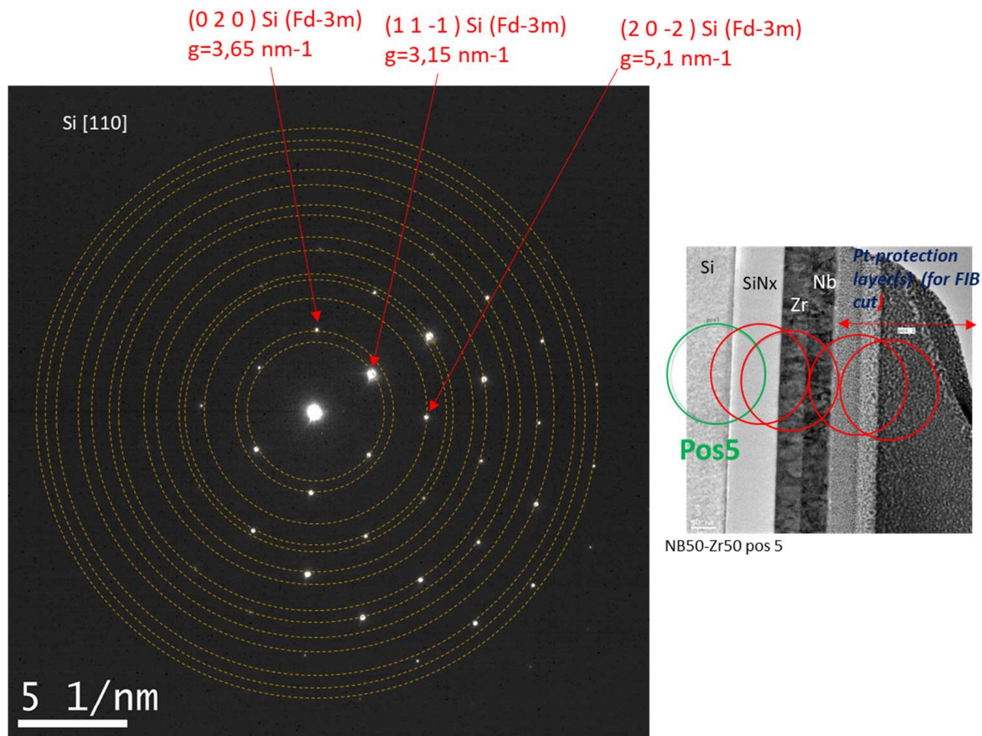

Nb50-Zr50 DP Si pos5_calibrated.

Rotation average for the DP

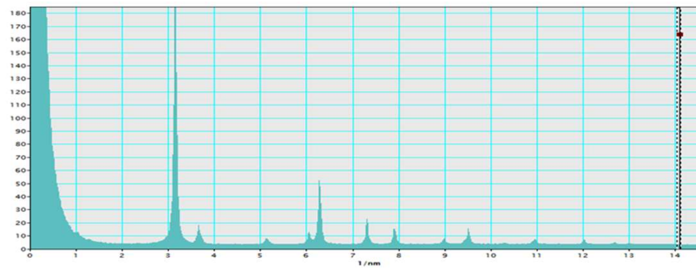

Figure 12 green circle in the image above represents position of the selected area aperture used for the acquisition of DP from pos 5 i.e. Si and SiNx only.

Table 5. 2 *Positions of intensities (in nm-1) the respective diffraction patterns for Nb/Zr*

Pos 1	Pos 2	Pos 3	Pos 4	Pos5_ Measured/model
	3.2 ZrO (111)		3.2	3.2 (3,19)
	3.7	3.5 Zr P63/mmc (100)	3.7 +Si	3.7 (3.68)
	3.8	3.8 Zr fcc (111) Zr P63/mmc (002)	3.9	
	3.9 ZrO (200)		4.1 Nb (110)	
4.4	4.2+Pt	4.2 Zr fcc (200)		
5.1	5.2+Pt	5.2 Zr P63/mmc (102)	5.2+Si	5,2 (5,21)
	5.4 ZrO (220)	5.4	5.6	
	5,7	5.9		
	6.0	6.0	6.1Nb (200) +Si	6.1 (6.11)
	6.2	6,15 Zr fcc (220) Zr P63/mmc (110)		
	6.4 ZrO (311)		6.3	6.4 (6.38)
	6.8	6.7 Zr P63/mmc (103)	6.7	
7.1	7.3+ Pt+Zr	7.2 Zr fcc (311)	7.4 Nb (211) +Si	7.4 (7,37)
	7.7	7.6 Zr fcc (222)	7.8	
			8.0	8.0 (8.03)
8.3	8.4ZrO (331) +Pt	8.4	8.6 Nb (220)	
			9.1	9.1 (9.235)
	9.4 ZrO (422)	9.4	9.6 Nb (310)	9.6 (9.57)
	9.7			
	10.2	10.2	10.4 Nb (222)	10.4 (10.42)
11.0	11.1	11.0	11.1	11.1 (11.05)

Accordingly**, the best fit corresponds to the Zr Fm-3m structure,** i.e. all peaks of this structure are present and the ratios from the experimental pattern agree with this structure model. It is possible also that hcp Zr is present – its strongest intensities (of 101) and (110) would overlap with the firs ring (I did not type other intensities of hcp Zr since they are weak.

For Nb it is not possible to exclude it, because within the calibration accuracy, possible unit cell size variations and the broadness of the experimental intensities (up to 1 mn-1) these are broad enough to contain the reflexes of Nb structure, as well. Moreover, all Nb reflexes overlap with some Zr intensities.

For Si I assumed a structure model with Fd-3m space group (structure of mostly used Si wafers).

Si can be excluded, because its strongest peak of (111) planes is missing in the experimental pattern. Another g for Si would overlap with Zr pattern.

6.2 Zr/Nb TEM analysis Structure

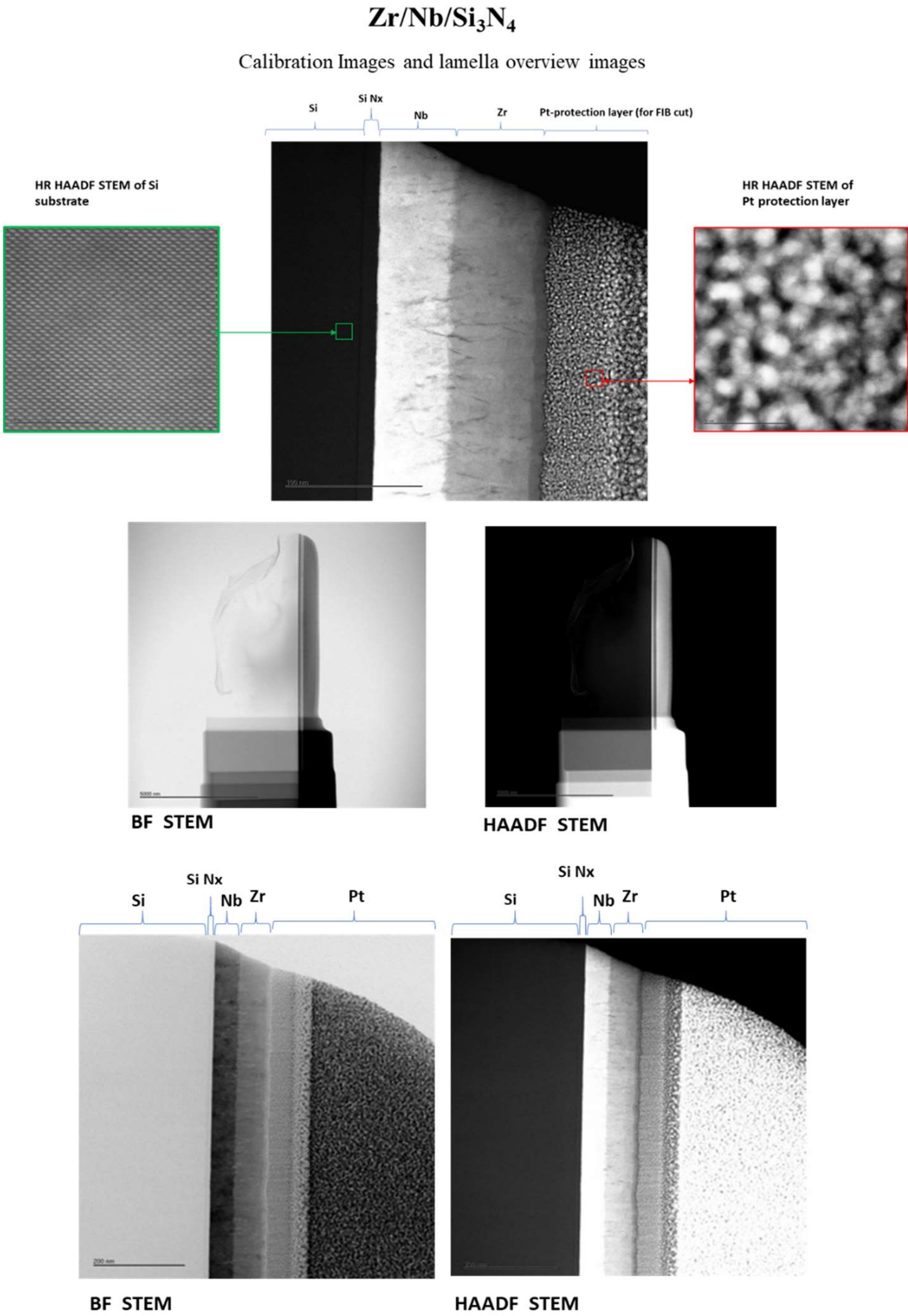

Figure 5.9. preparation of the "lamella" and calibration with SI

Zr/Nb/ Si_3N_4 EDX Analysis

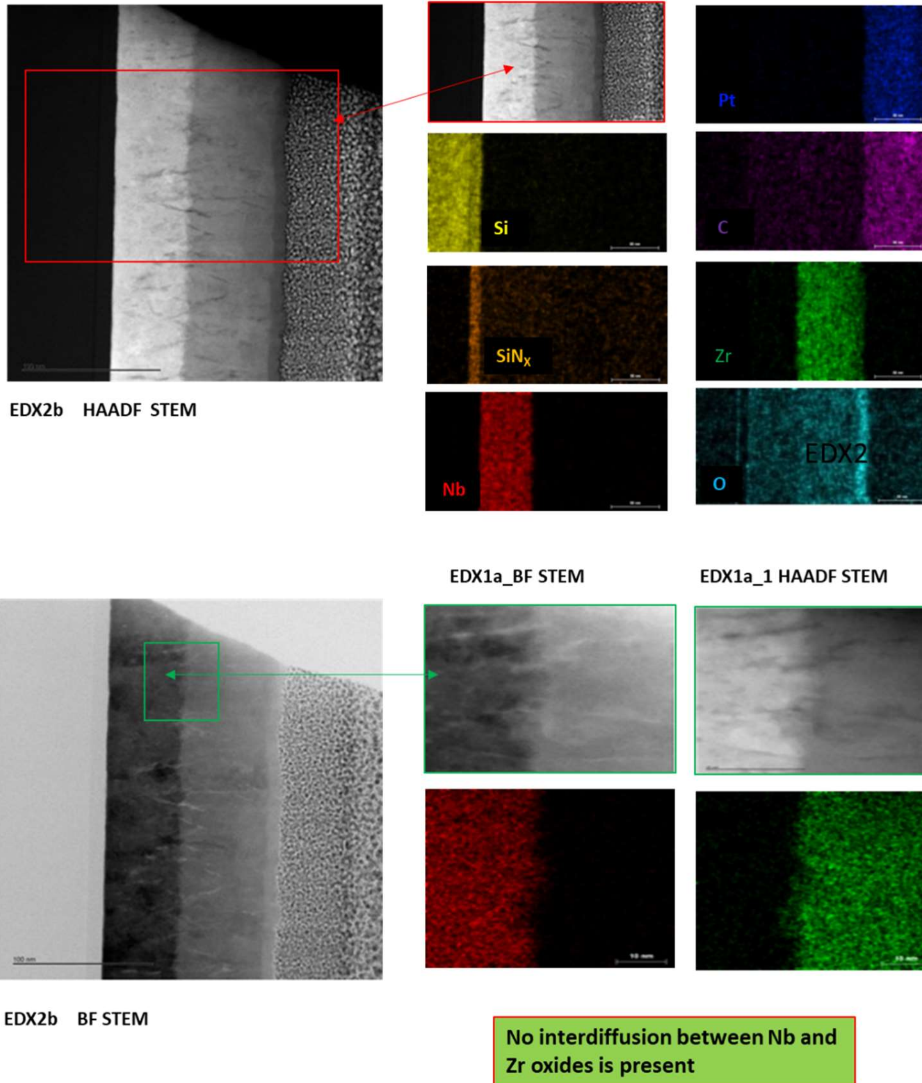

Figure 5.10. EDX analysis of the sample. It was not found interdiffusion between Nb and Zr layer.

Fourier Transform Images Analysis for Zr/Nb/Si_3N_4

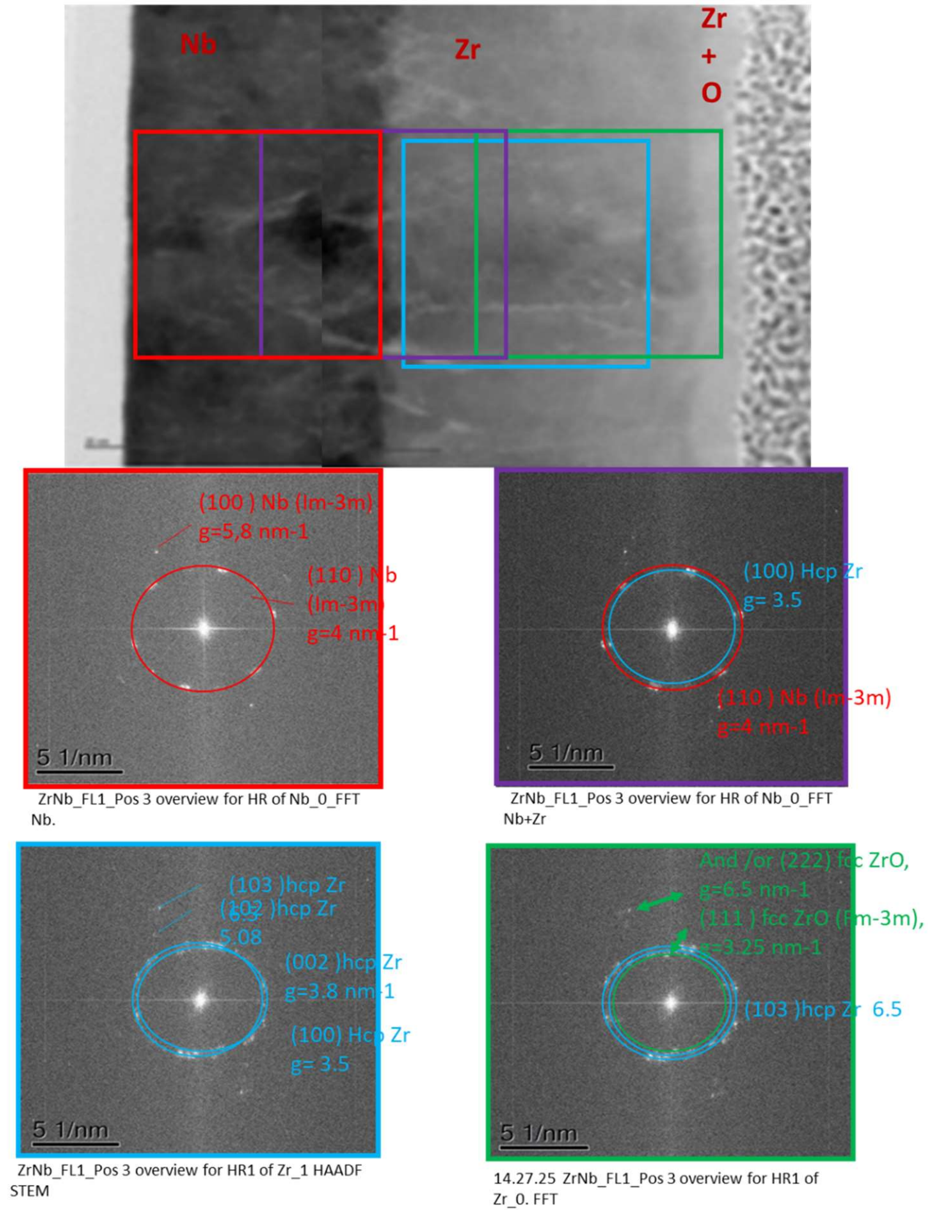

Figure 5.11 FFT diffraction pattern showing Zr and atoms of Zr oxides.

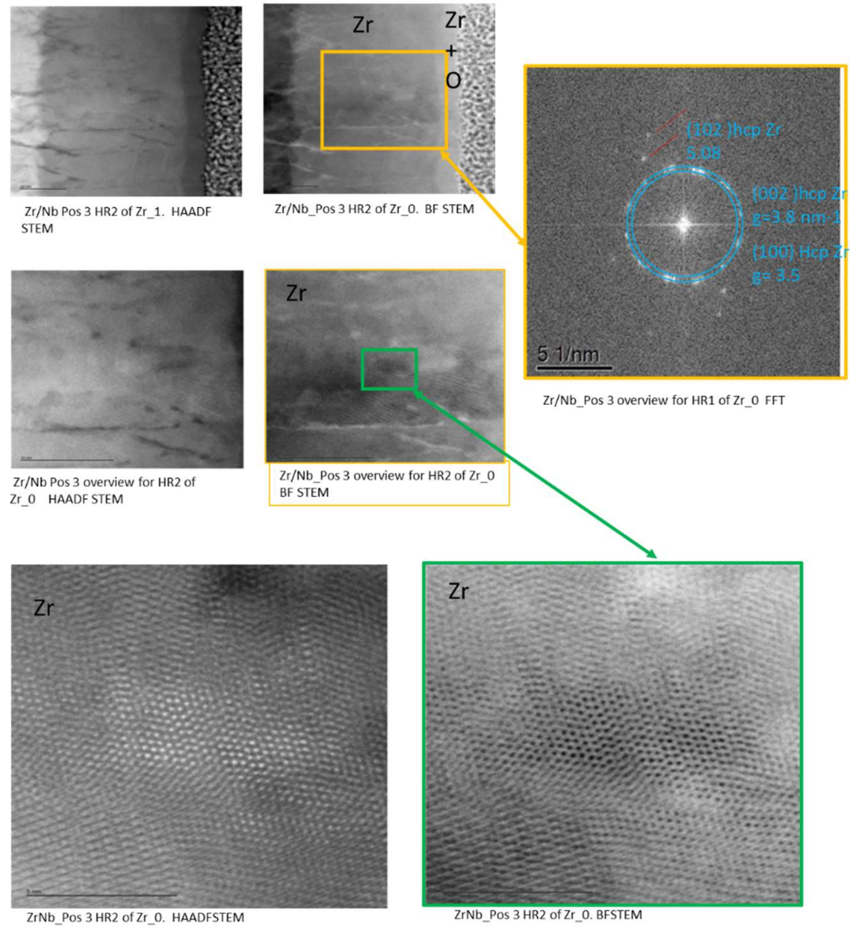

Figure 5.12. HAADFSTEM and BFSTEM images of the crystal structure of Zr.

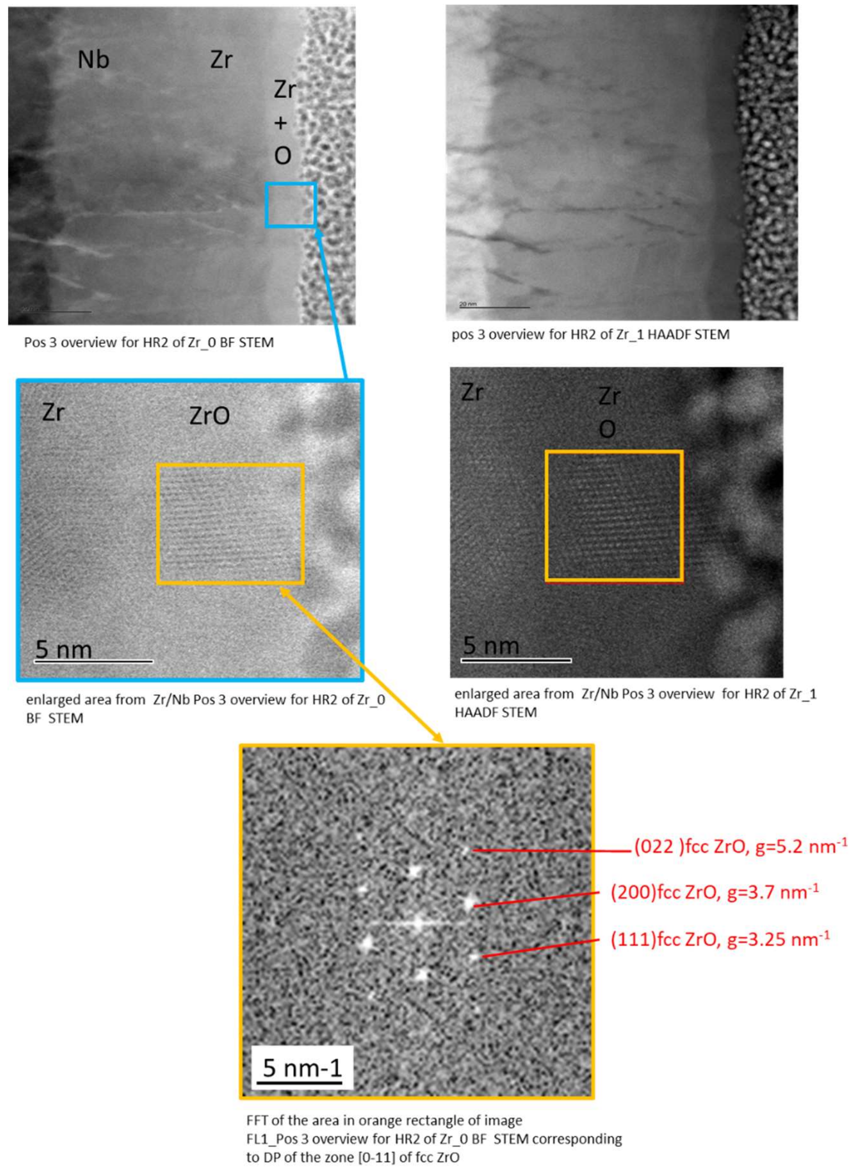

Figure 5.13. FFT image to observe the diffraction pattern and determine the crystal structure of ZrO

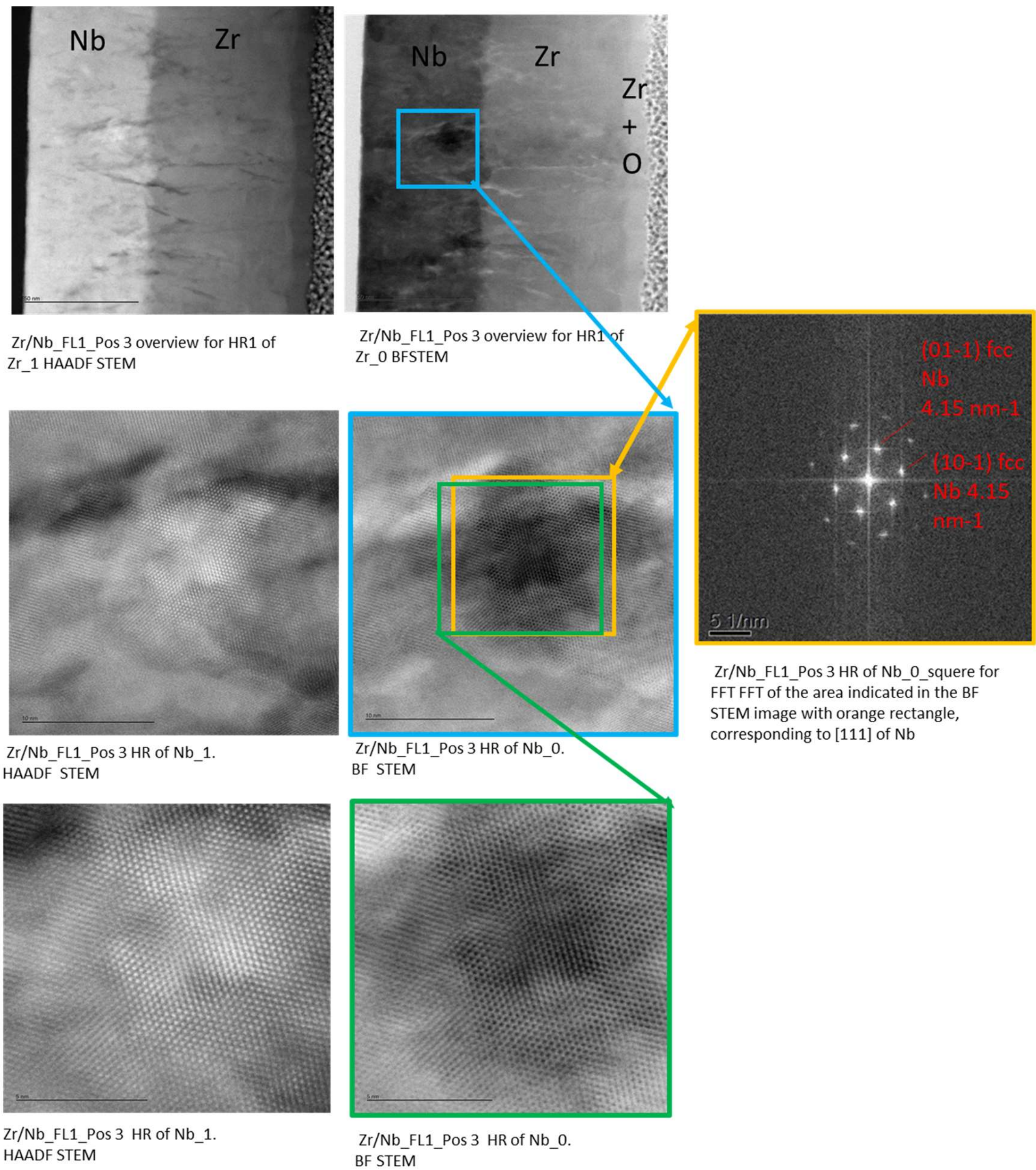

Figure 5.14 STEM images to observe crystal structure of Nb

Remarks.

- outer layer of Zr (10 nm top layer) is oxidized in Zr-Nb system, in the one with Zr layer on the top oxidation effect is not present in the systems with Nb used as a top laye. Zr layer is not oxidized there but Nb layer is – see EDX maps for 25Nb50Zr25Nb system. This may relate to your issues with failure of system you mentioned. (I do not remember in which case failure took place)!
- Fourier Transform (FT) images from the respective areas could be well indexed with the unit cells of Nb (Im-3m) and Zr hcp (i.e. high temperature hexagonal structure of Zr with space group $P6_3/mmc$) and cubic ZrO (space group Fm-3m) Unit cell one can recalculate from the values of given g. Detailed images and analysis of FT images is shown on the subsequent slides.
- Fourier Transform (FT) images in slide 5 were indexed with the unit cells of d Zr hcp (i.e. high temperature hexagonal structure of Zr with space group $P6_3/mmc$) parameters of model used are a=0,323 nm c=0,515 nm. For this model g (002) =3.88 nm-1 and g (100) =3.57 nm-1, while from experimental images we got g(002)=3.8 nm-1 and g(100)=3.5 nm-1 so the unit cell parameters will be respectively bigger than that of model.
- Fourier Transform (FT) images in slide 7 were indexed with the unit cell of cubic ZrO (space group Fm-3m) with a=0,513 nm. **For this model should be** g (200) =3.896 nm-1 and g(220)=5.51, while from **experimental image FT we got:** g(200)=3.7 nm-1 and g(220)=5.2 nm-1 so the unit cell parameter will be respectively bigger than that of model
- Fourier Transform (FT) images in slide 8 (and slide 4) were indexed with the unit cell of cubic cells of Nb (Im-3m) with a=0.33nm. **For this model** g(200) =6.06 nm-1 and g(220)=4.28 nm-1, while from **experimental image FT we got:** g(200)=5.8 nm-1 (from FT of image 14.23.25 ZrNb_FL1_Pos 3 overview for HR of Nb_0_FFTNb.tif given in slide 4) and g(220)=4.15 nm-1, (from slide 8), so the unit cell parameter will be respectively bigger than that of model.
- Each time the experimental parameters appear to be c.a. 5% bigger then these of the model. Considering the calibration overestimation of 2% evaluated for Si (for the sample 25Nb50Yr25Nb), 2-3% difference in the lattice parameter can be assumed.

6.3 Nb/Zr/Nb TEM analysis structure

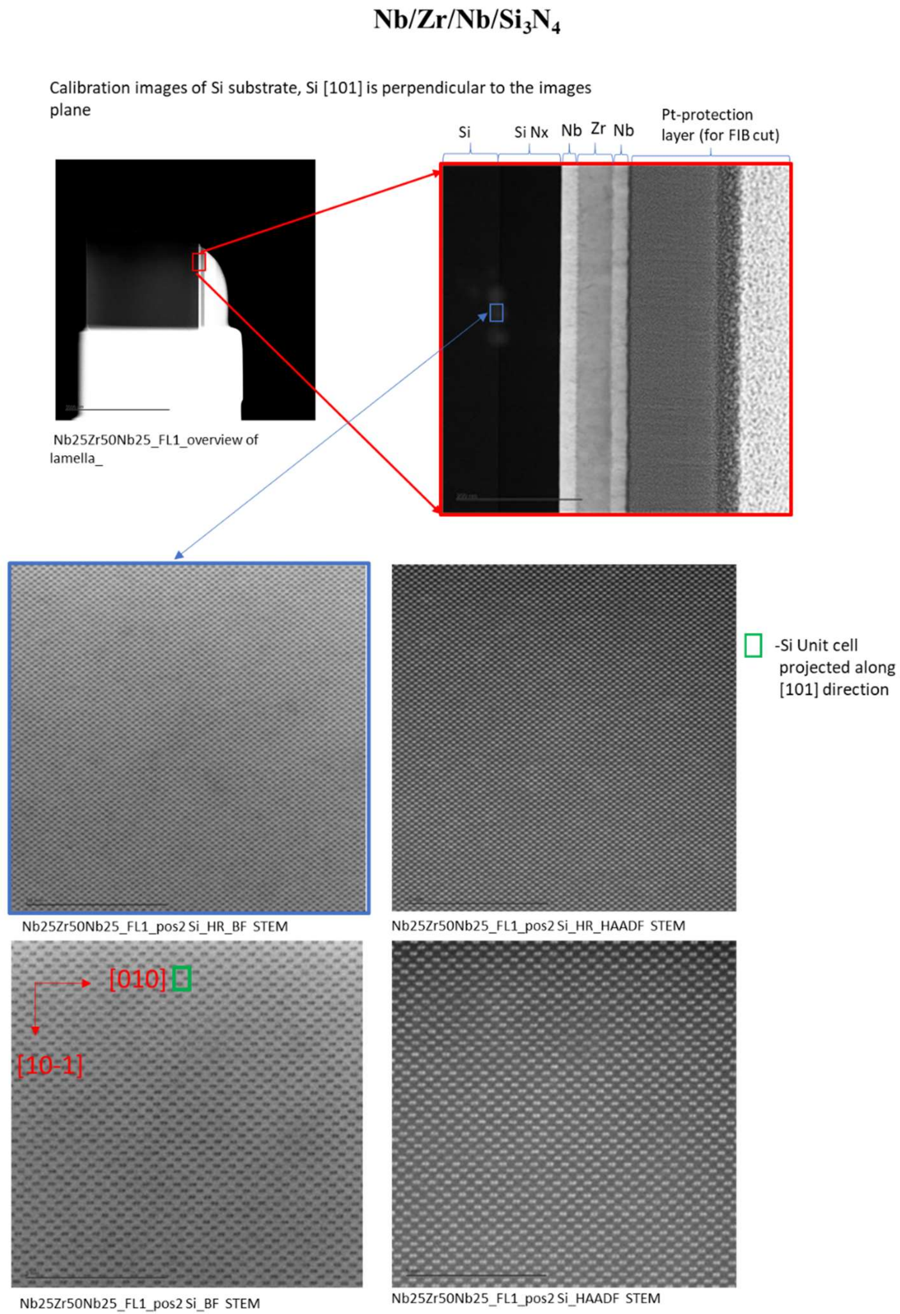

Figure 5. 15. Calibration of the images using the Si substrate. Crystal structure of Si can be appreciated.

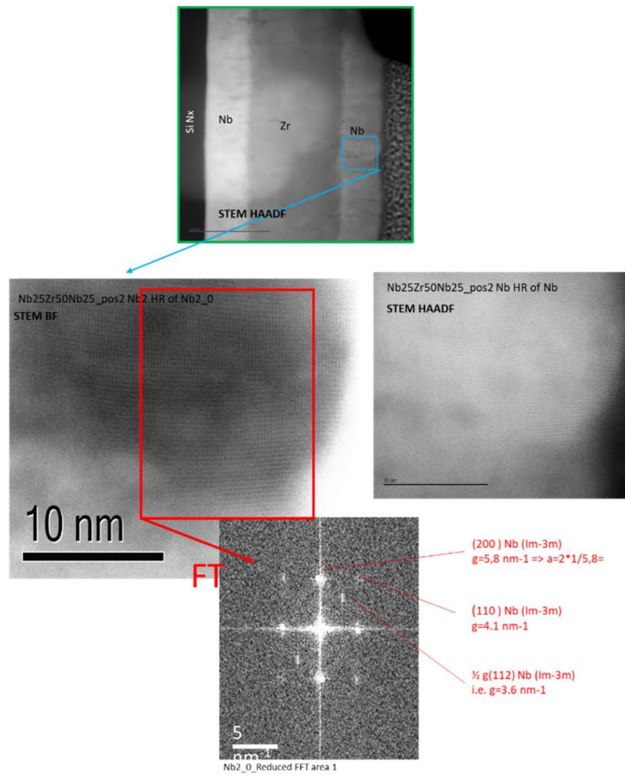

Figure 4.16. Diffraction pattern of STEM image showing Nb structure.

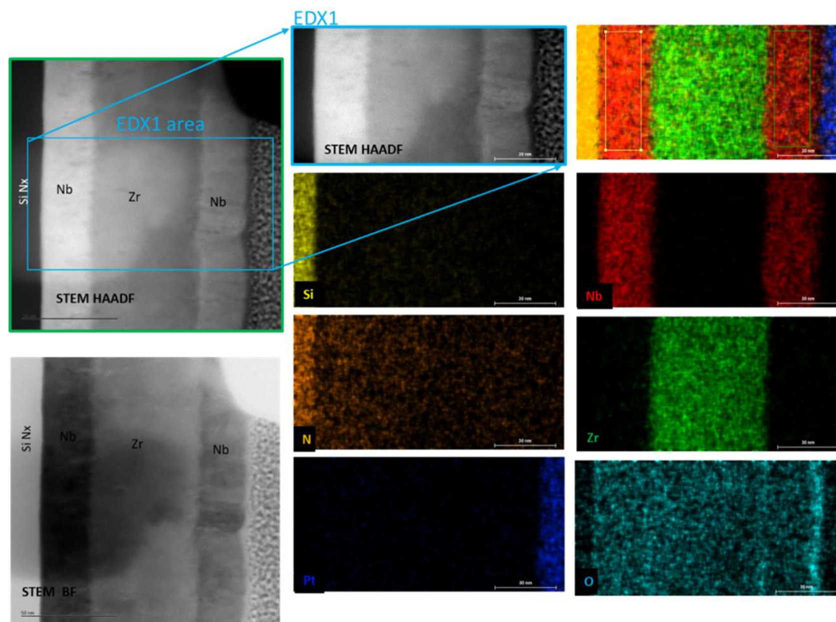

Figure 4.17. EDX analysis of the difference interface s interactions, no interdiffusion was found

Summary of conclusions:

- Si images shown in the first slide were used to check calibration of the microscope and it was found that unit cell parameters measured from HRSTEM will be overestimated for 2%
- From the HRSTEM images the unit cell of Nb in the outer layer is about 0,338 nm (after consideration of 2% overestimation calculated via calibration from HRSTEM images of Si)
- Cannot explain the origin of additional g with 3.6 nm-1 It does not fit to NbO (Pm3m), but could be some superstructure.
- No interdiffusion was observed between the layers, also at higher resolution.
- Oxidation of the most outer part (c.a. 5nm thin) of the top Nb layer can be observed (see O maps in EDX1)
- the internal boundaries between Zr and Nb layers are not perfectly flat - roughness of the interphase is in the range of 1-2 nm.

6. Study of EUV radiation damage on free self-standing Nb, Zr, Nb/Zr, and Zr/Nb thin film filters. (Ongoing)

6.1 Introduction

When optical devices such as thin film absorption filters, mirrors and others, which operates under vacuum of about 10-6 Pa or lower, in high brilliance sources, are exposed to EUV radiation in presence of residual contaminants (more often water vapor and hydrocarbons), their surfaces ae susceptible to oxidation, carbon deposition and other chemical reactions.

EUV optics are used in vacuum conditions to minimize absorption of EUV light by air. The main chamber is filled with optics, sensors, reticles, electric wiring and numerous other components [11]. All these components not only produce outgassing but also make baking of the vacuum system impossible. Which can also lead to the contamination of the filters. The residual gas mixture consists of many different components including hydrogen, oxygen, water and hydrocarbons. Moreover, the contribution of hydrocarbons produced during the exposure process itself cannot be ignored. Most filters are very susceptible a carbon contamination, reducing their transmittance performances.

The photochemistry of the relevant processes at the surface of the multilayer optics is found to be largely dependent on the type and pressure of background gas constituents and the incident flux of the EUV photons. Under illumination of EUV radiation, photoelectrons of less than 10 eV are typically created [12]. Cracking of adsorbed molecules at the optical surface by those photoelectrons or by EUV photo dissociation directly results in contamination of the surface of the optical devices with molecules and radicals [13-15].

Water and oxygen act as oxidizers, most of the materials available for filters in EUV regions oxidize easily reducing also their performances and producing rapid aging. This effect can be prevented or mitigated by using an oxidation resistant protective capping layer.

Hydrocarbons lead to carbon growth as illustrated in Fig. 4. There are three steps leading to carbon growth: adsorption, diffusion and photon or secondary electron induced dissociation [12,13]. Unfortunately, the capping layer does not prevent the build-up of carbon contamination, leaving this as the main surface

contamination process [12]. The high absorption of EUV radiation by carbon makes the contamination layer a critical issue.

Thin film filters for extreme ultraviolet are used to remove multiple- order radiation but they are also used as gas barriers that allow introduction of contaminant gas that could damage them and of course one cause of contamination [1, 3 proposal]; this contamination reduce the performance of the multilayer filters, so proper study of the contamination due to environment and radiation exposure is necessary to determine a proper protective coating solutions for these transmittance filters.

6.2 Description of the experiment.

A set of samples were fabricated using e-beam deposition technique, samples were etched following the fabrication procedure describer in chapter 1. All samples are free standing filters Figure 6.1.

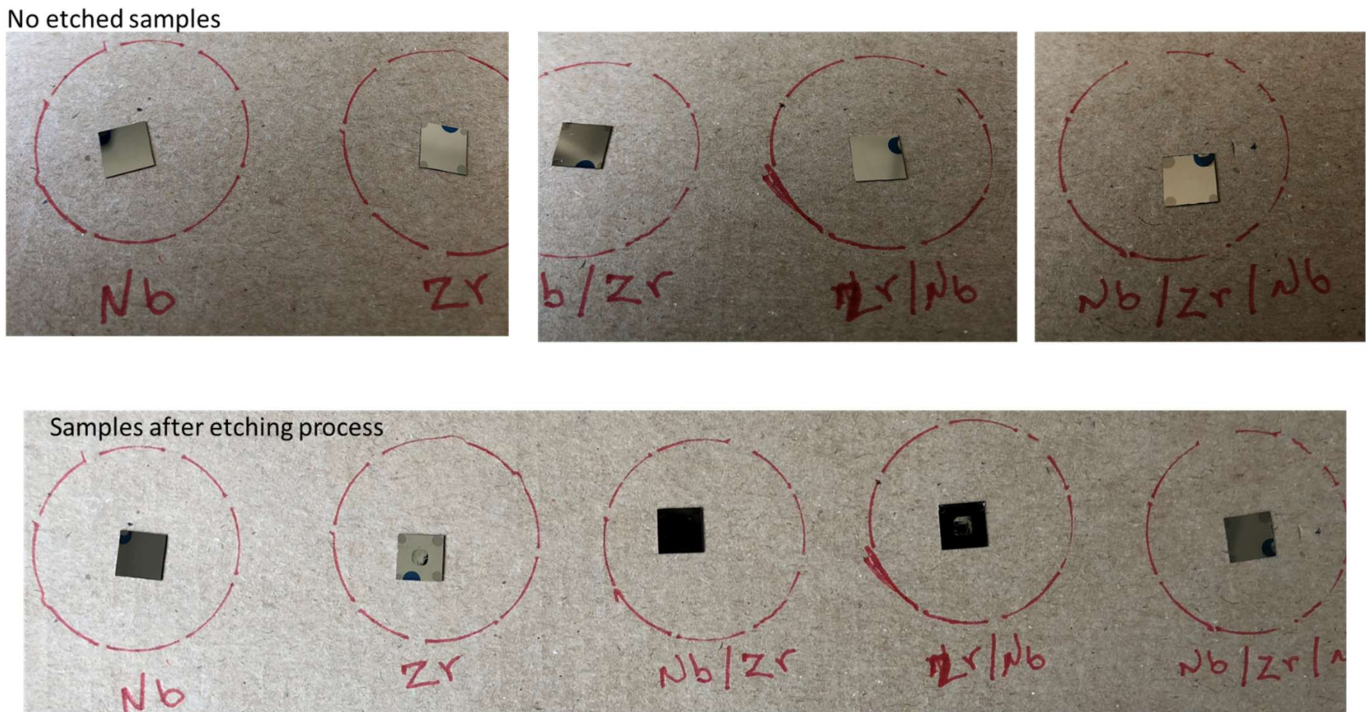

Figure 6.1. Samples before etching and after etching can be appreciate.

Samples are described in table 6.1

Sample	Thickness (nm) +/- 5nm error each layer	Objective
Nb	100	To be exposed
Zr	100	To be exposed
Zr/Nb	50/50	To be exposed
Nb/Zr	50/50	To be exposed
Nb/Zr/Nb	25/50/50	To be exposed
Nb	100 nm	Sample control
Zr	100 nm	Sample control

Samples will be characterized before and after exposure to high density radiation with the following methods of characterization.

- XPS analysis of the surface of the sample. To determine changes due to the exposure. Two samples will remain as control samples. So, the difference between contamination due to a high energy radiation exposure and the environmental contamination can be determined.
- Transmittance performance of the samples in EUV range between 5-20 nm.

6.3. High density radiation set up

As a light source, a pulsed xenon plasma discharge source is used. These sources produce a plasma pinch with sub-millimeter diameter and strong emission lines in the XUV. A collector focus a high-density energy at the focal point. The Set up is well explained at the Master Thesis of Oskar Hoffman [ref]

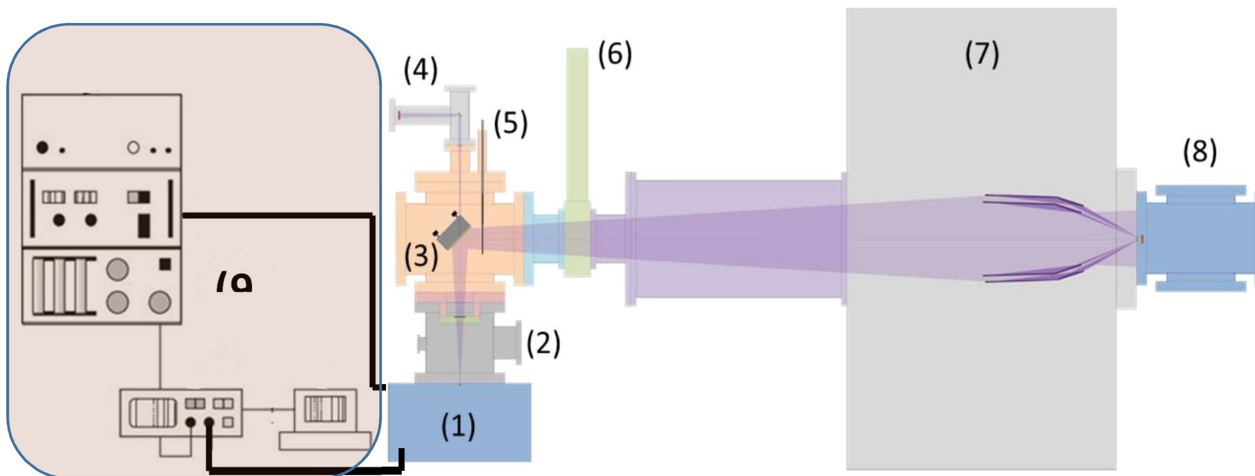

Figure 6.2 Scheme of the experimental setup with source (1), 6-way-cross connector (2), multilayer mirror (3), reference diode (4), removable collector blocker (5) (not visible in the photograph), gate valve (6), collector chamber (7) and sample chamber (8). controllers for the source and motion motors, power supply, oscilloscope and computer (9).

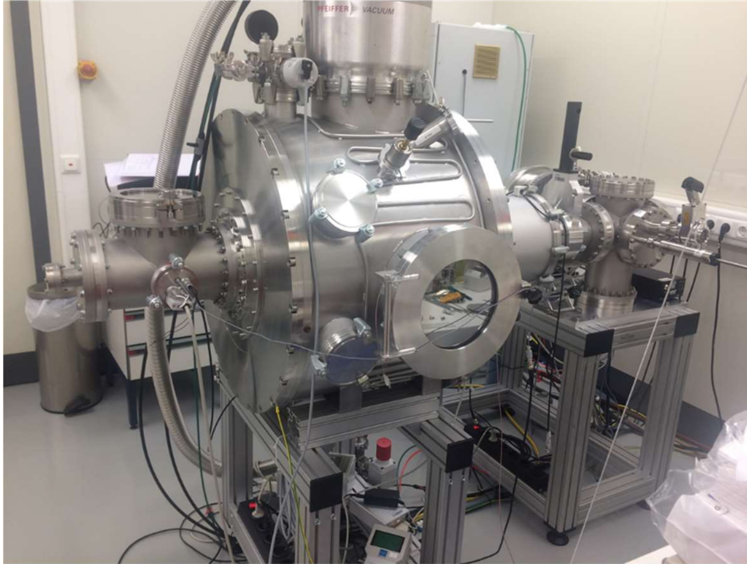

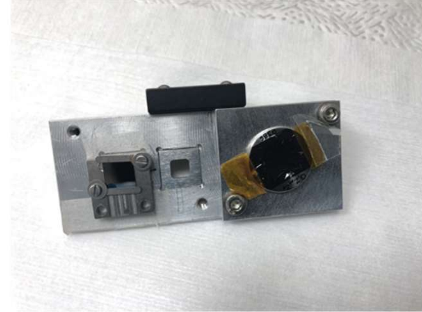

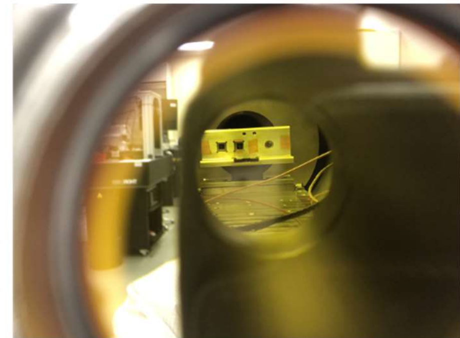

Figure 6.3 Picture of the actual set- up located in ILT institute of Aachen University.

7 Conclusion and recommendation.

- Nb and Zr have good transmittance performance between 5-20 nm and since they stay practically opaque all the way till the far infrared region, they are good candidates for EUV filters.

- Using Magnetron Sputtering as a deposition technique we achieved to etch Nb and Nb/Zr filter. Our Nb/Zr free standing filter presents a high peak transmittance value of almost 60 %.

- Using e-beam deposition technique, samples were mechanically stable and etching procedure was possible in all the samples. So, Zr, Nb, Zr/Nb, Nb/Zr and Nb/Zr/Nb free standing filters were achieved with a total nominal thickness of 100 nm.

- EDX analysis of the samples showed that there is not interdiffusion between Zr and Nb interfaces.

- Besides the presence of a residual thin layer of Si_3N_4 on the bottom of the sample, the XPS analysis of the Nb/Zr free standing filter indicated that the reduction of the expected values on transmittance could be due to the surface contamination and some level of oxidation of the metal layers. Also XPS of all samples showed some level of oxidation in the samples.

- It is recommended to grow an oxidation protection layer in situ with the metal material to avoid progressive oxidation of the filters.

Bibliography.

[1] Masatoshi Hatayama et al. High-Transmittance Free-Standing Aluminum Extreme Ultraviolet Filter 2009 *Jpn. J. Appl. Phys.* **48** 122202.

[2] Gann E, Young AT, Collins BA, Yan H, Nasiatka J, Padmore HA, Ade H, Hexemer A, Wang C. “Soft x-ray scattering facility at the Advanced Light Source with real-time data processing and analysis”. Review of Scientific Instruments 83, 045110 (2012).

[3] Y. Saitoh, H. Kimura, Y. Suzuki, T. Nakatani, T. Matsushita, T. Muro, T. Miyahara, M. Fujisawa, K. Soda, S. Ueda, H. Harada, M. Kotsugi, A. Sekiyama, and S. Suga. “Performance of a very high-resolution soft x-ray beamline BL25SU with a twin-helical undulator at SPring-8”. Review of Scientific Instruments 71, 3254 (2000).

[4] Wayne R. McKinney and Dmitri Mossessian. “Efficiency and stray light measurements and calculations of diffraction gratings for the Advanced Light Source”. Review of Scientific Instruments 66, 2160 (1995).

[5] J.H Underwood, E.M Gullikson, “High-resolution, highflux, user friendly VLS beamline at the ALS for the 50– 1300 eV energy region”, Journal of Electron Spectroscopy and Related Phenomena 92 (1998) 265–272.

[6] F Bencivenga, S Baroni, C Carbone, M Chergui, M B Danailov, G De Ninno, M Kiskinova, L Raimondi, C Svetina and C Masciovecchio. “Nanoscale dynamics by short-wavelength four wave mixing experiments”. New Journal of Physics 15 (2013).

[7] O'shea, P.G., Freud, H.P. Free-electron lasers: status and applications. (2001). Science 292, 1853.

[8] C.J. Bocchetta et al. FERMI@Elettra Conceptual Design Report, 2007. Technical Report ST/F-TN-07/12, Sincrotrone Trieste.

[9] M. Zangrando, D. Cocco, C. Fava, S. Gerusina, R. Gobessi, N. Mahne, E. Mazzucco, L. Raimondi, L. Rumiz and C. Svetina. “Recent results of PADReS, the Photon Analysis Delivery and Reduction System, from the FERMI FEL commissioning and user operations”. J. Synchrotron Rad. (2015). 22, 565-570.

[10] Tarrio, C., Berg, R. F., Lucatorto, T. B., Lairson, B., Lopez, H. & Ayers, T. “Thermally stable thin-film filters for high-power extreme-ultraviolet applications”, (2015). The Review of Scientific Instruments, 86(11), 116103.

[11] Powell, F. R. 'Care and Feeding of Soft X-Ray and Extreme Ultraviolet Filters', Laser-Induced Damage in Optical Materials, 1992: SPIE Proc. 1848, 503.

[12] S. B. Hill, N. S. Faradzhev, L. J. Richter, S. Grantham, C. Tarrio, T. B. Lucatorto, S. Yulin, M. Schürmann, V. Nesterenko, T. Feigl, "Optics contamination studies in support of high-throughput EUV lithography tools, (25 March 2011), " Proc. SPIE 7969, Extreme Ultraviolet (EUV) Lithography II, 79690M.

[13] H.A. Macleod: Thin-film Optical Filters, Institute of Physics Publishing, Bristol and Philadelphia, 2001.

[14] Forbes R. Powell, Terry A. Johnson, "Filter windows for EUV lithography", (20 August 2001). Proc. SPIE 4343, Emerging Lithographic Technologies V.

[15] Brose S., Danylyuk S., Juschkin L., Dittberner C., Bergmann K., Moers J., Panaitov G., (...), Grutzmacher D. Broadband transmission masks, gratings and filters for extreme ultraviolet and soft X-ray lithography. (2012) Thin Solid Films, 520 (15), pp. 5080-5085.

[16] Slemzin, V.A., Goryaev, F.F. & Kuzin, S.V. Spectroscopic diagnostics of the solar coronal plasma. Plasma Phys. Rep. (2014) 40: 855.

[17] N. I. Chkhalo, M. N. Drozdov, E. B. Kluenkov, S. V. Kuzin, A. Ya. Lopatin, V. I. Luchin, N. N. Salashchenko, N. N. Tsybin, and S. Yu. Zuev, "Thin film multilayer filters for solar EUV telescopes," Appl. Opt. 55, 4683-4690 (2016).

[18] Terry A. Johnson, Regina Soufli, Eric M. Gullikson, Miles Clift, "Zirconium and niobium transmission data at wavelengths from 11-16 nm and 200-1200 nm", Proc. SPIE 5538, Optical Constants of Materials for UV to X-Ray Wavelengths, (14 October 2004).

[19] David L. Windt, Webster C. Cash, M. Scott, P. Arendt, B. Newnam, R. F. Fisher, and A. B. Swartzlander, "Optical constants for thin films of Ti, Zr, Nb, Mo, Ru, Rh, Pd, Ag, Hf, Ta, W, Re, Ir, Os, Pt, and Au from 24 Å to 1216 Å, " (1988). Appl. Opt. 27, 246-278.

[20] Y. Wu, L. Zhang, H. Cao, X. Zheng, H. Jiao, and L. Chen, "Preparation and Characterization of Free-Standing Zr Filter for Soft X-ray Laser Application," in Optical Interference Coatings, OSA Technical Digest (CD) (Optical Society of America, 2007).

[21] N. I. Chkhalo, M. N. Drozdov, S. A. Gusev, E. B. Kluenkov, A. Ya. Lopatin, V. I. Luchin, N. N. Salashchenko, L. A. Shmaenok, N. N. Tsybin, B. A. Volodin, "Freestanding multilayer films for application as phase retarders and spectral purity filters in the soft x-ray and EUV ranges", Proc. SPIE 8076, EUV and X-Ray Optics: Synergy between Laboratory and Space II, 80760O (4 May 2011).

[22] Belik, V.P., Zadiranov, Y.M., Il'inskaya, N.D. et al. Free-standing optical filters for a nanolithography source operating in the 12–15 nm wavelength range. (2007). Tech. Phys. Lett. 33: 508.

[23] Heyun Wu, Yonggang Wu, Gang Lv, Zhenhua Wang, Leijie Ling, Zihuan Xia, Naibo Chen, "Preparation and characterization of free-standing Zr, PI and Zr/PI filter", Proc. SPIE 7995, Seventh International Conference on Thin Film Physics and Applications, 79951F (18 February 2011).

[24] E. Allaria, L. Badano, S. Bassanese, F. Capotondi, D. Castronovo, P. Cinquegrana, M.B. Danailov, G. D'Auria, A. Demidovich, R. De Monte, G. De Ninno, S. Di Mitri, B. Diviacco, W.M. Fawley, M. Ferianis, E. Ferrari, G. Gaio, D. Gauthier, L. Giannessi, F. Iazzourene, G. Kurdi, N. Mahne, I. Nikolov, F. Parmigiani, G. Penco, L. Raimondi, P. Rebernik, F. Rossi, E. Roussel, C. Scafuri, C. Serpico, P. Sigalotti, C. Spezzani, M. Svandrlik, C. Svetina, M. Trovó, M. Veronese, D. Zangrando, M. Zangrando, The FERMI free-electron lasers, J. Synchrotron Radiat. 22 (2015) 485–491. doi:10.1107/S1600577515005366.

[25] David Attwood, D. Attwood, Soft X-rays and extreme ultraviolet radiation, 1999.

[26] Free-electron lasers Peter Schmuser ¨ Institut fur Experimentalphysik, Universit ¨ at Hamburg, Germany. https://cds.cern.ch/record/941330/files/p477.pdf

[27] X-ray free-electron lasers: An introduction to the physics and main characteristics. P. Musumeci Department of Physics and Astronomy, UCLA https://www.bioxfel.org/science/resources/397/download/X-ray_FELs_lecture_Musumeci.pdf.

[28] 2.V. Bakshi. Status Report on EUV Source Development and EUV Source Applications in EUVL. IEEEXPLORE/document/5760393.

[29] [8] C.J. Bocchetta et al. FERMI@Elettra Conceptual Design Report, 2007. Technical Report ST/F-TN-07/12, SincrotroneTrieste.

[30] [9] M. Zangrando, D. Cocco, C. Fava, S. Gerusina, R. Gobessi, N. Mahne, E. Mazzucco, L. Raimondi, L. Rumiz and C. Svetina. "Recent results of PADReS, the Photon Analysis Delivery and Reduction System, from the FERMI FEL commissioning and user operations". J. Synchrotron Rad. (2015). 22, 565-570.

[31] 89. Windt, D.L.: 'IMD - Software for modeling the optical properties of multilayer films', Computers in Physics, 1998, 12, (4), pp. 360-370

[32] 110. Windt, D.L.: 'IMD, Version 5, Installation and User's Manual', in Editor (Ed.)^(Eds.): 'Book IMD, Version 5, Installation and User's Manual' (2013, edn.), pp.

[33] M.A. Monclús, M. Callisti, T. Polcar, L.W. Yang, J. Llorca, J.M. Molina- Aldareguía, Selective oxidation-induced strengthening of Zr/Nb nanoscale multilayers, (2017). Acta Materialia, 122, 1-10.

[34] http://www.samaterials.com/content/147-what-are-the-applications-of-niobium, by Stanford Advanced Materials | May 17 2017 (Nb)

[35] https://www.lenntech.com/periodic/elements/nb.htm

[36] https://www.azom.com/article.aspx?ArticleID=1190

[37] Ohring, M. 'Materials science of thin films' (Academic press, 2001. 2001)

[38] G. Binnig, C. F. Quate, and Ch. Gerber. Atomic Force Microscope. Phys. Rev. Lett., 56:930 933, Mar 1986.

[39] T. L. Alford, L. C. Feldman, and J. W. Mayer. Fundamentals of nanoscale lm analysis [E-Book], 2007.

[40] L.R. Doolittle, Nucl. Instrum. Methods B 9, 344, (1985).

[41] A. A. Sokolov, F. Eggenstein, A. Erko, R. Follath, S. Künstner, M. Mast, J. S. Schmidt, F. Senf, F. Siewert, T. Zeschke, F. Schäfers, "An XUV optics beamline at BESSY II", Proc. SPIE 9206, Advances in Metrology for X-Ray and EUV Optics V, 92060J (5 September 2014).

[42] Nannarone, S., et al., "The BEAR Beamline at Elettra," AIP Conf. Proc. 705, 450 (2004).

[43] Pasquali, L., et al., "The UHV Experimental Chamber for Optical Measurements (Reflectivity and Absorption) and Angle-Resolved Photoemission of the BEAR Beamline at ELETTRA," AIP Conf. Proc. 705, 1142 (2004).

[44] A. LYAPIN, L. P. H. JEURGENS, P. C. J. GRAAT, and E. J. MITTEMEIJER, "The Initial, Thermal Oxidation of Zirconium at Room Temperature," (2004). Journal of Applied Physics 96 (12), 7126-7135.

[45] R.J. Drese, M. Wuttig, In situ stress measurements in zirconium and zirconium oxide films prepared by direct current sputtering, J. Appl. Phys. 99 (12) (2006) 0–5.

[46] K. Sokhey, S. Rai, and G. Lodha, "Oxidation studies of niobium thin films at room temperature by X-ray reflectivity," 2010. Appl. Surf. Sci. vol. 257, no. 1, pp. 222–226.

[47] C.T. Wu, "Intrinsic Stress of Magnetron-Sputtered Niobium Films," Thin Solid Films, vol. 64, pp. 103-110, 1979.